Important Notice

THE UNIVERSITY OF CALGARY

**3-D Physical Seismic Modeling Study of a Lower
Cretaceous Channel in Southern Alberta**

by

Kelly Dale Hrabi

A THESIS

SUBMITTED TO THE FACULTY OF GRADUATE STUDIES

IN PARTIAL FULFILLMENT OF THE REQUIREMENTS FOR THE

DEGREE OF MASTER OF SCIENCE

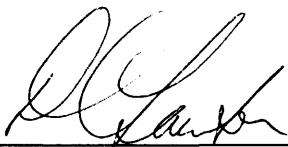DEPARTMENT OF GEOLOGY AND GEOPHYSICS

CALGARY, ALBERTA

SEPTEMBER, 1994

THE UNIVERSITY OF CALGARY
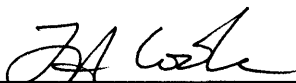
FACULTY OF GRADUATE STUDIES

The undersigned certify that they have read, and recommend to the Faculty of Graduate Studies for acceptance, a thesis entitled "3-D Physical Seismic Modeling Study of a Lower Cretaceous Channel in Southern Alberta" submitted by Kelly Dale Hrabi in partial fulfillment of the requirements for the degree of Master of Science.

Supervisor, Dr. D.C. Lawton,
Department of Geology and Geophysics

Dr. K. Duckworth,
Department of Geology and Geophysics

Dr. F. A. Cook,
Department of Geology and Geophysics

Dr. R. B. Hicks,
Department of Physics and Astronomy

1996-09-22
Date

ABSTRACT

Channel-sands of the Lower Cretaceous Glauconitic Formation in
southern Alberta are important petroleum reservoirs. They have subtle
seismic characteristics which can often be confused with shale-filled channels.
Acoustic 2-D and 3-D physical seismic modeling over a Glauconitic channel
was undertaken to gain insight into its seismic signature. Physical modeling
and 3-D survey design conclude that fold, offset and azimuth distribution are
significant for producing a high quality image of the channel structure. Three
surveys, a 2-D, zero-offset 3-D and full-offset 3-D were acquired and processed.
All three surveys produce a high quality image of the channel with the
accompanying bars and displayed the velocity pull-up anomaly on the
Mississippian event but only the full-offset 3-D survey was able to image the
velocity pull-down on the Mississippian event. From this modeling study it
was concluded that full-offset 3-D surveys are important for distinguishing a
sand-filled channel from a shale-filled channel.

TABLE OF CONTENTS

LIST OF TABLES

LIST OF FIGURES

LIST OF SYMBOLS

CMP   common mid-point

Fresnel zone   the portion of a reflector from which reflected energy can reach a detector within one-half wavelength of the first reflected energy

Horizon map   base map showing an interpreted horizon

Offset   distance between source and receiver

Residual statics   reflection statics

RMS   root mean square

Sideswipe   out-of-plane reflection

Split-spread   receiver spread with source location halfway between first and last receiver in the spread

Time slice   slice through the 3-D volume at a particular time

Velocity pick   velocity determined by semblance velocity analysis

CHAPTER 1 INTRODUCTION

1.1 General Statement

The Glauconitic Member of the Mannville Group is found at a depth of about 1000 m beneath southeastern Alberta and has been an oil play for 40 years (Hopkins et al., 1991). Oil in place in the Glauconitic Member varies from a few thousand cubic meters in single-well pools to 40 million cubic meters in the larger fields (Energy Resources Conservation Board, 1989). Most of the Glauconitic reservoirs have been found in large sand channel and present exploration is concentrating on smaller scale channel trends. These sand channels produce subtle seismic characteristics which can often be confused with a shale-filled channel and this makes delineation difficult.

The two-dimensional (2-D) common mid-point (CMP) method has been widely used to locate channel trends, but this method suffers from Fresnel zone effects, which occur when the sand is located within the Fresnel zone radius of the line. These effects produce an apparent lack of correlation between seismic amplitudes and sand thickness on 2-D seismic sections (Noah et al., 1992). The three-dimensional (3-D) method has become popular as a means to better delineate channel trends, and has the advantage of reducing the effects of Fresnel zone smearing and producing more robust correlation between sand thickness and seismic amplitude (Noah et al., 1992).

Complex seismic reflections are often associated with stratigraphic anomalies. Seismic modeling has been used to increase our understanding of complexities that occur on seismic data as well as to gain insight into the seismic signatures that specific geological sequences produce. May and Hron (1978) have shown that even for simple structures, the geometries of the reflected seismic events cannot be anticipated without the aid of modeling. In a physical

modeling experiment, the response of a known model to a well-defined seismic source is measured in the laboratory. A clear seismic representation can then be produced for a given model and this can be used to understand the more complex responses in field seismic data.

1.2 Purpose of Study

The seismic physical modeling tank at The University of Calgary was used to collect seismic data over a model of a meandering channel. This model is representative of a typical Lower Cretaceous channel system which occurs in the Little Bow area of southern Alberta (T 14, R 18-19 W4M). This area is of interest to the petroleum industry due to the discovery of oil in valley-fill channels of the Glauconitic Member of the Upper Mannville Formation (Hopkins et al., 1982). The Glauconitic valley fill channels are 2-2.5 km wide and up to 30 m thick in the Little Bow area (Wood and Hopkins, 1989). The sandstone bodies contained within the channel form elongate pods that are 3-4 km long, 300-500 m wide and up to 22 m thick.

In this study, a high resolution 2-D seismic line and 3-D zero-offset and full-offset surveys were acquired over the channel model The objectives in acquiring these data were: 1) to develop algorithms to acquire 3-D data in the physical modeling tank, 2) to test 3-D seismic processing software developed by Inverse Theory and Applications (ITA) by acquiring and processing 3-D seismic surveys from the channel model, 3) to review data acquisition parameters and acquisition geometries for 2-D and 3-D seismic surveys over this type of stratigraphic texture and 4) to determine if 3-D seismic acquisition can reduce the effect of Fresnel zone smear and thus produce a better correlation between sand thickness and event amplitude in processed seismic data.

CHAPTER 2 PHYSICAL MODELING

2.1 Introduction

Physical modeling is used to simulate real world seismic exploration in a laboratory environment (Rana and Sekharan, 1990). One advantage of physical modeling is that the geometry of the model is known while in field surveys the geometry is not well defined and therefore, the seismic response from the model can be used for testing processing software using a well defined structures. A second advantage of physical modeling is that the seismic response of the model contains multiples, mode conversions etc. which are often not included in numerical simulations. The physical modeling method has been used by many researchers to investigate acoustic propagation through a variety of earth models (McDonald et al., 1983; Zimmerman, 1991). Three-dimensional (3-D) models have been used to study geological situations where stratigraphic changes perpendicular to the seismic profile are important (Pant et al., 1988). Some early physical model experiments involved 3-D models using blocks of wax of up to several meters in dimension (O'Brien, 1955), concrete (Northwood and Anderson, 1953), plastic (Evans et al., 1953), rolled metals (Levin and Hibbard, 1955) and limestone (Howes et al., 1953). However, it is difficult to cut and pour materials into large blocks and maintain homogeneity throughout the entire volume, so this led to models being constructed using thin sheets of material which can be cut and bonded into various shapes. These type of models have several advantages over those of large blocks of single materials. The two primary advantages of using thin sheet models are that there is a wide variety of materials available in thin sheets (e.g. aluminum, steel, Plexiglas etc.) and fabrication is simple, requiring only machining, gluing, cutting or bonding to form the various shapes. It is also possible to construct thin sheet models out of

epoxy resins and RTV rubber where it is feasible to construct molds to contain the material during their hardening stage.

Later seismic modeling projects include that of Hilterman (1970), who investigated reflection and diffraction patterns associated with anticlines and fault structures and French (1974) who examined the oblique seismic reflection profiles of two-dimensional and three-dimensional models. French concluded that three-dimensional seismic migration is necessary to eliminate or reduce ambiguities caused by sideswipe. Newman (1980) investigated a buried channel model by using the Kirchhoff 3-D migration method. Hospers (1985) used a physical model to investigate sideswipe and other external reflections from salt plugs in the Norwegian Basin. Cheadle (1988) and Nazar (1990) used the physical modeling tank at the University of Calgary to study the seismic response of permafrost sediments in the Beaufort Sea and a meandering shale-filled Mannville channel from southern Alberta respectively.

2.2 Physical Modeling System

The physical modeling system at the University of Calgary is described by Cheadle et al. (1985). The physical modeling system consists of a water filled tank (4 m long by 3 m wide by 2 m high), two perpendicular motorized beams, three spherical ITC-1089C piezoelectric transducers, a digital oscilloscope, a pulse generator, a pre-amplifier and a personal computer. The transducers have a bandwidth of 100-600 kHz and the digital oscilloscope can sample down to a 50 nano-second time sample interval.

For the modeling experiment, a scaled physical model is constructed and submerged in the tank. The model is leveled and the height of the transducers above the model is set so that the multiple reflection that is produced off the surface of the water arrives at the receiver much later than any reflected energy

from the model. The model is also located away from the walls of the tank so that any reflected energy from the walls of the tank arrives at the receivers much later than the reflected energy from the model. Piezoelectric transducers operate as both the source and receivers and they travel across the model on motorized beams. The personal computer controls the location of the source and receivers on each shot and different acquisition programs can be executed by the computer (i.e. 2-D or 3-D acquisition). A source signal is obtained by summation of three square waves generated by the pulse generator, and each pulse can be individually adjusted in duration and amplitude so the summation of them produces a desired zero-phase wavelet. The signal recorded by the receivers is digitized by the oscilloscope and then stored with each seismic trace containing a maximum of 4096 samples. The physical modeling data are stored on the department SUN computing system in SEG-Y format.

2.2.1 Physical model scaling

The real world and simulated environments in the laboratory are related by the scaling of physical equations based upon the principles of physical similitude (Buckingham, 1914). McDonald et al. (1983) discusses the concepts of scaling for physical models that each dimension in the original field experiment is directly proportional to a corresponding dimension on the model. The length scale factor is related to the velocity and time scale factors by the physical law:

$$\text{distance} = \text{velocity} \times \text{time} \qquad (3.1)$$

To construct a physical model, the linear dimensions are scaled so that a large area in the field can be represented by a reasonably sized physical model. Equation (3.1) can be written as:

$$\text{distance (D)} = \text{velocity (V)} \times \text{time (T)} \qquad (3.2)$$

where D, V and T are dimensionless scaling factors.

The time scale factor is chosen such that the scaled frequency bandwidth of the piezo electric transducers is comparable to the bandwidth of seismic data. The spherical piezo electric transducers have a bandwidth of 100 - 600 kHz and a central frequency of about 250 kHz. The sampling intervals on the digital oscilloscope range from 50 to 500 ns. For a time scale factor of 5000, the scaled bandwidth of the transducers is 20 -120 Hz. For a model system sample interval of 200 ns, the full scaled sample interval is 200 ns x 5000 (1 ms). Typical time scale factors range from 5000 to 10000. The distance scale factor is chosen to be as small as possible to minimize the effects of positioning errors but not too small to make the scale model too large to construct and handle. The velocity scale factor is chosen based on the finite range of acoustic velocities of materials used for physical model construction. Typical velocity scale factors range from 1 to 3.

2.2.2 Physical modeling scaling limitations

The simulation of field data by means of physical modeling data collected in the laboratory is limited by the accuracy of the recording system in the laboratory and by the accuracy with which the physical model represents the actual earth model. The time scale factor for physical modeling is limited by the dominant frequency of the transducers. There is a limited range in the acoustic velocities for the modeling materials and the velocity of acoustic waves in water also limits the velocity scaling factor. The distance scaling controls the spatial size of the model so the scale factor is chosen such that a reasonable size physical model can represent the earth model. In the laboratory acquisition of the data, the distance scaling factor affects the positional accuracy of the source and receivers due to the finite step size of the stepping motors. For a 1:5000 distance scale factor the stepping motors have a positional accuracy of ± 0.5 mm which represents a full scale positional error of ± 2.5 m.

The data acquisition is also restricted by the number of data samples which can be stored on the controlling computers disk drives.

CHAPTER 3   STUDY AREA GEOLOGY AND DESCRIPTION OF MODEL

3.1 Regional Stratigraphy

The Mannville Group in southern Alberta is a part of the Lower Cretaceous wedge of clastic sediment which was deposited in the foreland basin adjacent to the advancing Cordillera. An informal stratigraphic column of the Lower Cretaceous group in the study area is shown in Figure 3.1.

MESOZOIC	MANNVILLE GROUP	UPPER MANNVILLE	UPPER BLAIRMORE MEMBER	
			GLAUCONITIC SANDSTONE MEMBER	
		LOWER MANNVILLE	CALCAREOUS MEMBER (OSTRACOD ZONE)	OSTRACOD LIMESTONE
				BANTRY SHALE
			SUNBURST SANDSTONE MEMBER	
			CUTBANK MEMBER	
PALEOZOIC	RUNDLE GP		LIVINGSTONE MEMBER	
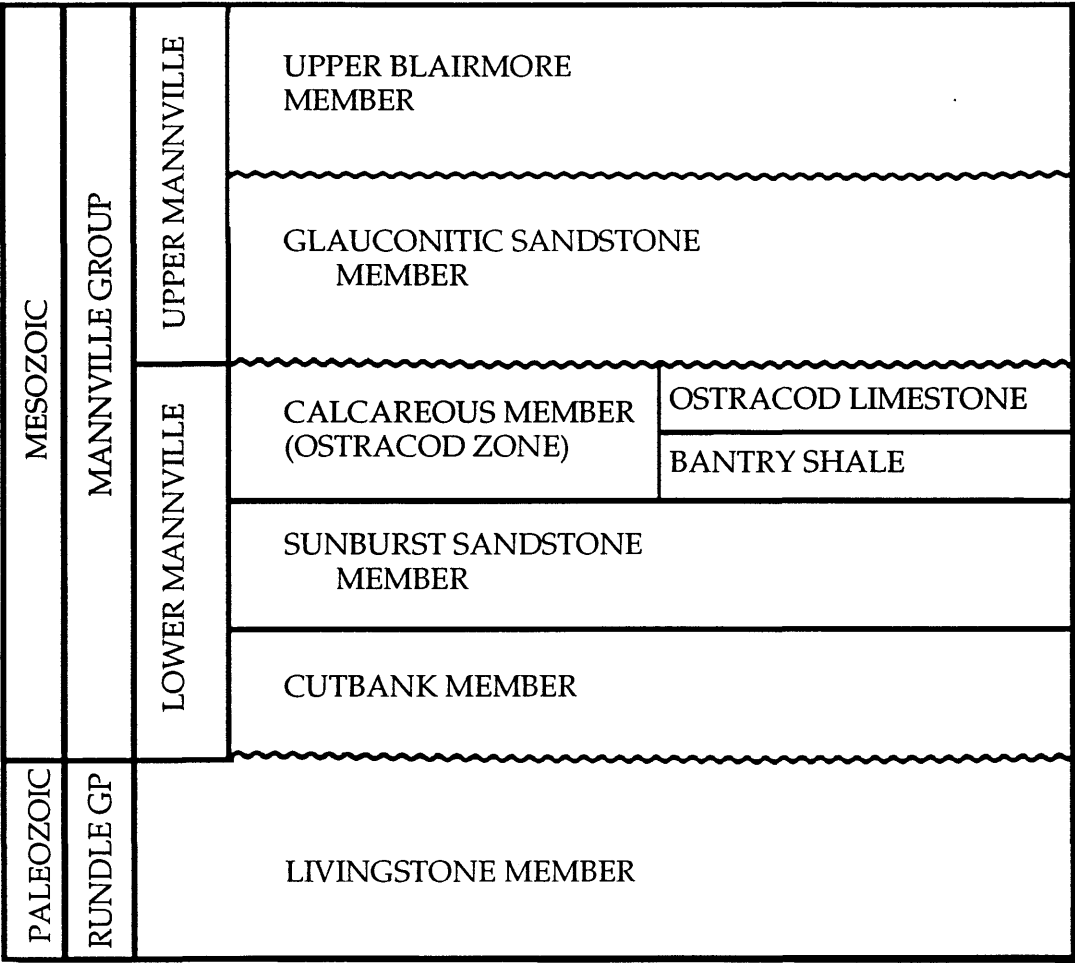
FIG 3.1 Stratigraphic column for the Mannville and upper Rundle group in the study area based on information presented by Wood (1990). The corrugated lines represent unconformity surfaces.

Glaister (1959) divided the Mannville Group into a lower and upper unit and placed the boundary between them at the top limestone bearing Calcareous Member (Figure 3.1). Farshori (1983) redefined the Calcareous Member, renamed it Ostracod beds and subdivided it into the A and B units which became known as the Bantry Shale and Ostracod Limestone respectively. The Bantry Shale and Ostracod Limestone form stratigraphic markers over a wide area of southern Alberta and northern Montana (Glaister, 1959) and these two marker beds can be correlated on logs throughout southern Alberta. In the Little Bow area the Bantry Shale and Ostracod Limestone can be recognized regionally except where they have been incised and replaced by valley fill at the base of the Glauconitic Member (Wood and Hopkins, 1989).

Several transgressive-regressive cycles were included in the Mannville Group as the Boreal Sea advanced and retreated into the foreland basin in response to sea level changes (Farshori and Hopkins, 1989). One of these cycles represents the Glauconitic Member (VanWagoner et al., 1987) which lies unconformably above the Ostracod beds (Farshori, 1983; Wood and Hopkins, 1989). The Glauconitic Member is an unconformity-bounded sequence which was named in this manner due to the presence of glauconite in marine sandstones in central Alberta (Glaister, 1959).

The Ostracod beds were deposited when the Boreal Sea had transgressed to a southerly position. The paleotopography of the Sub-Mannville unconformity was almost completely buried (Jackson, 1984).

3.1.1 Geological setting of the study area

The geology of the area in and around the Little Bow area of southern Alberta (T 13-14 R 18-19 W4) has been extensively studied by Hopkins et al., (1982) and Wood and Hopkins (1989). This area is of interest to the petroleum

industry due to the discovery of oil in valley fill channels of the Glauconitic Member of the Upper Mannville Formation (Hopkins et al., 1982). The Glauconite valley fill channels are 2-2.5 km wide and up to 30 m thick in the study area (Wood and Hopkins, 1989). They cut down through the Calcareous Member to the top of the Sunburst Member. The sandstone bodies contained within the channel are 3-4 km long, 300-500 m wide and up to 22 m thick, forming elongate pods (Wood and Hopkins, 1989).

3.2 Physical Model

3.2.1 Field parameters

To construct a physical model of the Lower Mannville sequence, sonic log information was obtained for the different members of the Mannville Group. The top of the model represents the Upper Blairmore Member and the base of the model represents the Mississippian (Livingstone Member). Most of the model detail represents the channel and the surrounding members. The sonic velocities, density and thicknesses of the different members in the Mannville Group were determined from the examination of about a dozen well logs (sonic and density) from the study area. The correlation of the different members of the Mannville Group was based on the work of Wood (1990) in the study area.

A map showing wells in the study area is presented in Figure 3.2. Three wells that represent an off-channel regional well (2-12), a shale-filled channel well (10-24) and a sand-filled channel well (6-1) are shown in cross-section in Figure 3.3. These were examined in detail to determine the P-wave sonic velocities, densities and thicknesses of the different members of the Lower Mannville sequence. In well (2-12) the Glauconitic sandstone Member is approximately 16 m thick and the sonic velocity of the good porosity sand is 3226

WELL LEGEND

✳ = Gas well

✧ = Dry hole

● = Oil well
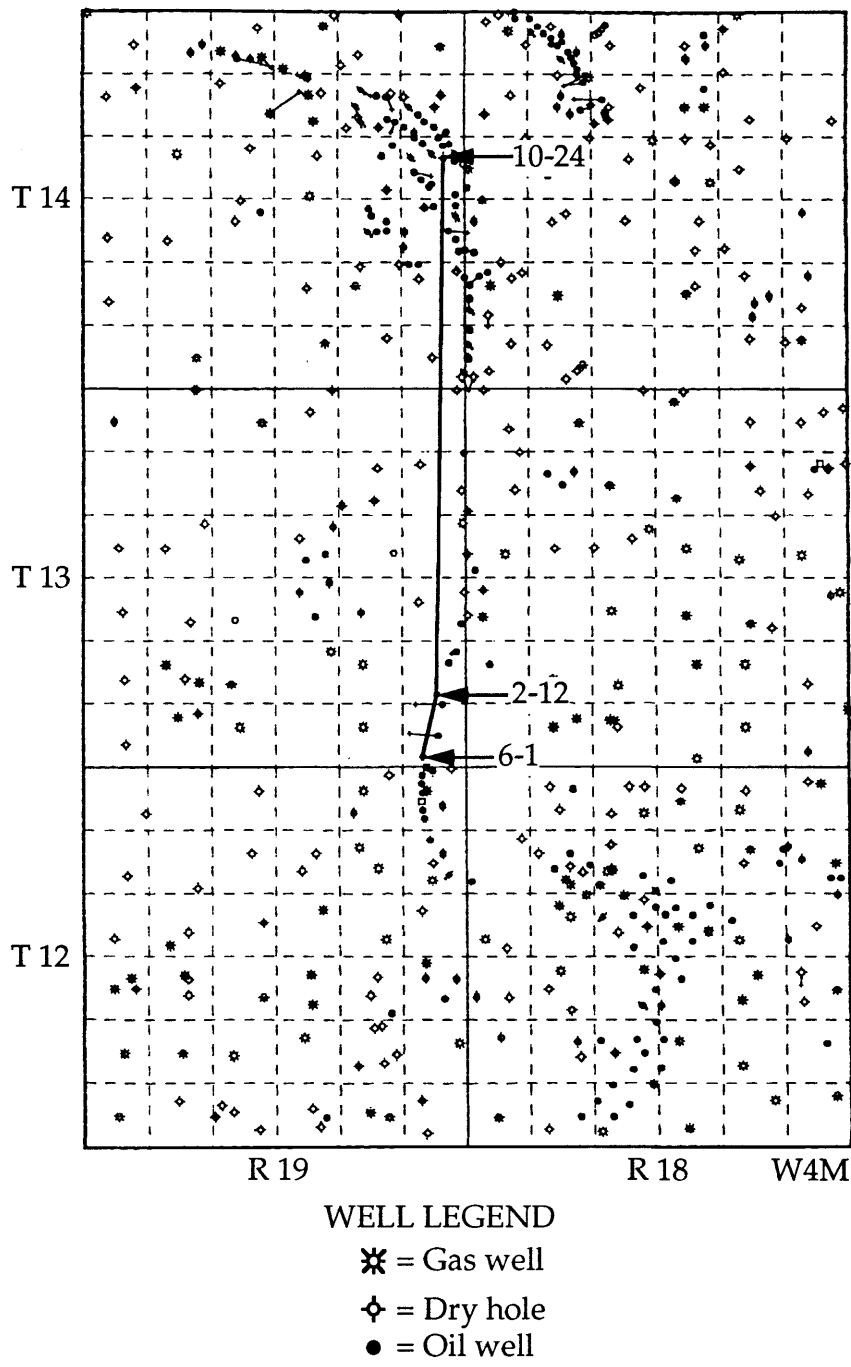
FIG. 3.2 A map of the study area. The black line indicates location of cross section shown in Figure 3.3.
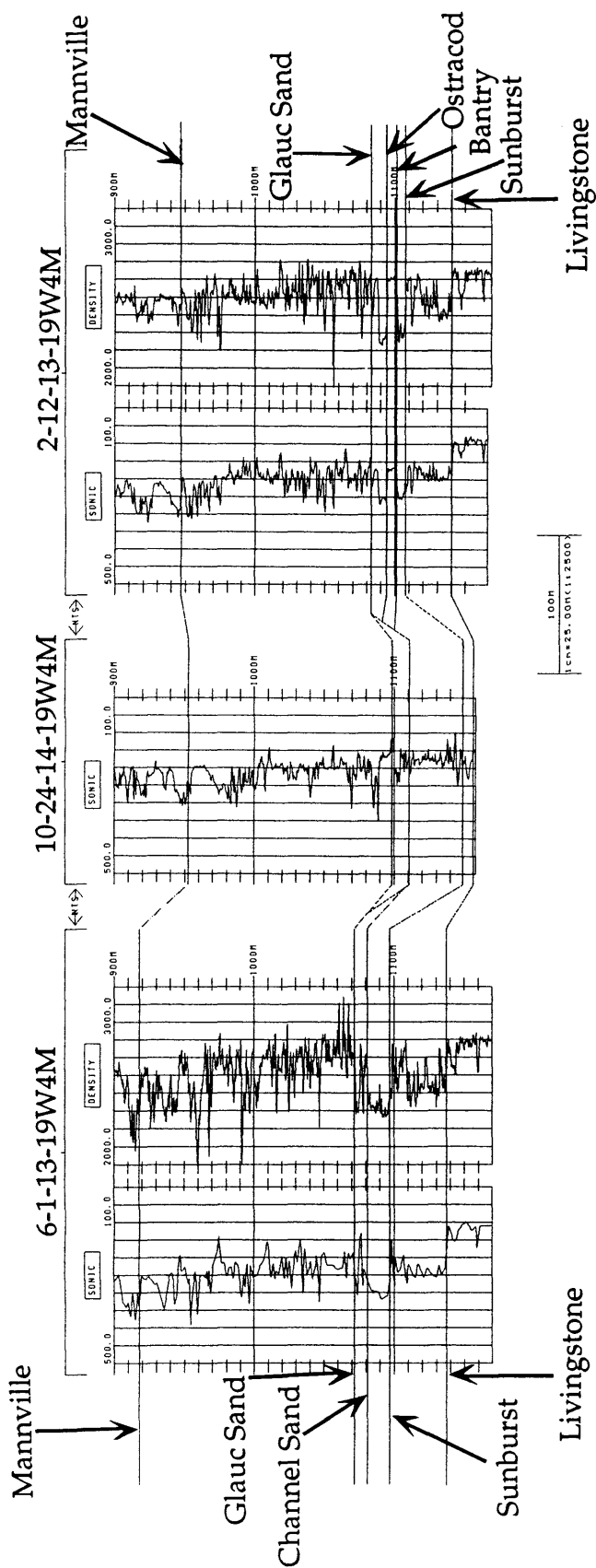
FIG. 3.3 Cross section of sonic and density logs indicating a Glauconitic sand channel, a shale-filled channel and a regional well.

m/s and its density is 2270 kg/m^3. The Ostracod Member is 6 m thick and its sonic velocity and density respectively are 4166 m/s and 2600 kg/m ^{3}. Underlying the Ostracod Member is the Bantry Shale Member which is 7 m thick and which has sonic velocity of 3390 m/s and density of 2300 kg/m^3. This sonic velocity is very high for a typical Bantry Shale as the average value in the study area is approximately 2750 m/s. Below the Bantry Shale Member is the Sunburst Member which is 33 m thick and its velocity and density are 3850 m/s and 2450 kg/m^3 respectively. The Livingstone Member lies below the Sunburst Member and it has a velocity of 5555 m/s and a density of 2600-2650 kg/m^3.

The 10-24 well intersected a channel totally filled with shale (37 m thick) with a sonic velocity and density of 4166 m/s and 2600 kg/m^3 respectively. The 6-1 well intersected 17 m of channel-fill sandstone. Its sonic velocity and density, respectively, are 2941 m/s and 2325 kg/m^3. Table 3.1 provides a summary of the average P-wave velocities and range of thicknesses for the formations of interest from the various wells examined in the study area. These velocities and thicknesses were calculated from the sonic logs of the various wells in the study area. The P-wave velocities range from 2900 m/s for the channel sand to 5400 m/s for the carbonates of the Livingstone Formation. Thicknesses vary from 2.5 m for Bantry/Ostracod members to 37 m for the Sunburst Member. It is interesting to note that, in this area, the channel shale has a velocity which is approximately 1.5 times greater than that of the channel sand.

3.2.2 Physical Model Construction

Metal, plexiglass, epoxy resins, plaster of Paris and various plastics were used as model building materials to simulate the acoustic responses of layers in the earth. It was found that the acoustic properties of epoxy resins and Plaster of

Paris could be varied by adding different proportions of glass beads of various sizes.

TABLE 3.1 MODEL PARAMETERS USED FOR THE PHYSICAL MODEL

FIELD			MODEL		
FORMATION	AVERAGE P-WAVE VELOCITY (m/s)	THICK-NESS (m)	MATERIAL	SCALED VELOCITY (m/s)	SCALED THICK-NESS (m)
MANNVILLE	3500-3600	-	PLEXIGLAS	3850	178
GLAUCONITIC	3370	4-16	TRABOND	3600	10.78
CHANNEL FILL SAND	2900	30	PLASTER OF PARIS	3045	30
CHANNEL FILL SHALE	4166	30	POLYESTER RESIN & 0.1 MM GLASS BEADS	4070	30
OSTRACOD	4719	2.5-4	TRABOND & 0.66 MM GLASS BEADS	4595	4.62
BANTRY	2748	2.5-7	LEXAN	3016	5.53
SUNBURST	3846	18-37	PLEXIGLAS	3850	88
MISSISSIP-PIAN	5400	-	ALUMINUM	8904	44.45

A physical model was constructed of a meandering channel system with a 630 m wide channel and a 320 m wide point bar (Figure 3.4). The model was 1 m x 1 m in size and was constructed using a 1:7000 distance scale factor. This value was chosen as it produces a reasonably sized channel at the model scale for a world scale 630 m wide channel. A cross-section view through the center of the model is shown in Figure 3.5.

To construct the physical model, a moldable and porous material had to be found for the channel point and lateral bars so it could simulate the channel sand bodies. Plaster of Paris was chosen for the point bar because it could be shaped both wet and dry and it has a high porosity. A time scale factor of 1:5000 had to be chosen because of the sampling interval used for the study; therefore the velocity scale factor was fixed at 1:1.4 The 2175 m/s of the Plaster of Paris scales to approximately to 2900 m/s using this factor. It was decided to include the Cutbank Member with the Sunburst Member in the physical model construction because their velocities are very similar.

A physical model was constructed which modeled the Lower Mannville sequence. The base of the model was made of 0.635 cm thick aluminum plate to simulate the Livingstone Formation. Aluminum was used because a rigid base was required to prevent flexure of the model. However, its scaled velocity of 8905 m/s was greater than the Livingstone Member scaled velocity of 5400 m/s. A sheet of 1.25 cm plexiglass which simulated the Sunburst Member was bonded to the Aluminum using a acrylic glue. When the channel incised through the Lower Mannville sequence it usually cut down part way through the Sunburst Member, as shown in Figure 3.5, so the Sunburst Member forms the base of the channel. This feature was built into the physical model by cutting the channel down into the plexiglass sheet. Overlying the Sunburst Member was the Bantry
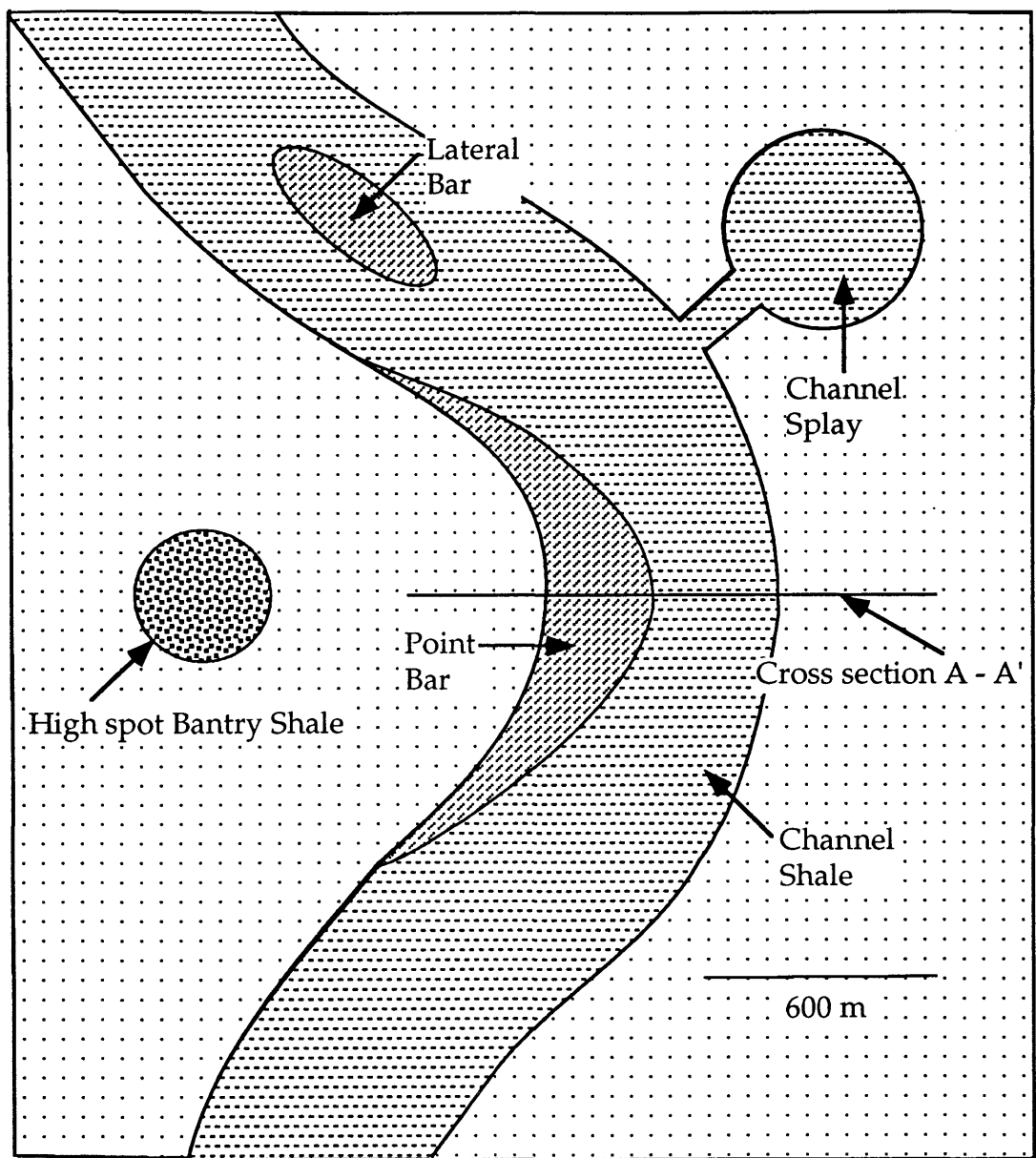
FIG. 3.4 A schematic diagram of the physical model with the top layer removed (Upper Blairmore Member) showing the location of cross section A - A'. The horizontal dashes are the channel shale, angled dashes are the point and lateral bars, dots are the Glauconitic Member and speckled circle is the unintended high spot in the Bantry shale.
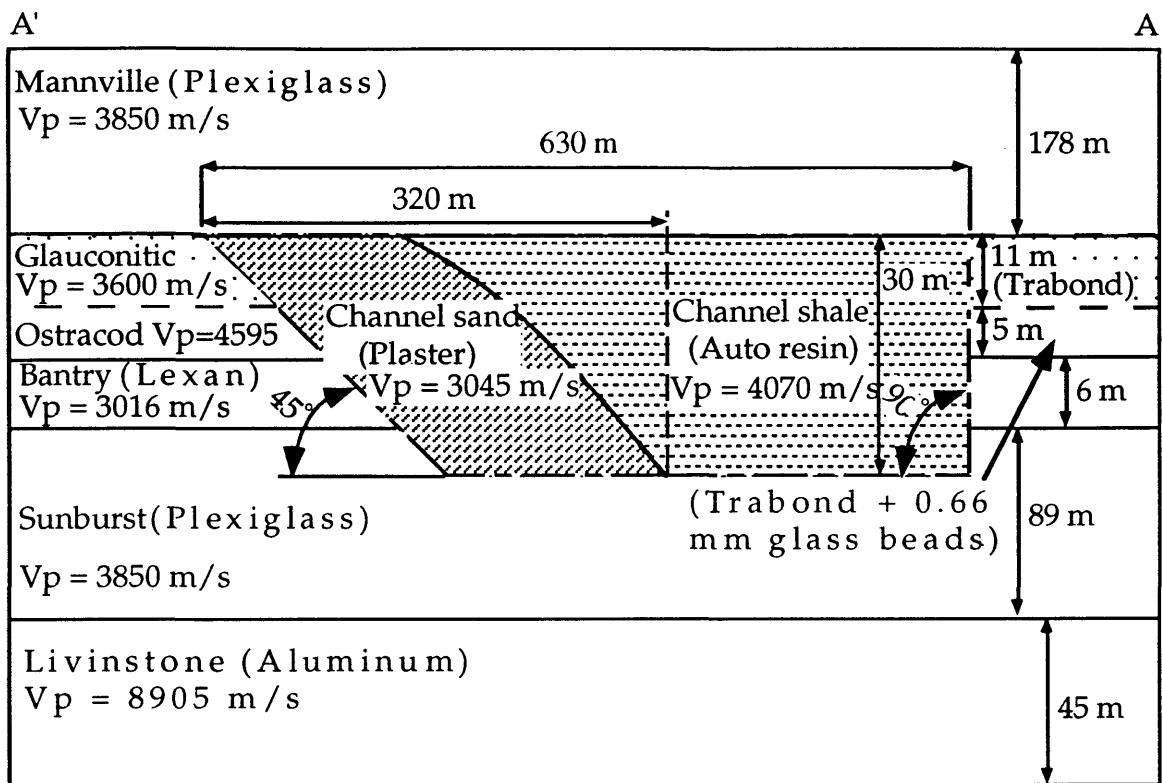
FIG 3.5 A cross section A-A' through the point bar located with respect to the physical model as shown on Figure 3.4. The bracketed names are materials used to simulate each of the different members. The indicated velocities are scaled sonic velocities of materials used to construct the physical model. The mixed dashed lines indicate the incised channel structure. The dashed line separating Glauconitic and Ostracod members indicate that both members were formed as one layer in the physical model.

Shale which is formed from a 0.079 cm thick sheet of Lexan. This Lexan sheet was bonded to the plexiglass with the acrylic glue. A slight problem occurred during the bonding of the Lexan sheet to the plexiglass and a circular high spot formed in the Lexan to the left of the point bar, as shown on Figure 3.4. Above the Bantry Shale lies the Ostracod/Glauconitic interval which was poured as one layer and this is indicated by the dashed line separating the Ostracod from the Glauconitic on Figure 3.5. The Ostracod Member was represented by a mixture of Trabond 2115 epoxy resin and 0.66 mm glass beads, in a ratio 1:1 by volume.

A pure Trabond 2115 epoxy resin represents the Glauconitic Member. Since both members were produced by using Trabond epoxy resin it was decided to form both formations with a single pour of epoxy resin. To create the Ostracod Member, a layer of 0.66 mm glass beads was placed on the model and leveled and packed so that the layer was only one glass bead thick (0.66 mm). The Trabond epoxy resin was then mixed and evacuated to remove most of the air from the resin. A wedge-shaped block was placed on top of the packed glass beads and the resin was poured gently over the block to prevent the movement of beads by the pouring of the resin. The block was then removed and the resin was allowed to level and set. This single pour of resin created a layer of resin and glass beads 0.66 mm thick (Ostracod Member) overlain by a 1.54 mm thick layer of pure resin (Glauconitic Member) as shown in Figure 3.5. The channel was then formed by cutting out a template of the channel which was clamped to the model and the channel was cut to a depth 0.43 mm with a width of 9 cm. The channel was cut so that the inside of the channel wall was tapered at a 45 degree angle while the outside wall of the channel was vertical (Figure 3.5). A channel splay with a diameter of 7.5 cm was also cut into the model at this time.

The point bar and the lateral bar were then formed out of plaster of Paris and placed in the channel. To manufacture the point bar and lateral bars, dams formed out of two-sided tape had to be placed in the channel to hold the plaster in place until it began to set. The plaster was made by mixing plaster powder with water at a ratio of 1:2 by volume. This produced a very watery mixture which was slow setting but which allowed sufficient time for shaping the plaster before it solidified. As the plaster began to set the dams were removed and shaping of the point and lateral bars began. This shaping was performed using a knife blade to carefully strip off thin pieces of plaster to avoid cracking of the

model bars. The slow removal of material continued as the plaster dried until a rough outline of the bar was formed. Final shaping was done using two templates.

The lateral bar was formed as a semi-elliptical shape, with a triangular cross-section as shown in Figure 3.4. After the plaster had dried completely, fine 600 grit sandpaper was used to shape the front surface of the point bar to a dip of about 22-25 degrees. Both bars were sealed with quick drying sealer to prevent penetration into the bars of the plastic resin used to form the channel shale. A cross section through the center of the point bar is shown in Figure 3.5.

The channel shale was simulated by plastic auto-body resin and 0.13 mm glass beads mixed 1:1 by weight. The amount of hardener added to the resin was reduced to 1/3 of that recommended as previous samples produced so much heat during setup that it cracked or crazed the surface of the resin. This reduction in hardener increased drying time of the resin from 1 hour to 10 hours but the channel shale did not crack or craze. Dams were placed across the ends of the channel at the edge of the model then the resin was slowly poured into the channel.

Once the channel shale had set a 2.54 cm thick sheet of plexiglass was bonded to the top of the model to represent the Upper Blairmore Member of the Upper Mannville Formation. Brass bolts were then inserted through the model at each corner to help maintain the model integrity when it was placed in the modeling tank.

CHAPTER 4   2-D PHYSICAL MODELING DATA

4.1 Introduction

High resolution 2-D data were acquired along a line perpendicular to and through the center of the point bar. This line was acquired to obtain a high quality seismic signature of the channel and point bar, and to evaluate the effect of sideswipe energy from out-of-plane parts of the sand body.

4.2 Data Acquisition

A 2-D high resolution survey was acquired over the model using acquisition parameters as indicated in Table 4.1. The top layer of the model was approximately 850 m (world units) below the recording plane. The 2-D line was located over the model, as shown in Figure 4.1, with the locations of the first shot (S1) and twenty third shot (S23) are indicated.

TABLE 4.1   2-D data acquisition parameters (world units)

850 m between the top of the model and the recording plane

21 m station interval

63 m shot interval

120 trace split-spread geometry

105 m near offset

1344 m far offset

4.3 Data Processing

The 2-D data were processed using ITA/Landmark software on the Sun workstation cluster at the University of Calgary. Table 4.2 lists the data processing procedure.
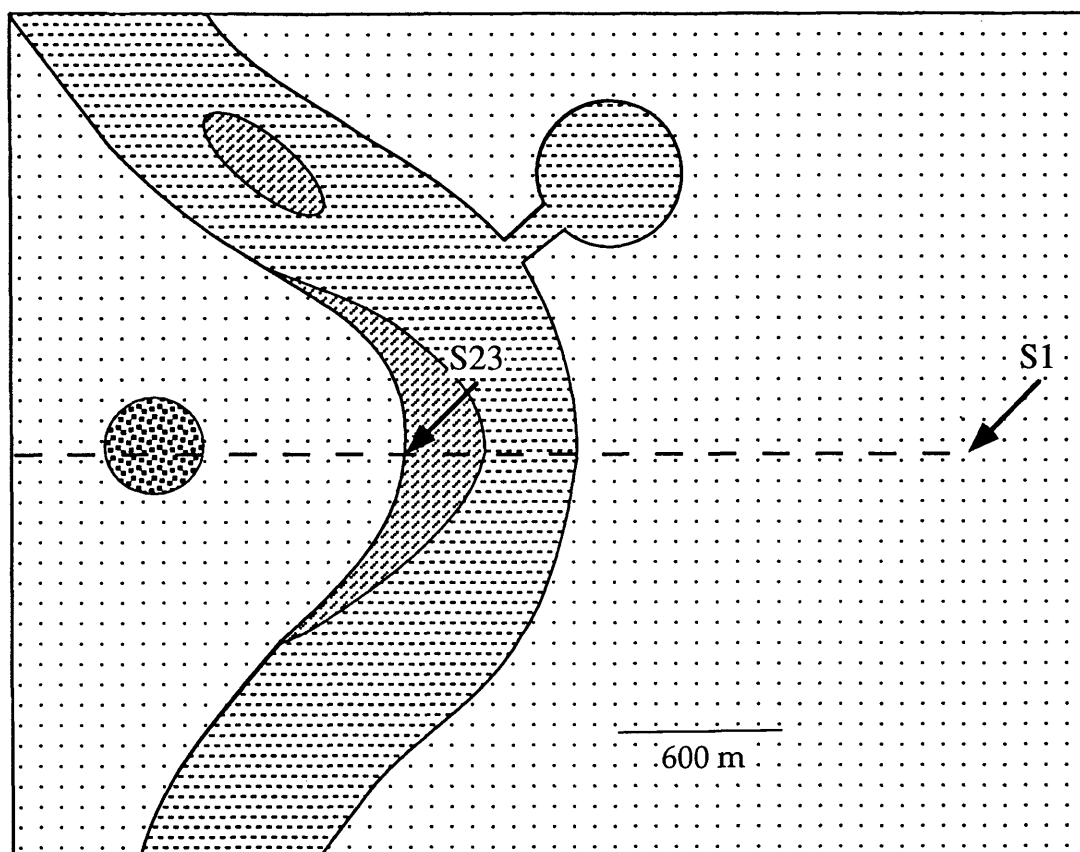
FIG. 4.1 A schematic diagram of the physical model with the top layer removed (Mannville Formation) showing the location of the 2-D line. The horizontal dashes are the channel shale, angled dashes are the point and lateral bars, dots are the Glauconitic Formation and the circle to the left of the point bar is the high spot in the Bantry shale.

Table 4.2   2-D seismic processing procedure

Geometry

↓

Flat Mute

↓

Sort Common Midpoint

↓

Velocity Analysis

↓

Normal Move Out Correction

↓

Mute

↓

Stack

↓

Bandpass Filter ⟶ Tvscale

↓   ↓

Poststack Migration   Final Display

↓

Tvscale

↓

Final Display
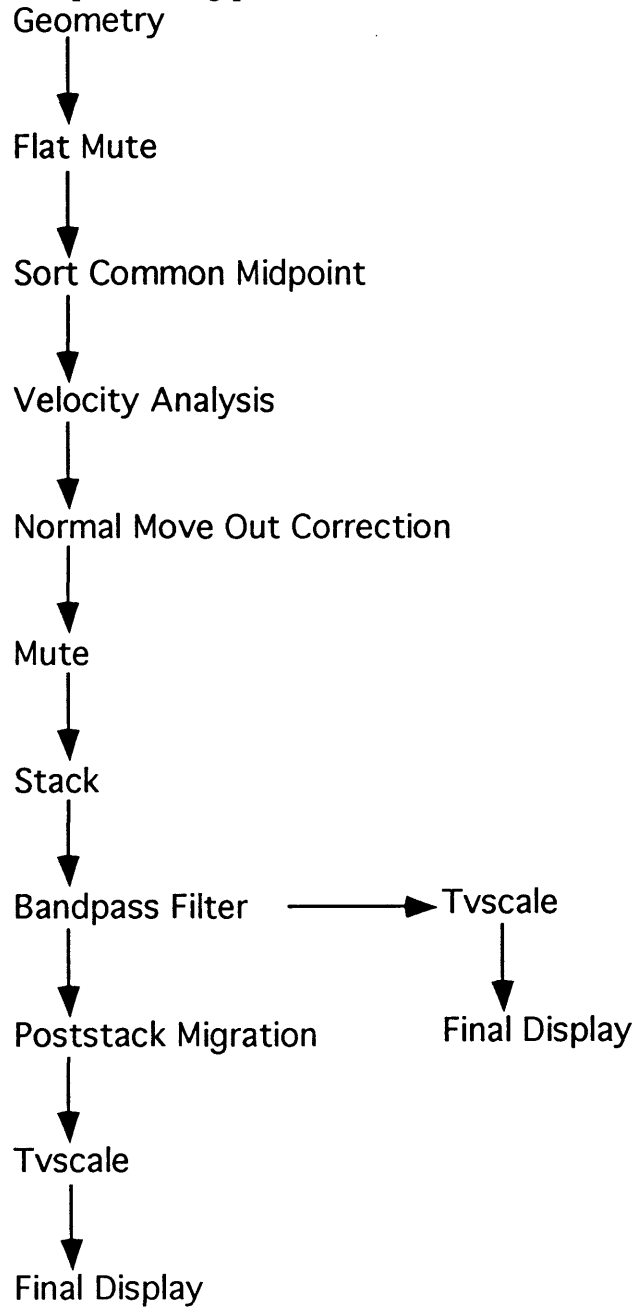
4.3.1 Geometry

The data recorded in the physical modeling tank are in trace sequential format so no demultiplexing of the data was required. The geometry update

consisted of placing the field geometry into the headers of each trace, as well as editing out any bad traces.

4.3.2 Mute

The data set was recorded in the physical modeling tank with a uniform medium (water) between the source, the model and, the receivers and a constant elevation between the acquisition plane and the model.   Therefore no elevation or weathering static corrections to the data were required. The raw data set was then muted with a flat mute (constant time) at all offsets to remove all direct-arriving energy, leaving only the reflected energy from the model. Records for shots S1 and S2 are shown in Figures 4.2 and 4.3, illustrating the muted raw shot data. These shots are displayed without any amplitude scaling or trace balancing applied. The event marked "*KM*" on Figures 4.2 and 4.3 is reflected energy from the top layer of the physical model, which represents the top of the Mannville Formation. The event marked "*M*" in Figures 4.2 and 4.3 is the reflected event from the top of the aluminum plate which represents the top of Mississippian (Livingstone Member) strata. For the data shown in Figure 4.3 the shot was located on the edge of the channel and the data images both the channel shale and the point bar. The point bar indicated by "*PB*" on Figure 4.3 produces a pull down of the Mississippian event on traces 43-48 of this record. This pull down of the Mississippian event was produced when the seismic energy passed through the channel sand which has a low P-wave velocity rather than through the surrounding material which has a higher P-wave velocity. The channel shale is indicated by "*CS*" on Figure 4.3 produces a pull up of the Mississippian event on traces 30-40 compared to the point bar because the channel shale has a higher P-wave velocity than the channel sand event. The time structural anomalies at the Mississippian event are indicative of the channel sand/channel shale event for
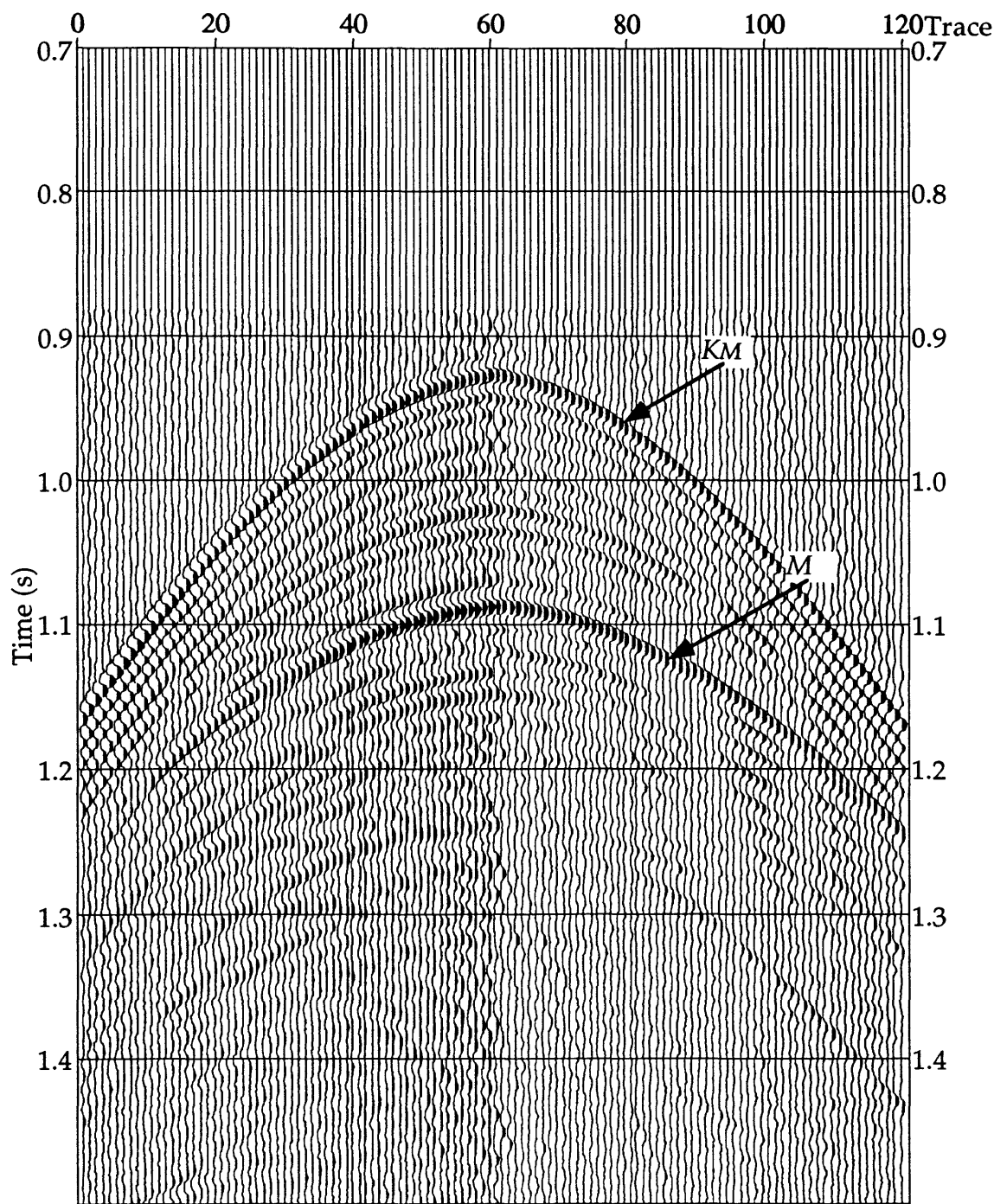
FIG. 4.2 Shot S1 of the 2-D physical modeling data set. Location of shot is shown in Figure 4.1. The events marked *KM* and *M* represent reflected energy from the top of the physical model and the top of the aluminum plate which represent the Mannville and Mississippian formations respectively.
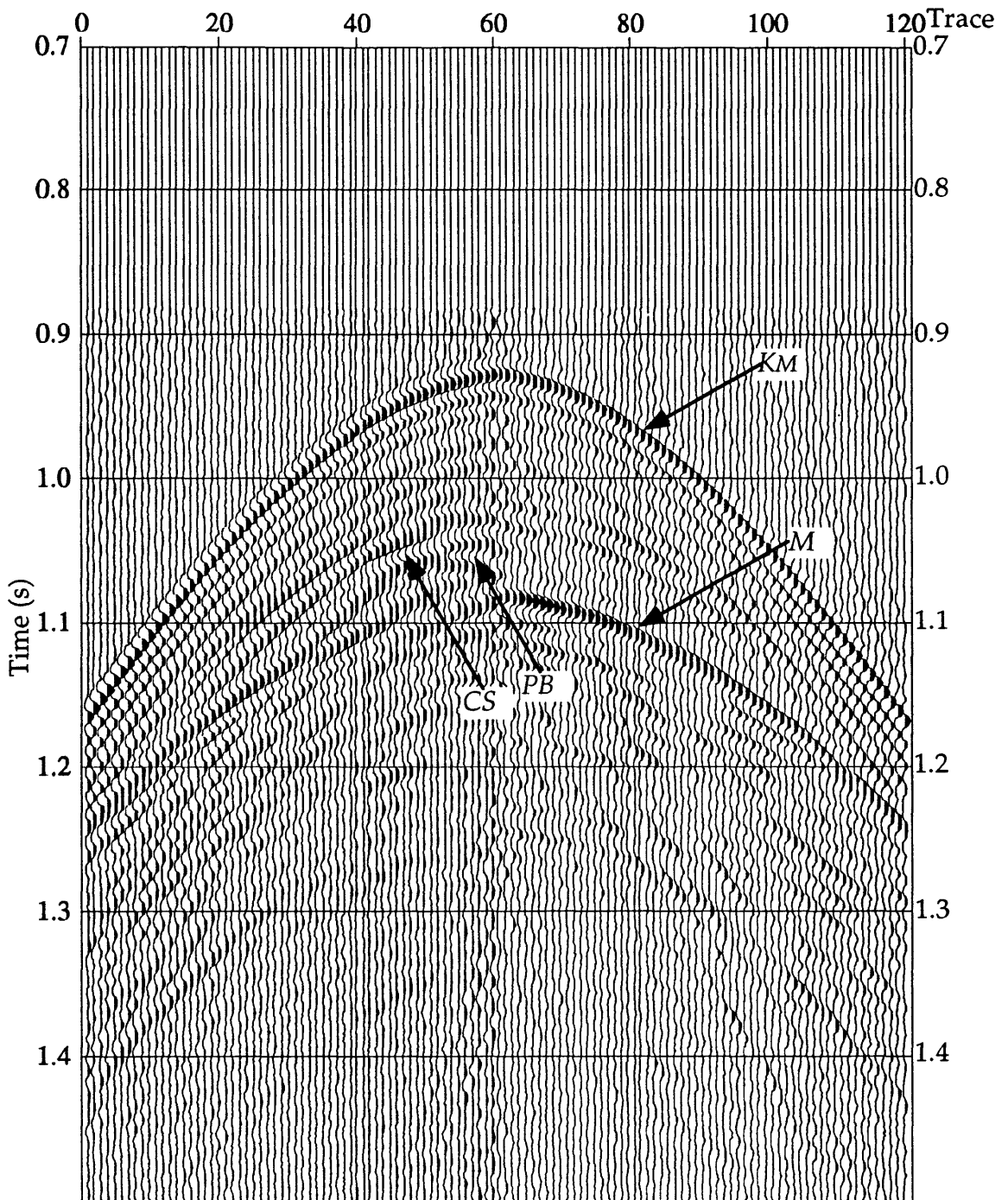
FIG. 4.3 Shot S23 of the 2-D physical modeling data set. Location of the shot is shown in Figure 4.1. The events marked *KM* and *M* represent reflected energy from the top of the physical model and the top of the aluminum plate which represent the Mannville and Mississippian formations respectively.

this 2-D data set.

4.3.3 Gather, velocity analysis

The muted records were then sorted into common midpoint (CMP) gathers and semblance velocity analysis was performed upon the gathers to determine stacking or normal move out (NMO) velocities. Table 4.3 is a comparison between stacking velocities used for processing and true rms velocities calculated from the modeling materials for CMP 745. There is a difference between the stacking velocity used for processing and true rms velocity calculated from the modeling material, but this is not unusual because a lot of the materials from which the physical model is constructed are composite materials made by mixing together other pure materials. The velocity was measured by taking a sample of each of the composites and measuring its velocity, but this assumes there is perfect mixing of samples so that the composite material is uniform in composition through the whole volume of the material.

Table 4.3   RMS. velocities for CMP 745

Time (s)	Stacking velocity (m/s)	Calculated RMS. velocity (m/s)
0.921	1896	2086
1.018	2121	2320
1.025	2128	2323
1.080	2224	2546

Figures 4.4 to 4.6 are normal move out (NMO) corrected CMP gathers located on one side of the channel, over the channel and on the other side of the channel respectively. The event marked "*KM*" at approximately 0.92 s in Figures 4.4 to 4.6 is the reflection from the top of the model (Mannville Formation), peak
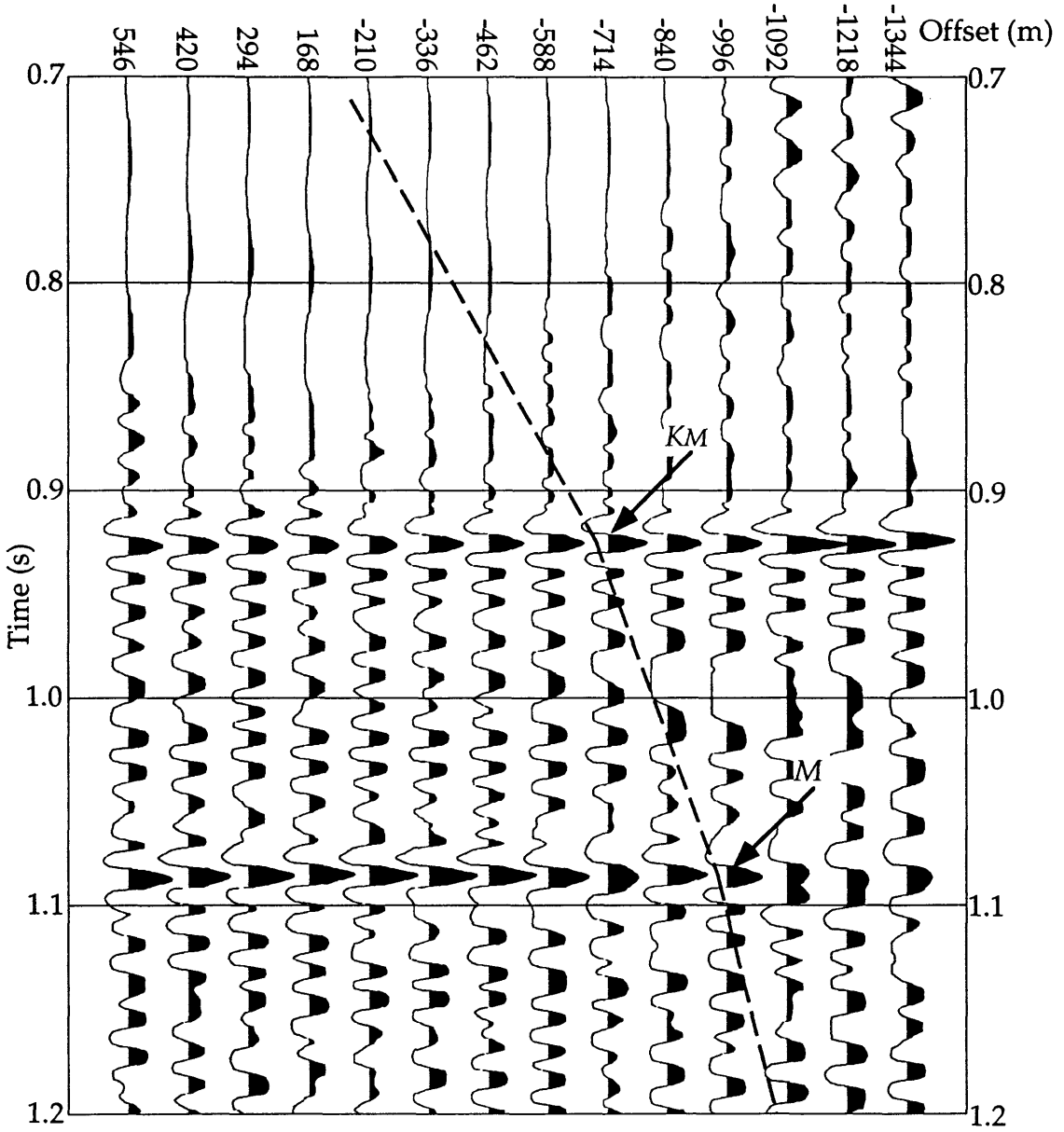
FIG. 4.4 CMP 780 from the 2-D physical modeling data set. The events marked *KM* and *M* represent reflected energy from the top of the physical model and the top of the aluminum plate which represent the Mannville and Mississippian formations respectively. The dashed line indicates the location of the mute which was applied to the stacked data set.
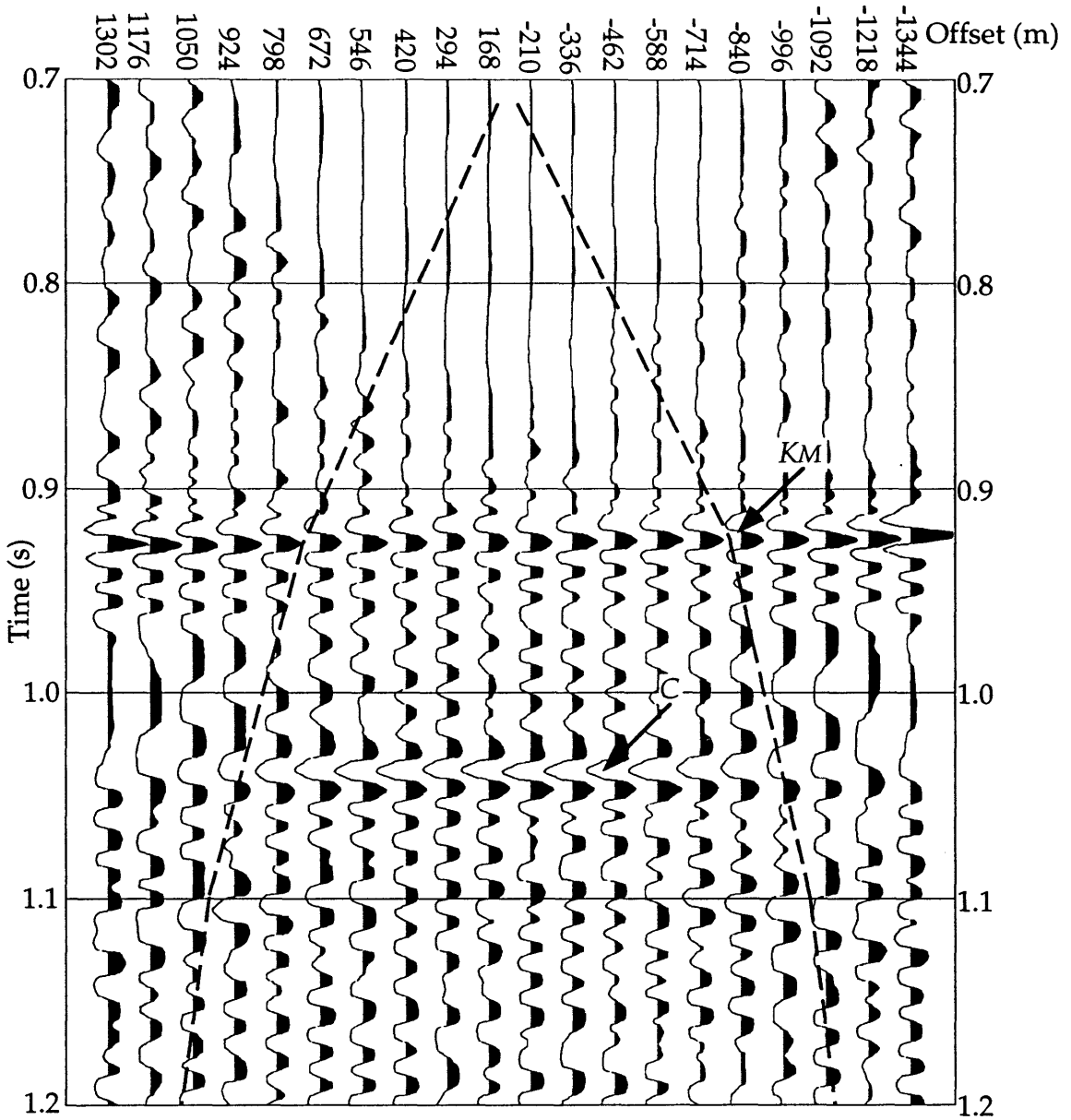
FIG. 4.5 CMP 1230 from the 2-D physical modeling data set. The events marked *KM* and *C* represent reflected energy from the top of the physical model and the channel which represent the Mannville Formation and channel shale respectively. The dashed lines indicates the location of the mute which was applied to the stacked data set.
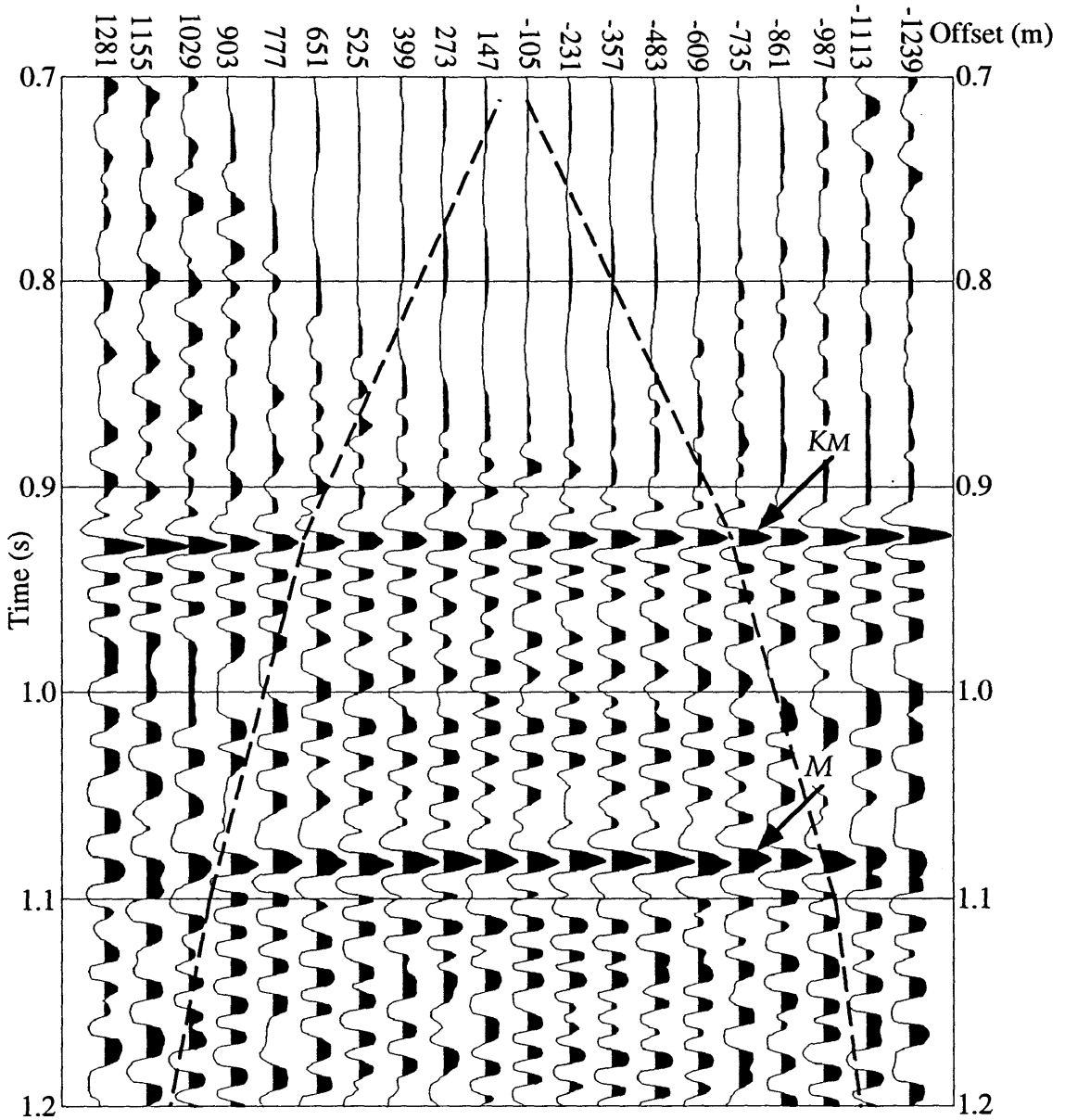
FIG. 4.6 CMP 1405 from the 2-D physical modeling data set. The events marked *KM* and *M* represent reflected energy from the top of the physical model and the top of the aluminum plate which represent the Mannville and Mississippian formations respectively. The dashed lines indicates the location of the mute which was applied to the stacked data set.

marked "M" at 1.08 s is the reflection from the top aluminum plate (topMississippian strata). There is a high-amplitude peak-trough-peak event at 1.02 s on Figure 4.5 (indicated by "C" on this figure) which represents the channel event. The reflectivity of the channel reduces the amplitude of the top of the Mississippian Formation event at 1.1 s.

There is some frequency distortion of events at large source-receiver offsets in Figures 4.4 to 4.6 and this is caused by NMO stretch, as discussed by Yilmaz (1987). The distortion occurs mainly between 0.95 and 1.05 s and tends to change the events to having lower frequencies. This distortion is eliminated by applying a second mute (dashed lines on Figures 4.4 to 4.6) to remove distorted events from the CMP gathers.

4.3.4 Stacking

The remuted traces within each NMO gather were then stacked to produce one zero-offset trace for each gather. The stack procedure in the ITA software sums together the amplitudes of all traces in the gather at a certain time sample and then divides the sum by the number of live traces in the gather. Stacking the gather results in a improved signal to noise ratio by canceling random noise. Figure 4.7 shows the stacked section of the 2-D physical modeling data set. This section shows a high-amplitude peak from the top Plexiglas (Mannville Formation) at 0.92 s and a high-amplitude peak from the top of the aluminum plate (Mississippian Formation) at 1.085 s. The events between these two high amplitude peaks are relatively weak compared to these two events so a time-variant gain factor was applied to the stacked data. This scaling boosted the amplitudes of events between top of the Plexiglas and the top of the aluminum plate. Normal incidence reflection coefficients were calculated for all of the interfaces in the physical model and it was found that the top of the
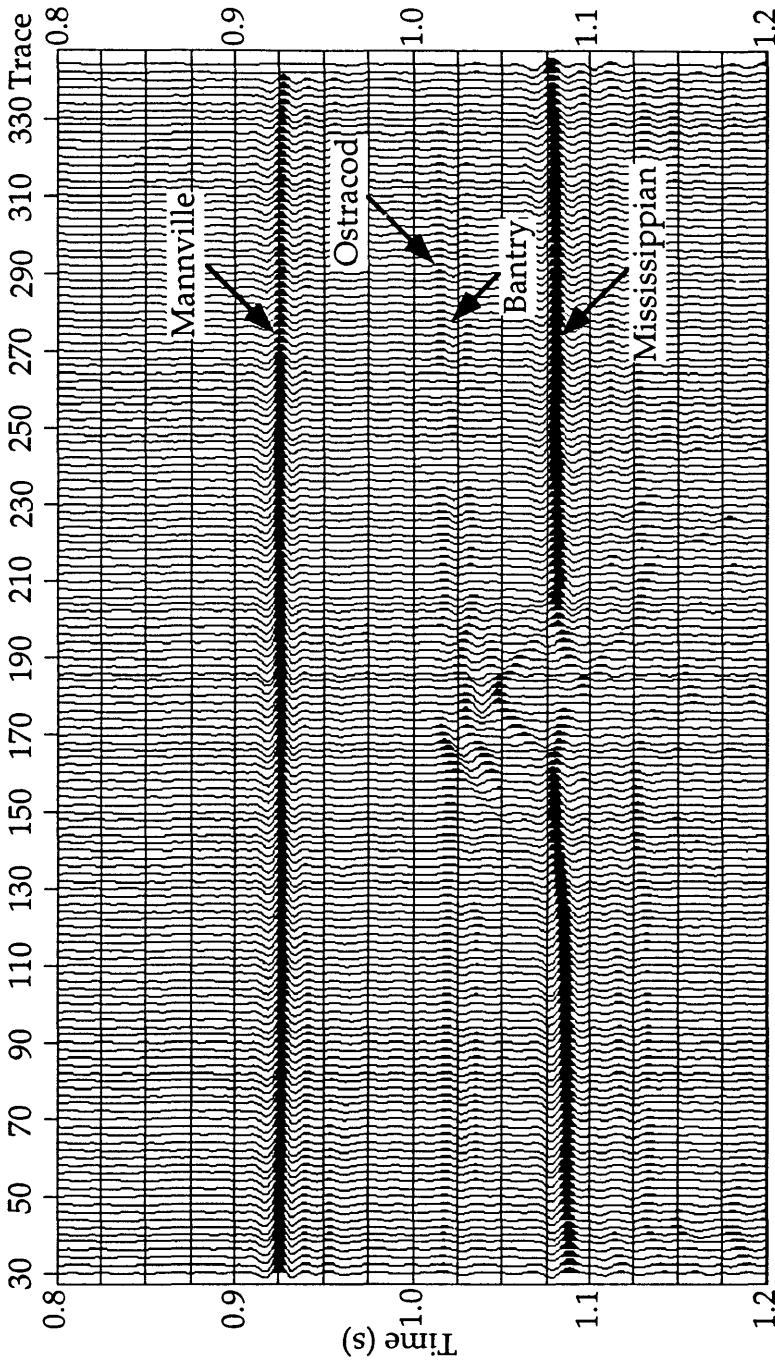
FIG. 4.7 Stacked section from 2-D physical modeling data set. The trace spacing is 10.5 m in world units.

Mississippian, top of the Bantry and top Mannville have strong reflection coefficients whereas the other layer boundaries have small reflection coefficients. The final stacked section, with the time-variant gain, is shown in Figure 4.8

The Mannville event is at approximately 0.92 s on the stacked section (Figure 4.8). It is a fairly strong amplitude peak with good continuity across the section. The next most obvious events on this section are the peak and trough doublet that occurs at 1.015 s and 1.02 s, which represent the Ostracod limestone and the Bantry shale respectively. There is a weak peak directly below the Bantry trough which represents the top of the Sunburst Formation. The strong peak at 1.085 s represents the Mississippian event. The strong trough of the Bantry shale and weak Sunburst peak disappear approximately at trace 140 on the stacked section, and this is interpreted to indicate the start of the channel on this section. This disappearance of this trough-peak doublet also corresponds to the location where pull-up of the Mississippian event is evident, caused by the high-velocity channel shale. There is a distortion in the peak-trough doublet on traces 240 to 266 and this distortion is produced by the high spot in the Bantry shale on the physical model. There is a weak dipping event between traces 166 and 180 occurring between 1.015 and 1.04 s, which is a reflection from the top of the point bar. This event appears to level out at 1.015 s at trace 180 and it can be followed to trace 194 where it appears to merge into the Bantry event. The dipping event below the top of the point bar probably represents the dipping inside edge of the channel. The point bar seems to attenuate all the energy passing through it so there appears to be a break in the Mississippian reflector below the point bar and there are diffractions produced off each side of the gap.
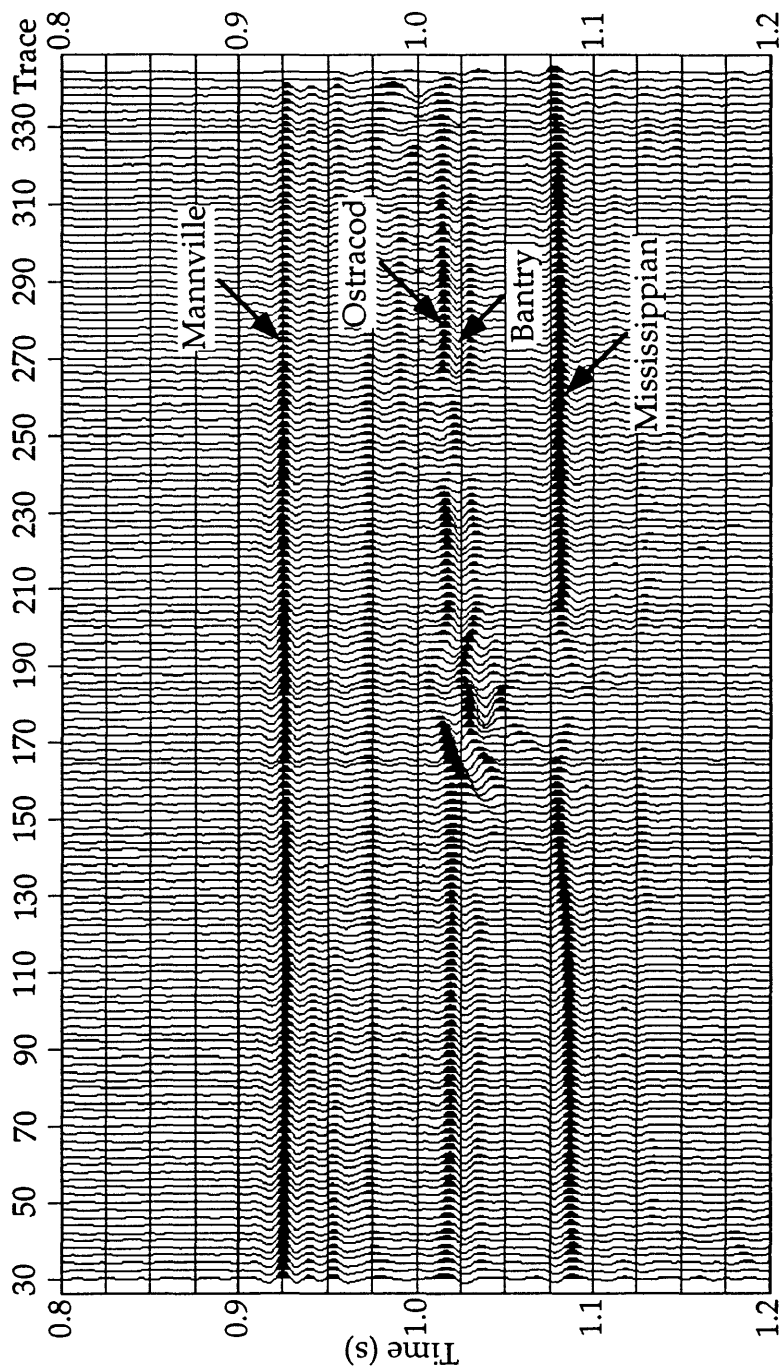
FIG. 4.8 Time-variant gained stacked section from 2-D physical modeling data set. The trace spacing is 10.5 m in world units.

<u>4.3.5 Migration</u>

The stacked section Figure 4.7 was migrated to collapse diffractions and move dipping reflectors to their true subsurface position (Yilmaz, 1987). In Figures 4.7 and 4.8 diffractions can be observed from the channel structure between 1.0 to 1.1 s on traces 150 and 200. Various migration methods were tested, including f-x migration, finite-difference migration and a phase-shift migration. The migrated sections had the same amplitude problem as the stacked section so a similar time-variant gain was applied to the migrated sections as was used for the stacked sections. Figures 4.9 to 4.11 show the migrated and gained sections for the 2-D physical modeling data.

The three time-migrated sections (Figures 4.9 to 4.11) have a very similar appearance. Each migration scheme has collapsed the diffractions which occur at the margins of the channel on the unmigrated stacked section. However each of these sections also has a slight hint of a diffraction remaining on the left side of the gap in the Mississippian event. This may be caused by the lateral variation in the velocity of the channel fill as the point bar increases in thickness. The three migration algorithms image the point bar very well and it is possible to follow the point bar reflection up the front slope of the point bar and across the flat top of the bar. The reflection from the top of the bar then merges with the Bantry event.

The major difference between these migration methods is the time for each algorithm to execute. Using the same input data set the phase-shift migration migrates the data in approximately 1.5 minutes while the f-x migration takes about 7 minutes and the finite-difference migration takes approximately 30 minutes. These times are all based on running each of the migrations on a Sun SPARCstation 2 .
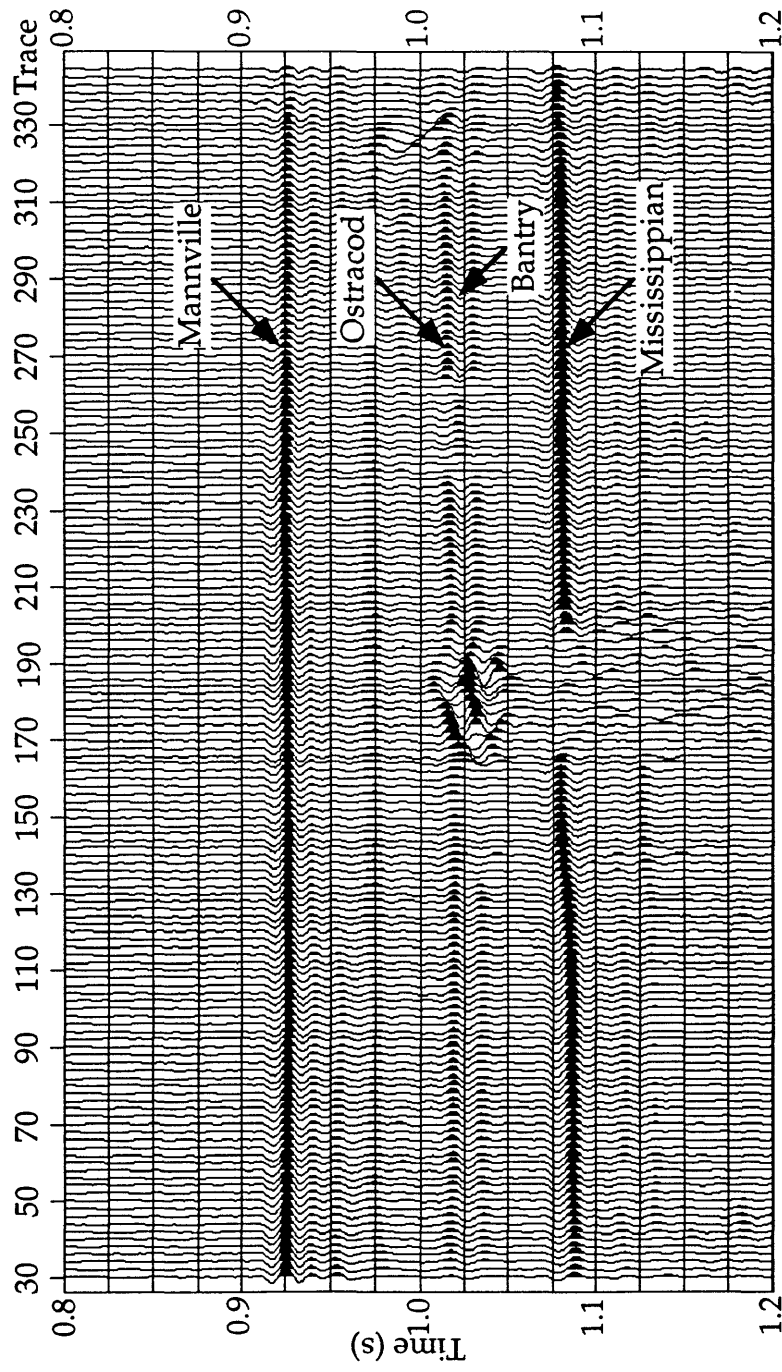
FIG. 4.9 Time-variant gained F-X migrated section from 2-D physical modeling data set. The trace spacing is 10.5 m in world units.
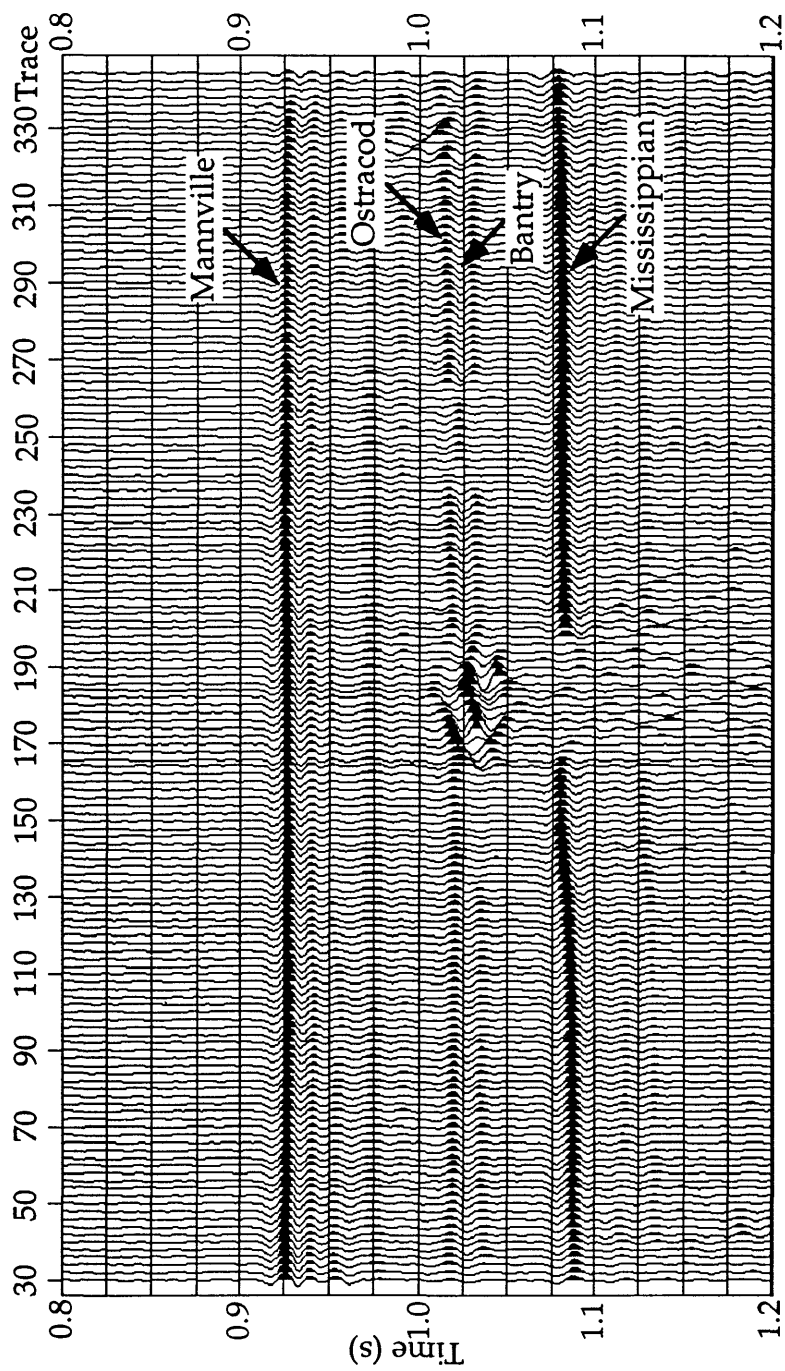
FIG. 4.10 Time-variant gained finite-difference migrated section from 2-D physical modeling data set. The trace spacing is 10.5 m in world units.
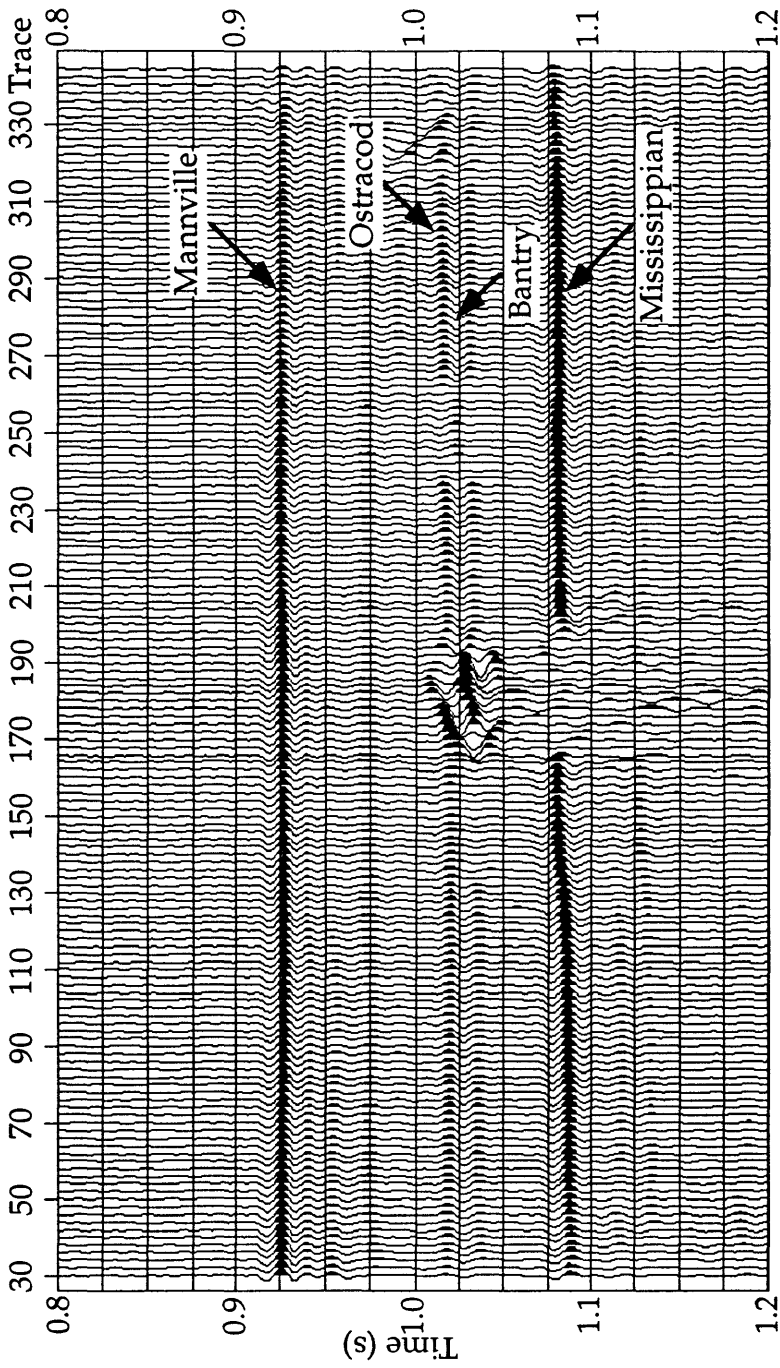
FIG. 4.11 Time-variant gained phase shift migrated section from 2-D physical modeling data set. The trace spacing is 10.5 m in world units.

There appears to be no significant change in the amplitude of the dipping reflection on either the migrated or unmigrated sections as the point bar thickens from 10 to 30 m. This observation seems to reinforce the observation made by Noah (et al., 1992) that the sideswipe energy is so strong that there is no variation in reflection amplitude from the point bar as the bar varies in thickness. Noah (et al., 1992) used a 3-D seismic model of the Larmie River (T17-18N, R74W, Wyoming) to analyze the seismic response of high-velocity sand point bar deposits enclosed in lower velocity shales to uncover the interpretation pitfalls in 2-D seismic data. They found in this study that as the sand body varied in thickness from 10-30 ft there was nearly an identical seismic amplitude response for the sand body. Noah attributed this lack of variation in amplitude response to variation in sand body thickness as a Fresnel zone effect from parts of the sand body which may not directly lie under the 2-D line but may still lie within the Fresnel zone radius.

CHAPTER 5   3-D SEISMIC ACQUISITION DESIGN

5.1 Introduction

The acquisition of 3-D seismic surveys requires careful planning of the layout of receiver and shot lines to provide the explorationist with data which will produce the best possible image of the geological target. Optimum 3-D survey design occurs when the parameters controlling costs, such as field hardware utilization and geophysical constrains, have been simultaneously optimized while obtaining the necessary resolution of the geological target (Crews et al., 1989).

To optimally design a 3-D survey to image a geological target, it is necessary to determine the minimum sampling of the subsurface which will produce an interpretable seismic data volume. Some 3-D surveys have been designed with subsurface sampling which yields some empty CMP bins which are later filled by interpolation during data processing. This interpolation of empty bins violates the principle of uniform subsurface sampling and it is preferable that subsurface sampling be uniform in all directions (Crews et al., 1989). Other factors which affect design of 3-D surveys include: bin fold, offset distribution of traces within bins, and source-receiver azimuthal distribution within each bin. The bin fold distribution in a 3-D survey is approximately equal to the product of the inline and crossline 2-D fold which are indicated by equations 5.1 and 5.2. The fold in each bin will affect the signal to noise ratio and ability to determine velocity distribution for proper normal move out (NMO) correction. Regular offset distribution within the bin is desired in order to determine a stable velocity field, to have coherent noise cancellation in stack and to attenuate multiples (Ritchie, 1991). A wide range of offsets in each bin is beneficial in seismic data processing of 3-D surveys. Short offsets in adequate

number are necessary for shallow exploration targets and for shallow velocity determination in refraction analysis. Long offsets are required to determine robust stacking velocities and deeper refractor velocities for long-wavelength statics analysis. If the range of offsets is limited, it may produce aliasing of dipping events, shot noise and failure of velocity analysis (Galbraith, 1994). A uniform distribution of source-receiver azimuths is also required to provide robust refraction static corrections and to help detect azimuthal-dependent variations from dipping horizons or from certain types of anisotropy (Galbraith, 1994).

$$\text{Inline 2-D fold} = \frac{R \times RI}{4 \times SL} \qquad\qquad 5.1$$

$$\text{Crossline 2-D fold} = \frac{RL \times RS}{4 \times SI} \qquad\qquad 5.2$$

R = number of receivers in each line of the receiver patch
RI = receiver interval
SL = source line spacing
RL = number of receiver lines in the receiver patch
RS = receiver line spacing
SI = source spacing

Another consideration in designing a 3-D program is the area to be encompassed by the survey. The size of the 3-D survey must be large enough to adequately image the subsurface area of interest, taking into account geological dips, proximity of the target to survey boundaries and area where full fold is required (Hawthorne and Webster, 1989). It is important to have a sufficiently large migration aperture around the perimeter of the survey to capture energy scattered outward from the center of the survey, so that migration can move the energy to the correct location on the time section. The migration distance required from the anomaly to the edge of survey can be calculated by the following formula (Hawthorne and Webster, 1989):

$$xmig = z \cdot \tan(\alpha)$$

α = dip picked from migrated data
z = depth to the anomaly
$xmig$ = required distance

5.2 Historical Summary of 3-D Acquisition

The invention of the 3-D seismic survey brought about a new era in seismic acquisition in the mid 1970's. A 3-D survey provides an areal picture of the subsurface instead of just imaging the subsurface beneath a profile line, as in the case of the 2-D method.

The first 3-D survey was acquired in the early 1970's (Bukovics and Nooteboom, 1990). The goal for 3-D acquisition at this time was to record seismic waves, impinging on the surface of the earth over a wide area, coming from single shot (Walton, 1972). A single shot produces only a limited area of subsurface coverage so two alternative schemes were developed. The first scheme was to use source points over a large area (typically 4 square miles), shooting into a central patch of geophones. Figure 5.1 delineates the field layout used on some early 3-D surveys (Walton, 1972). In this layout, there are 48 source lines with evenly spaced source locations over a 4 square mile area producing subsurface coverage of 1 square mile.

An alternative scheme developed for 3-D data acquisition was the crossed-array or crossed-spread. This array consists of a single line of shots which are orthogonal to a single line of geophones (Figure 5.2). This scheme produces single-fold areal coverage, as shown in Figure 5.2. The sources and geophones have the same spacing to provide an even grid of depth points. This method was soon expanded to include sources firing into multiple receiver lines.
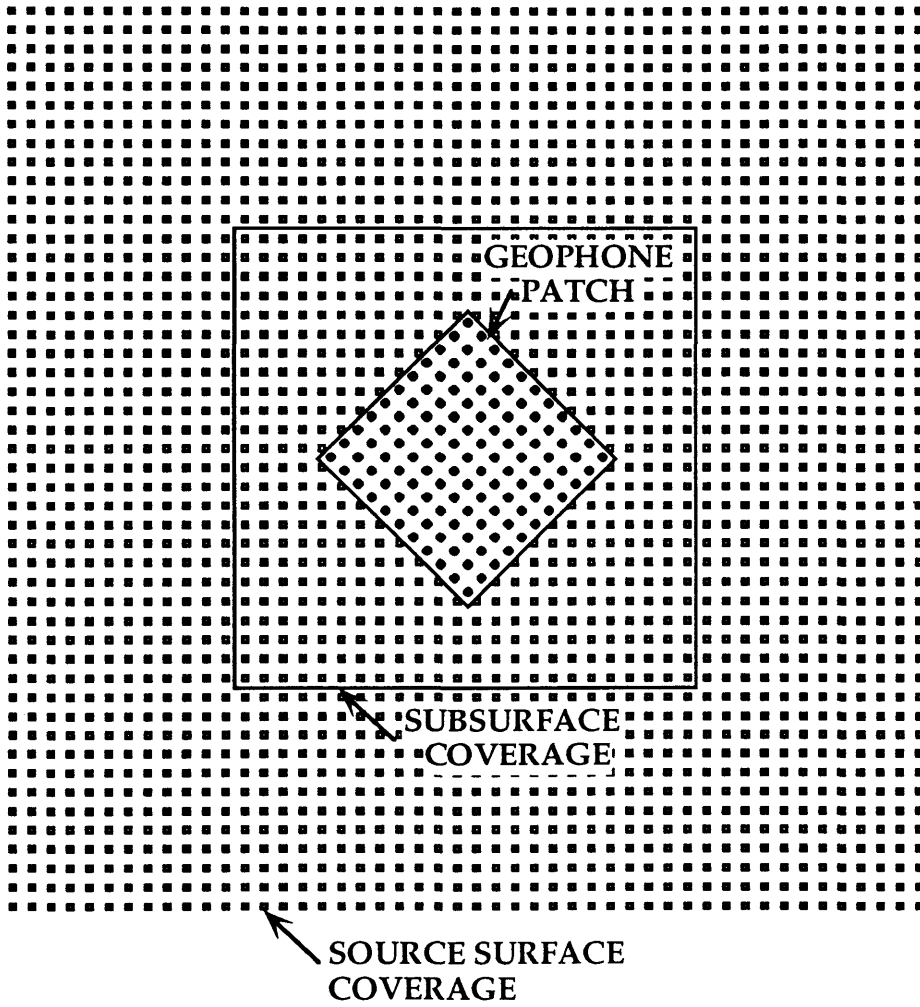
FIG 5.1 Early 1970's 3-D acquisition method using source points over a large surface area shooting into a central patch of geophones (Walton, 1972).
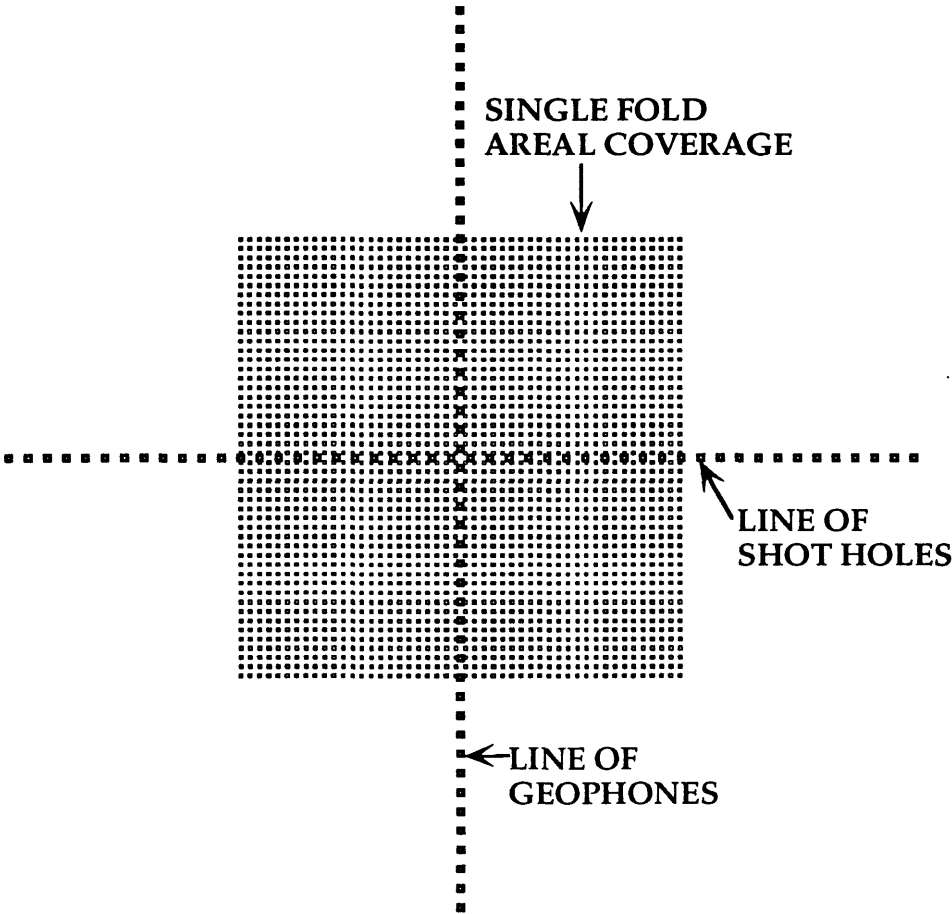
FIG. 5.2 Crossed-array or crossed-spread 3-D acquisition technique using a single line of shots into a single line of geophones to produce single-fold subsurface coverage.

In 1973, the first commercial 3-D program was acquired in New Mexico for a consortium of oil companies. This survey was acquired using a simple swath technique. The swath technique of acquisition uses a series of closely spaced, parallel receiver lines to form a long narrow receiver patch. A small number of sources, which lie along an orthogonal line to the receiver lines, are fired into the receiver patch. This type of acquisition technique provides a series of parallel subsurface lines with consistent fold. Since there are only a few receiver lines active for each shot, this tends to develop high fold along the receiver line (in-line direction), but limited fold in the crossline direction (Ritchie, 1991). This limited crossline fold and the fact that subsequent swaths are not coupled led to discontinuities at swath boundaries. The solution to this problem was to acquire overlapping swaths, with subsequently improved fold development in the crossline direction as well as improved crossline coupling. This type of 3-D acquisition program established the usefulness of 3-D surveys for accurately imaging subsurface features, but it was not operationally feasible in many areas of interest due to constraints of surface access.

The problem of surface access led to development of the Seisloop technique and other loop techniques (Figure 5.3) which provided areal subsurface coverage by placing sources and receivers around the boundary of the area of interest. However, the loop technique produced highly variable fold, irregularity in offset distribution and highly variable azimuth distribution. Each of these is an undesirable parameters for 3-D acquisition design.

In the early 1980's, a multi-cable swath technique became the scheme of choice for acquiring 3-D surveys (Figure 5.4). This technique provided consistent adequate fold and a better range and azimuthal distribution of offsets compared to the single-cable swath method. The multi-cable swath technique
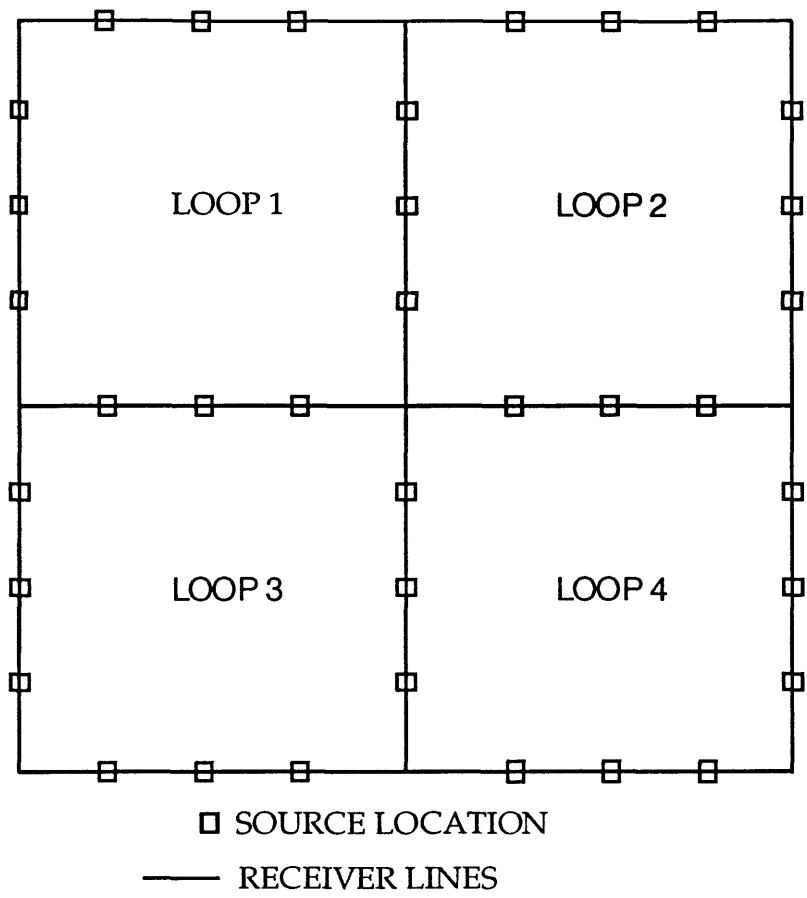
FIG. 5.3 Seisloop or loop technique of seismic acquisition.
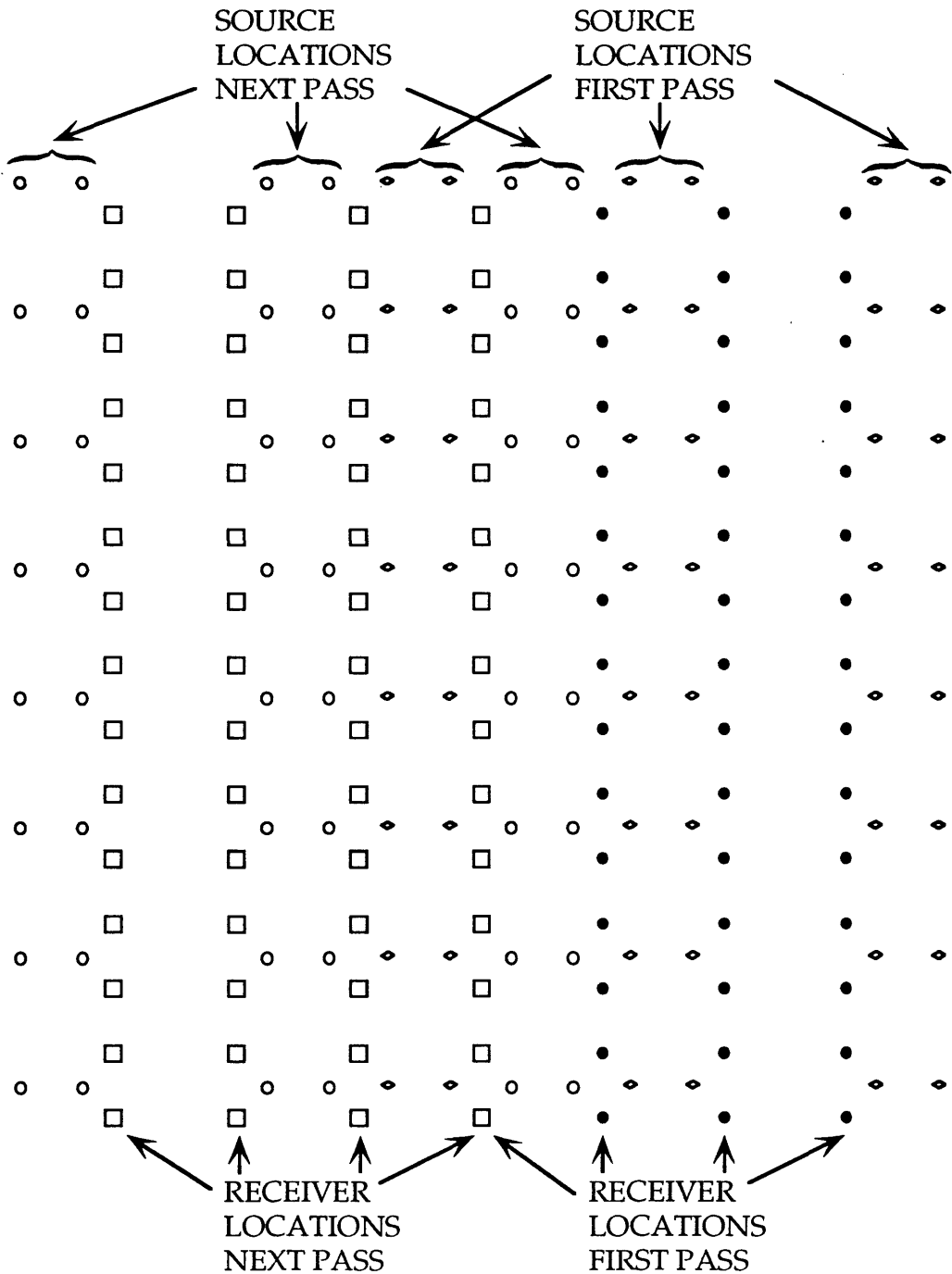
FIG. 5.4 Multi-cable swath using four receiver cables and six shot lines generating two-fold cross-line cmp and six fold in line if 24 receiver locations are used. Roll 3 cables per pass. (Lansley, 1993).

brought about improvements in crossline fold, but the longer offsets still tended to cluster in the inline direction (along receiver lines), which continued to cause problems with crossline stability of the near-surface static solution. This static problem was a result of the desire to limit large variations in azimuth distribution because the NMO velocity may vary as a function of azimuth between source and receiver. Thus, a survey which had a large variation in azimuth required a 3-D NMO solution which was unavailable at that time.

During the mid 1980's telemetry acquisition systems allowed large receiver/shot ratios and wider crossline spread apertures. This wider crossline aperture also provided better static solutions. The 1990's continued the 1980's trend of more channel telemetry recording systems which allowed larger and larger receiver/shot ratios. This reduced acquisition cost by increased utilization efficiency of field equipment.

5.3 3-D Acquisition Layout Strategies

The easiest and most common 3-D survey technique in land acquisition is the straight-line method (Figure 5.5) in which source and receiver lines are orthogonal. This method is easy to lay out in the field and allows a straight-forward roll along of the receiver patch. To acquire data with this method, all shots between adjacent receiver lines in the center of the receiver patch are fired, then the patch is moved over one receiver line and the process is repeated. The advantage of the method is that the geometry for processing is simple. The disadvantage of this method is that the minimum offset in the bin which lies in the center of the grid (box) formed by adjacent shot and receiver lines may be quite large. In a 3-D survey, this center bin will contain contributions from many shot-receiver pairs, but the shortest offset trace belonging to that bin will be largest minimum offset of the entire 3-D survey (Galbraith, 1994). This shortest

1:0   0.4

XM 0
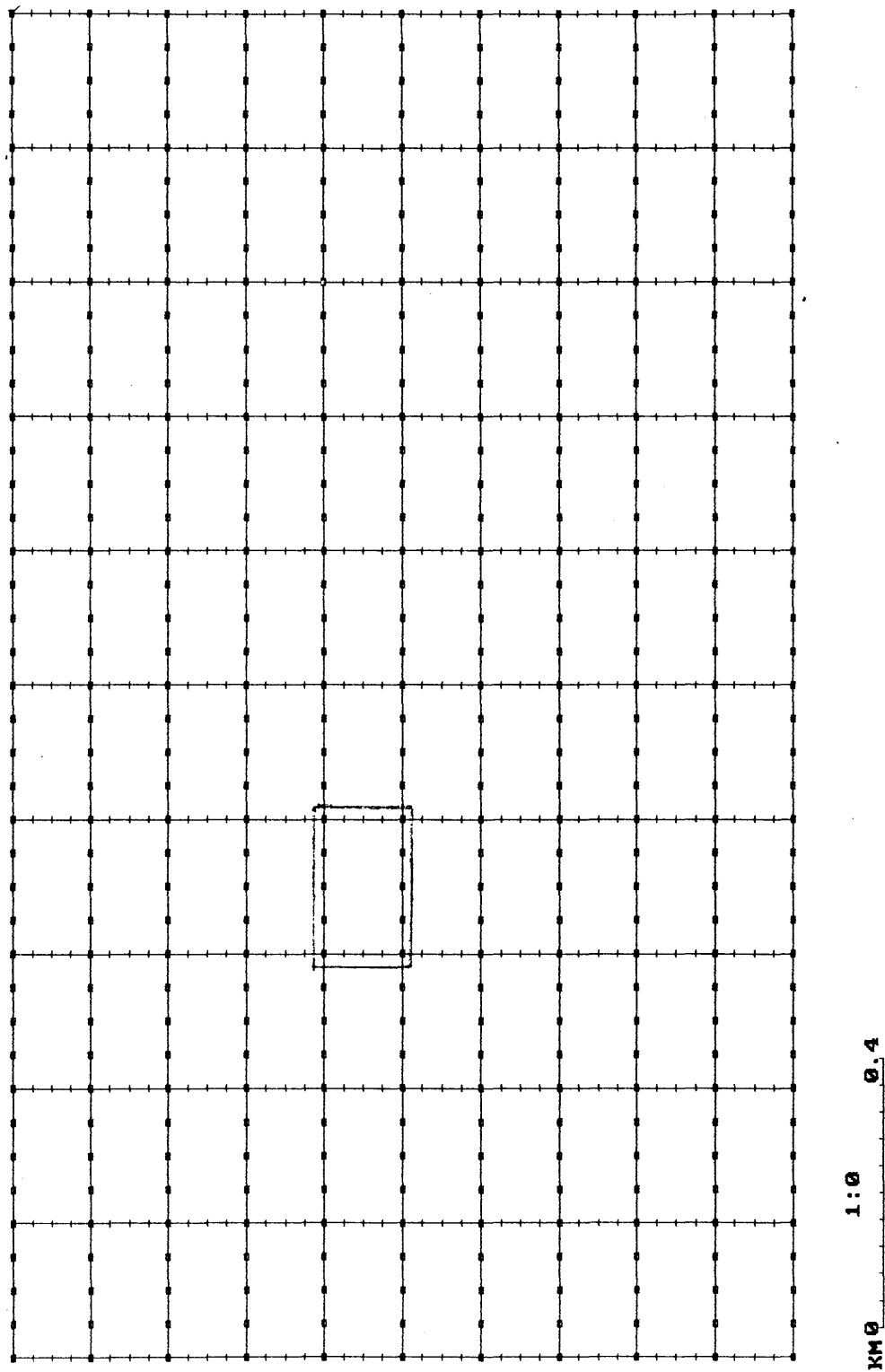
FIG. 5.5 Straight-line method of 3-D acquisition (+ = receiver locations, □= shot locations). Small rectangular box is used for offset and azimuth analysis.

offset trace is equivalent to diagonal of the box formed by adjacent shot and receiver lines.

To examine the offset, azimuth and fold distribution produced by the straight-line method of acquisition, a 3-D survey was modeled using Seismic Image Software's Field Design software. The model consisted of a 2000 by 2000 m survey with 200 m source and receiver line spacing and 50 m source and receiver intervals. A 2000 by 2000 m receiver patch was used to acquire data for this survey. The offset and azimuth distribution in the bins were examined for this acquisition method using a small spatial area in the center of the survey for 3 offset ranges; a near range 0-500 m, a mid range of 500-1000 m and a far range of 1000-1500 m. The fold distribution were examined over the full survey area for all three ranges of offset.

Figure 5.6 illustrates the offset distribution for the near-offset range (0-500m) for the straight-line acquisition method. The largest near-offset, which is 282 m, occurs in the bin (marked A in Figure 5.6) in the center of each box formed by adjacent source lines (S in Figure 5.6) and receiver lines (R in Figure 5.6). There are two orthogonal strips (indicated by B on Figure 5.6) through the bin marked A parallel to source and receiver lines which have a sparser offset sampling then the rest of the bins in the 3-D survey. Figure 5.7 illustrates the azimuth distribution for the near-offset range. The length and direction of each arm of the cross in the bins on Figure 5.7 represent a source/receiver offset in that bin and receiver azimuth from the source respectively. The azimuth distribution on Figure 5.7 has a sparse azimuth distribution in the bins in the center of the boxes formed by the adjacent source and receiver lines. Azimuth distribution declines from 6 azimuths along source and receiver lines to 4 uniform offset azimuths in the center of the box. The fold distribution (Figure
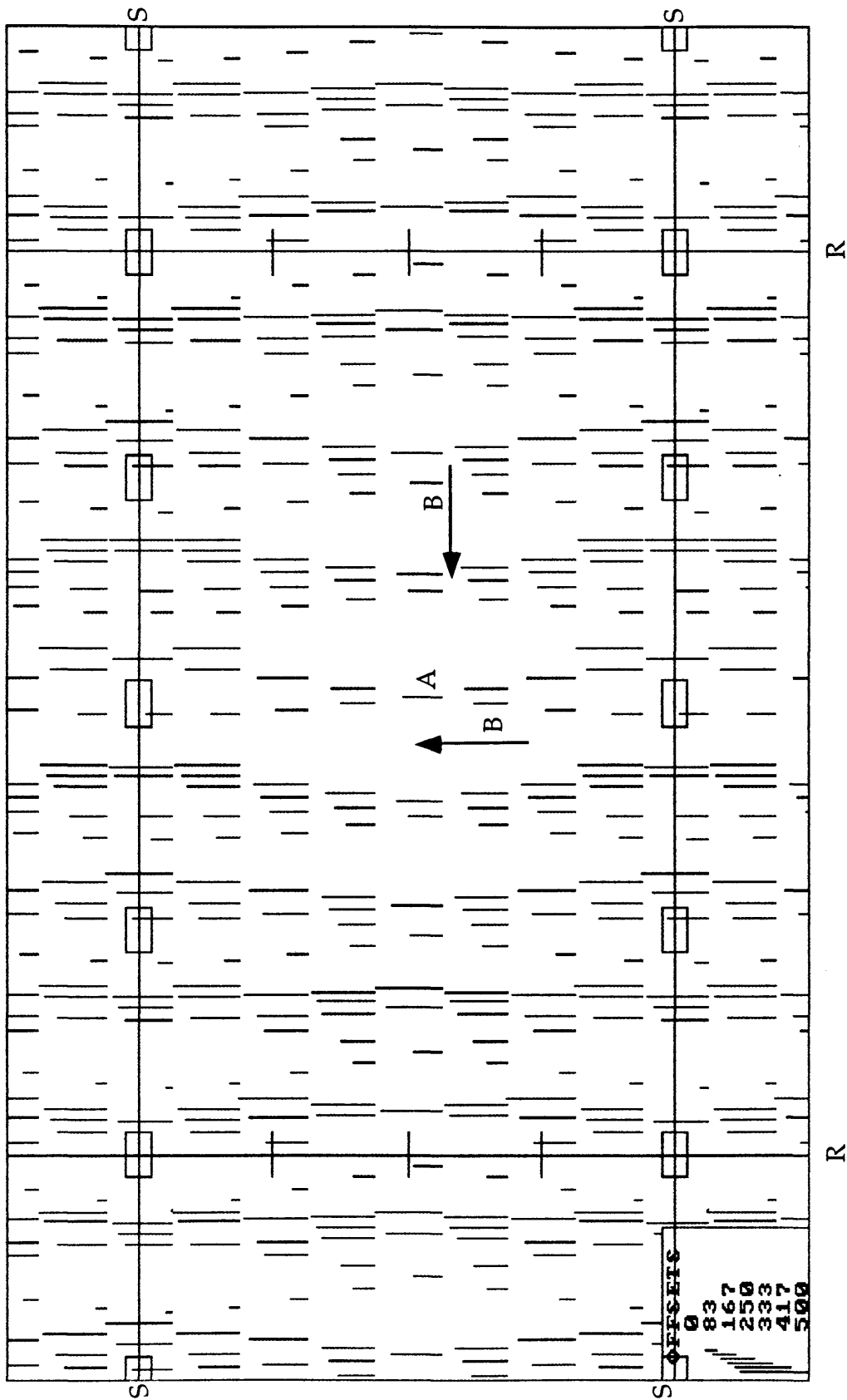
FIG. 5.6 Offset distribution for the near-offset range for the conventional straight-line 3-D acquisition method. The bin size is 25 X 25 m.
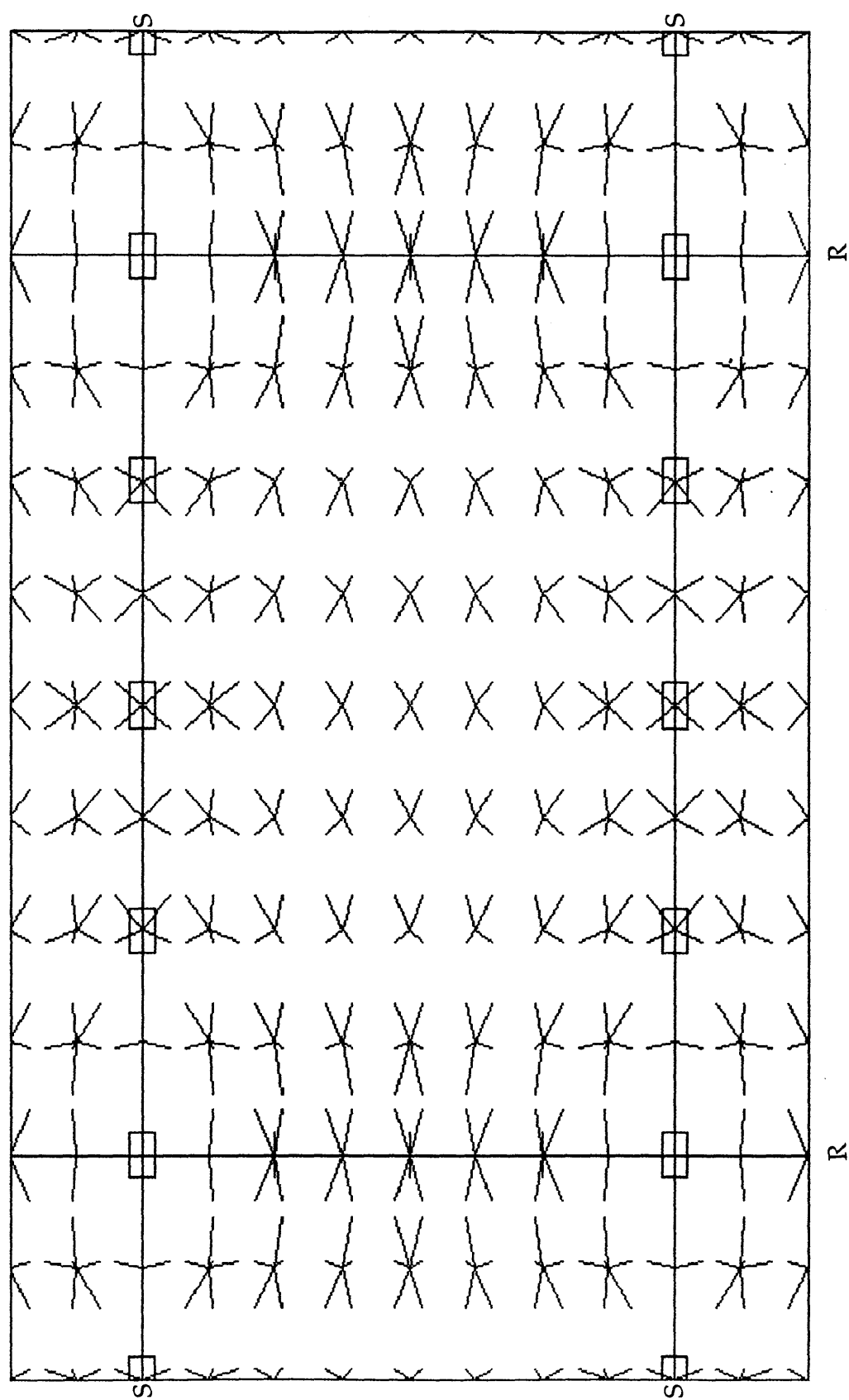
FIG. 5.7 Azimuth distribution for the near-offset range for the conventional straight-line 3-D acquisition method.

5.8) is fairly constant and averages about 4-6 fold for the near-offset range. Figure 5.9 shows the offset distribution for the mid-offset range, and shows that the offset distribution is more uniformly sampled than the near-offset range. The azimuth distribution (Figure 5.10) is uniform over the entire area for the mid-offset range. Fold distribution (Figure 5.11) is fairly uniform and average fold ranges from 12 to 15 fold.

A poor offset distribution is observed on Figure 5.12 along both source and receiver lines for the far-offset range. The azimuth distribution (Figure 5.13) for far-offsets has a lopsided azimuth distribution stripes (marked B on Figure 5.13) parallel to source and receiver lines but at the 1/2 source and receiver line interval. Fold distribution over this offset range (Figure 5.14) is uniform and averages about 3-6 fold.

In summary, offset distribution is unevenly sampled in the bins for the near and far-offset range but becomes more uniformly sampled for mid-offset range. The azimuth distribution follows the same pattern as the offset distribution with poor azimuth sampling at near and far-offset and more uniform distribution at mid offsets. Fold distribution also has a low fold distribution for the near and far-offset range and high fold distribution for 500-1000 m offset range.

A variation on the original straight-line acquisition model was created and called tight straight-line method. This method used the same survey and receiver patch size but changed the source line and source spacing to 100 m, and the receiver line and receiver spacing to 50 m (Figure 5.15). The purpose of testing this tight straight-line method of acquisition was to evaluate the effectiveness of a more uniform spatial sampling than was achieved using the conventional straight line method of acquisition.

FIG. 5.8 Fold distribution for the near-offset range for the conventional straight-line 3-D acquisition method.
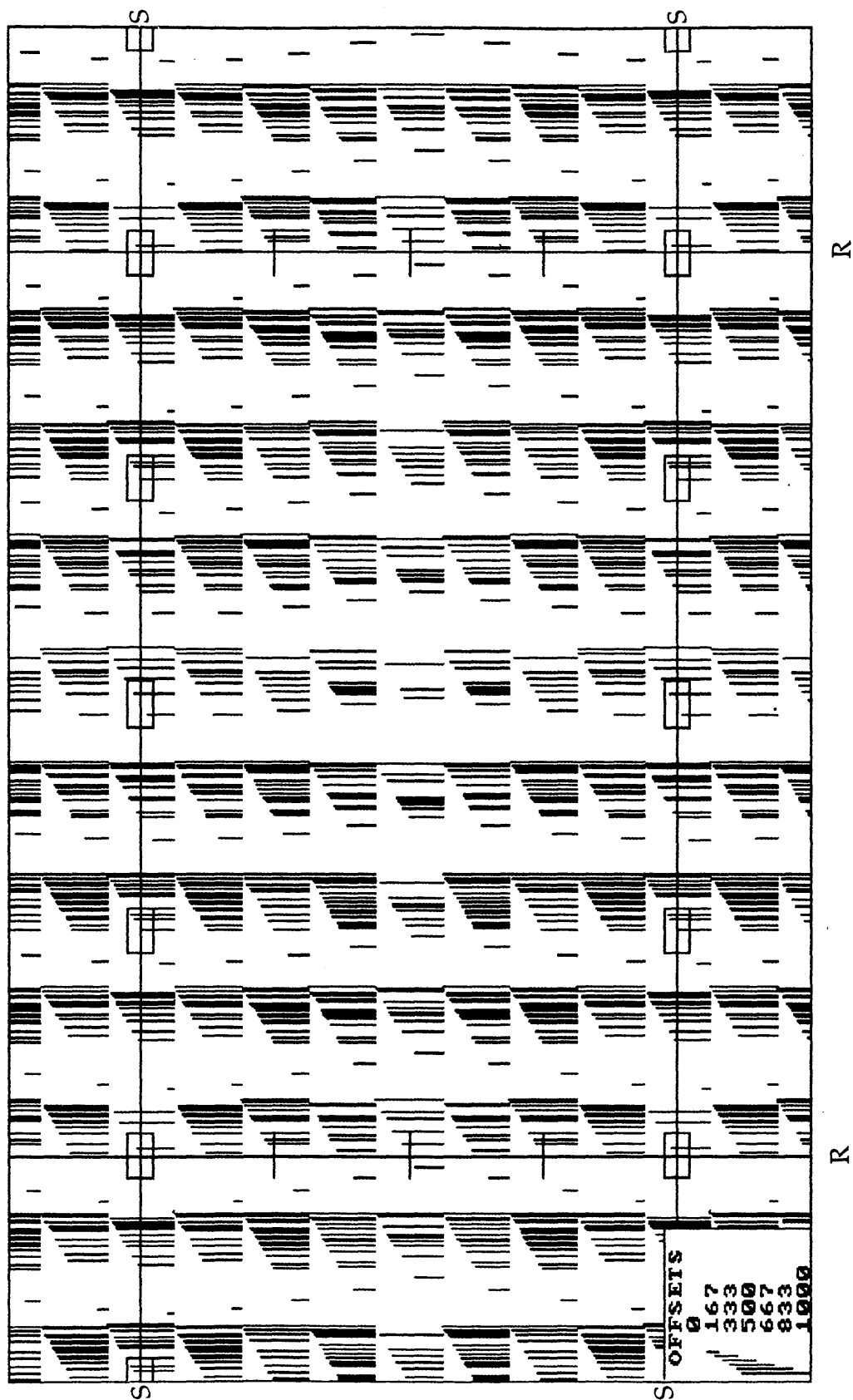
FIG. 5.9 Offset distribution for the mid-offset range for the conventional straight-line 3-D acquisition method.

54
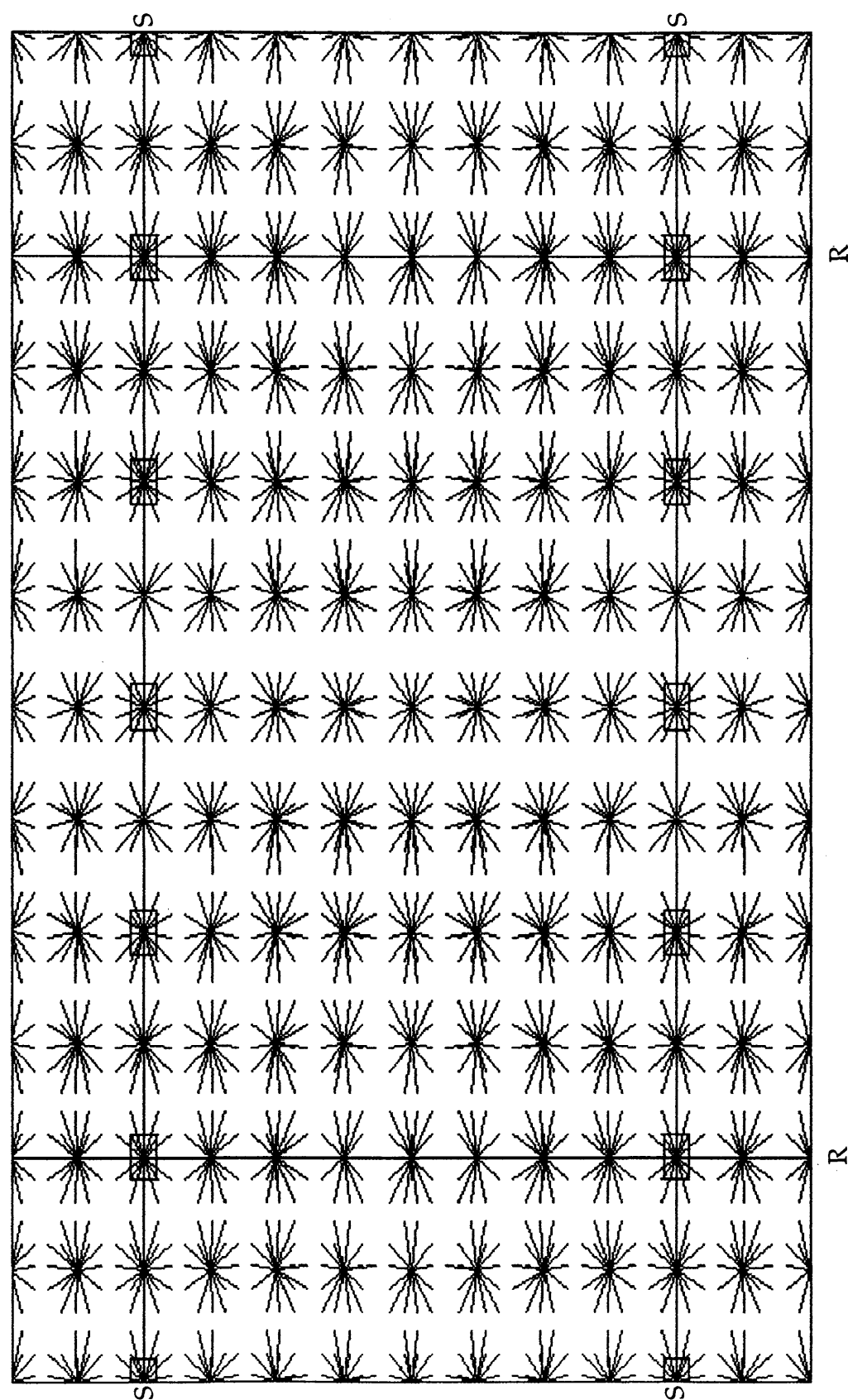
FIG. 5.10 Azimuth distribution for the mid-offset range for the conventional straight-line 3-D acquisition method.
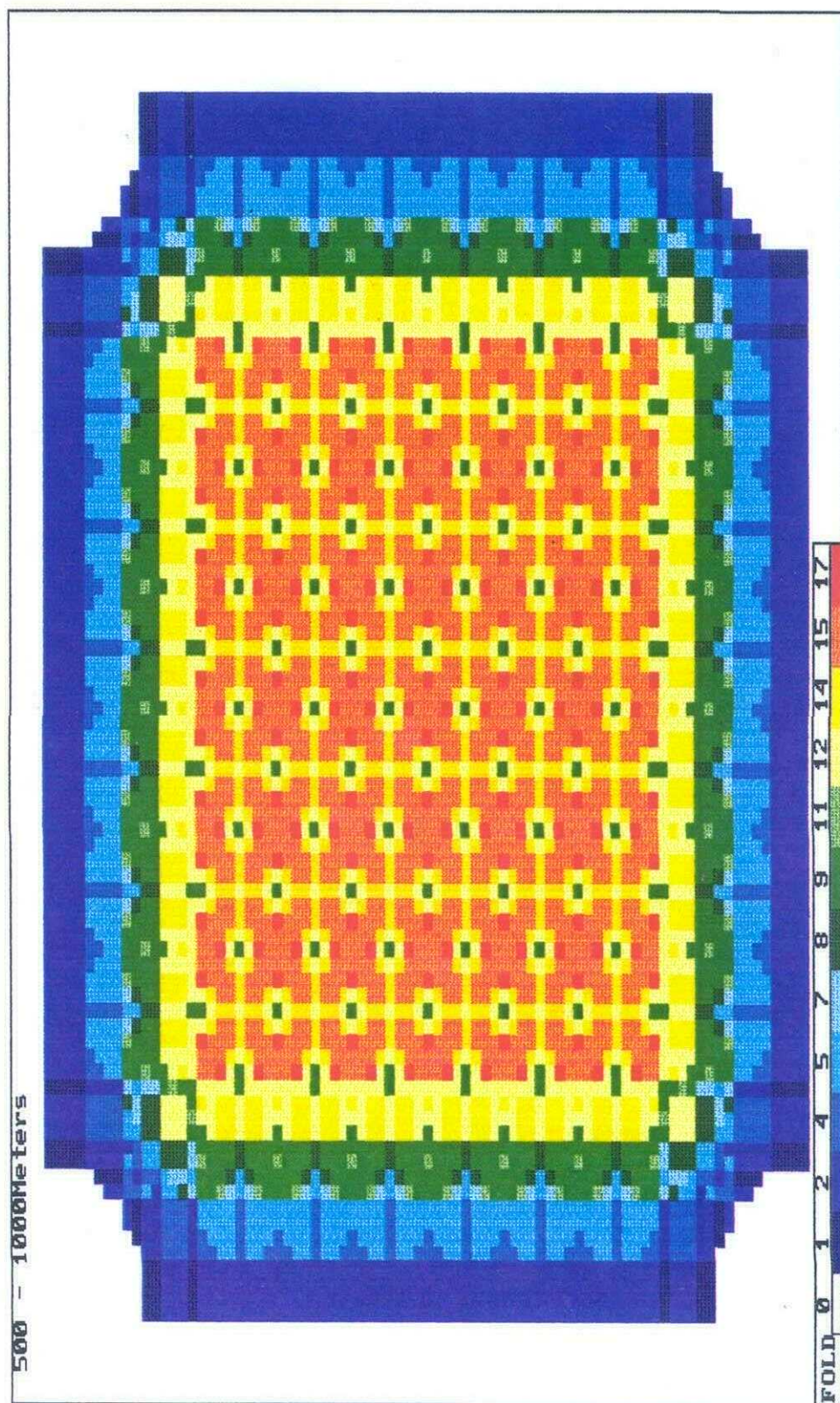
FIG. 5.11 Fold distribution for the mid-offset range for the conventional straight-line 3-D acquisition method.

57
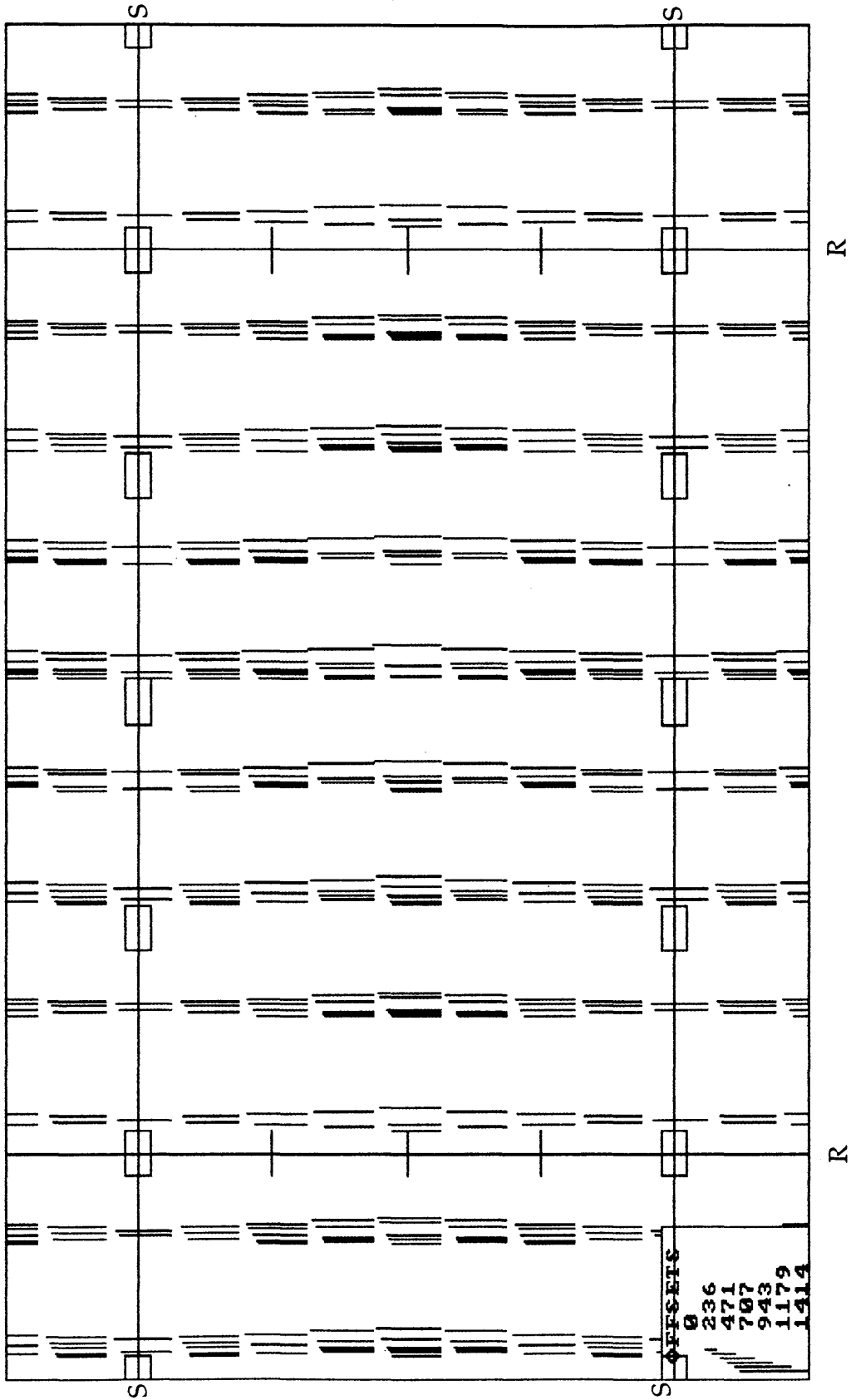
FIG. 5.12 Offset distribution for the far-offset range for the conventional straight-line 3-D acquisition method.

OFFSETS
0
236
471
707
943
1179
1414
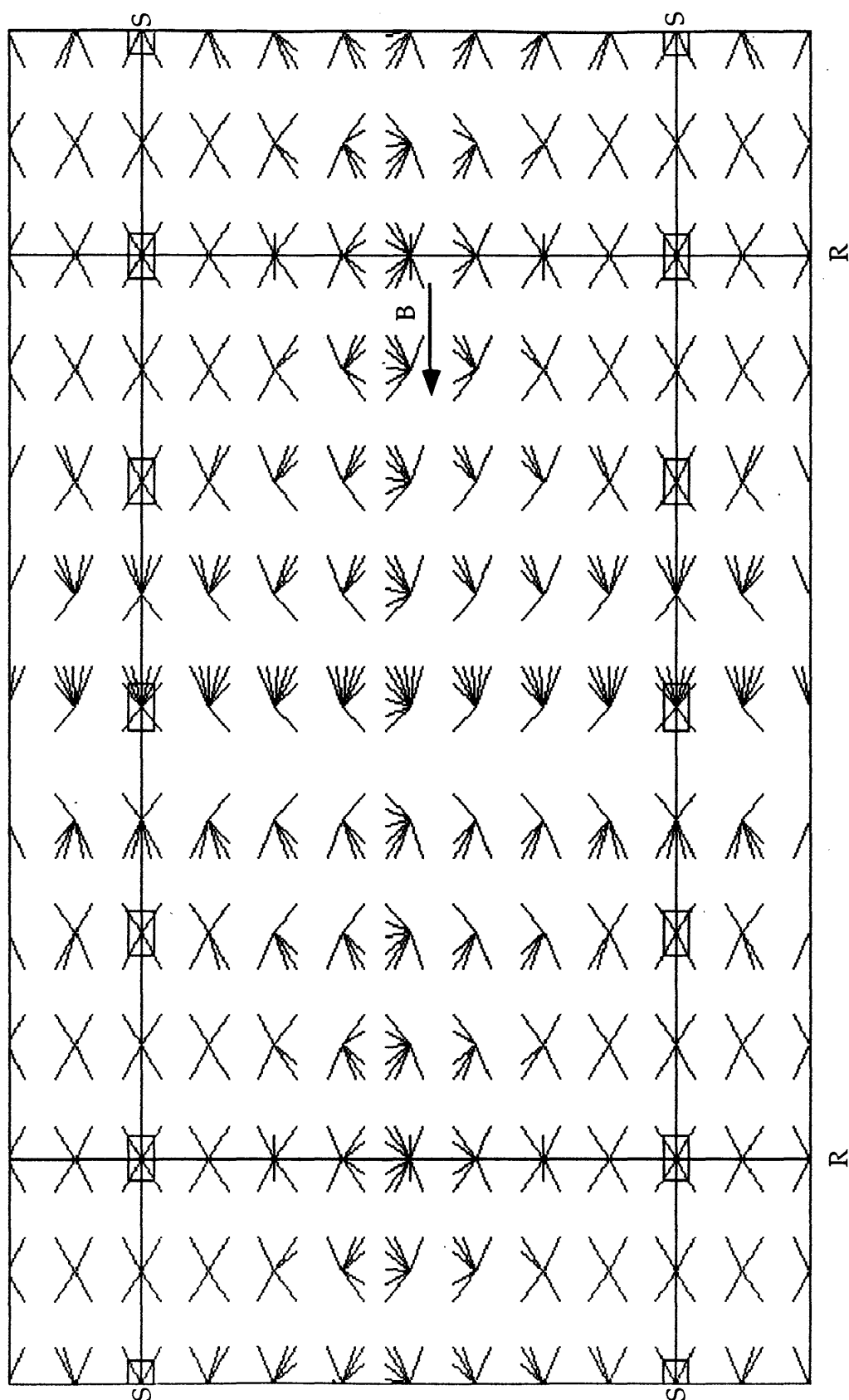
FIG. 5.13 Azimuth distribution for the far-offset range for the conventional straight-line 3-D acquisition method.

FIG. 5.14 Fold distribution for the far-offset range for the conventional straight-line 3-D acquisition method.

XM 0   1:0   0,4
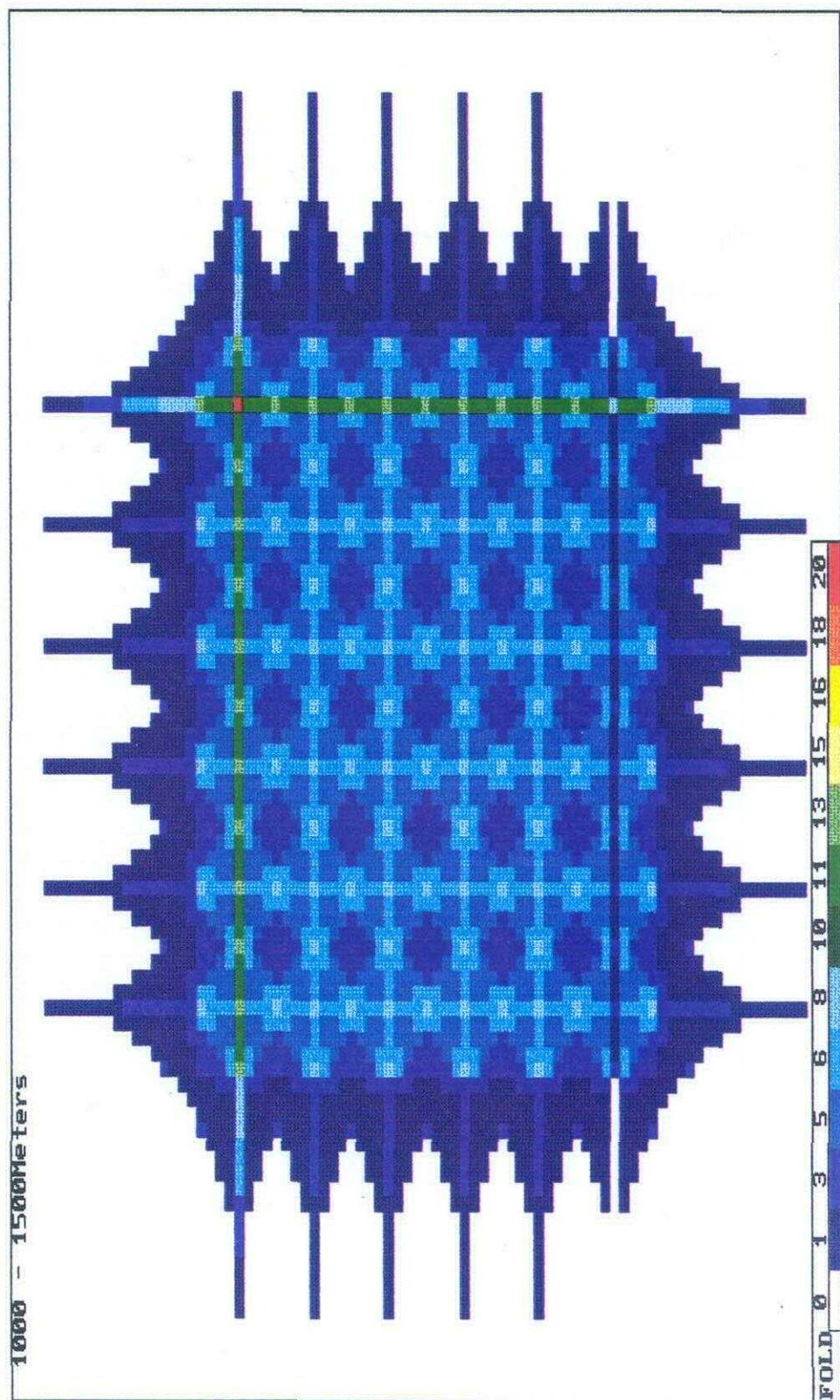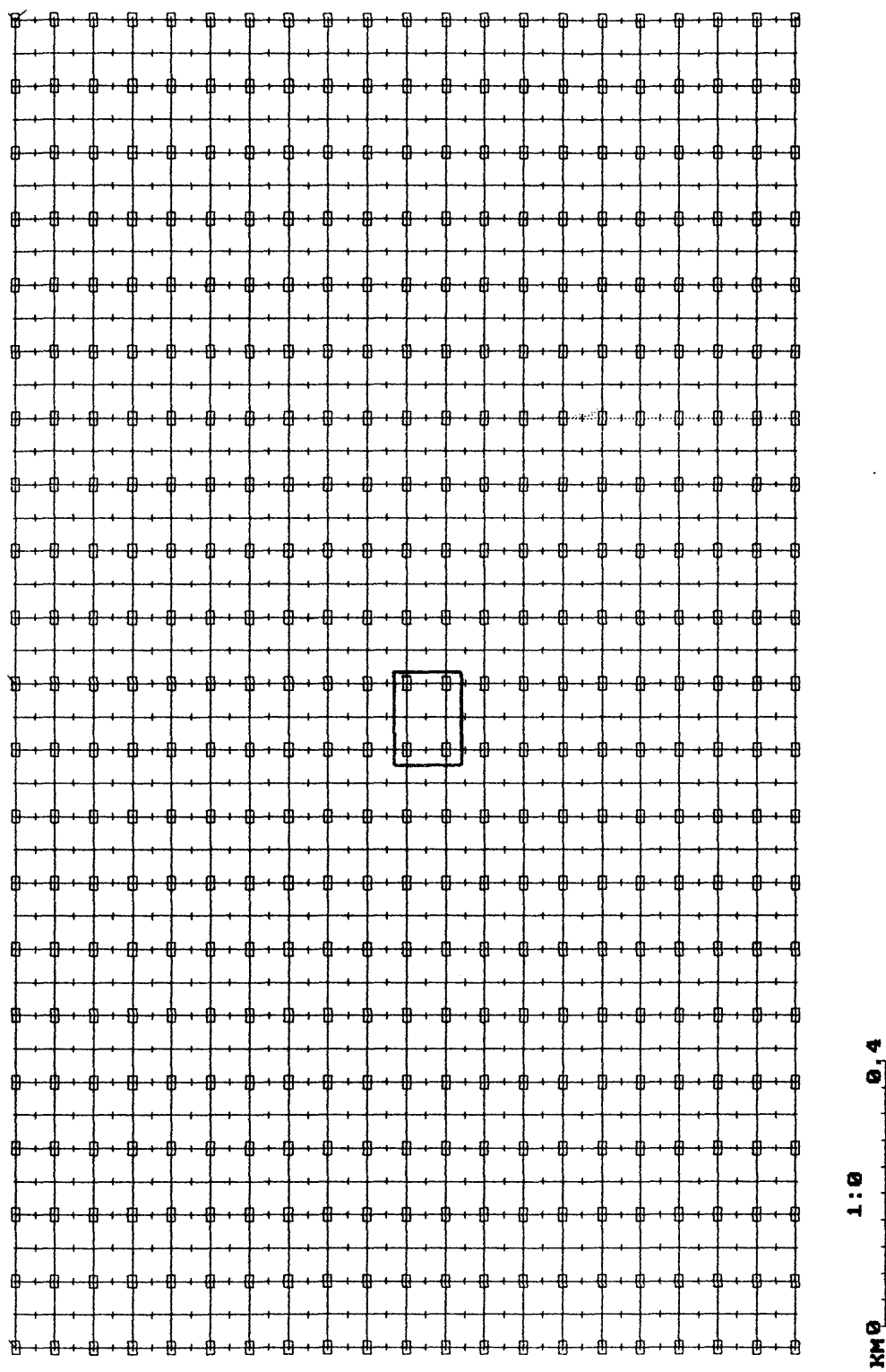
FIG. 5.15 Tight line spacing straight-line method of 3-D acquisition (+ indicate receiver locations, □ = source locations). Small rectangular box is used for offset and azimuth analysis. The bin size is 50 X 25 m.

Figures 5.16, 5.17 and 5.18 illustrate the offset distribution for the near, mid and far-offset ranges respectively and they indicate that the offset distribution is uniform over the whole area and much more consistent than the previous straight-line method over these offset ranges. The largest near-offset on the near-offset range diagram occurs in the bin in the center of any box. This offset is 112 m, which is smaller than 282 m on the straight line method of acquisition discussed previously.

Azimuth distribution for the near and mid-offset ranges, shown in Figures 5.19 and 5.20 respectively, is also uniform over this area and there are many more azimuths in each bin than for the previous straight-line method of acquisition. Figure 5.21 depicts the azimuth distribution for the far-offset range. The azimuth distribution is lopsided along each source line and along every receiver line which intersects a source line.

Fold distribution for the near, mid and far-offset ranges are indicated in Figures 5.22, 5.23 and 5.24 respectively. The fold distribution over this range of offset follows the same pattern as the previous example, with lower fold for the near and far-offset range than the mid-offset range, although fold distribution is closer to being uniform over these ranges than for the previous example. The average fold for the near, mid and far-offset range for this tight straight-line method is; 35-42, 105-115 and 35-43 respectively which is much higher than the conventional straight-line method at each offset range.

In summary, for the tight straight-line method of acquisition, the offset distribution is uniform over all offset ranges and does not suffer from sparse offset sampling that occurs for the near and far-offset range for the conventional straight-line method of acquisition. This uniform offset distribution over all offset ranges will help to determine stacking velocity and provide better coherent
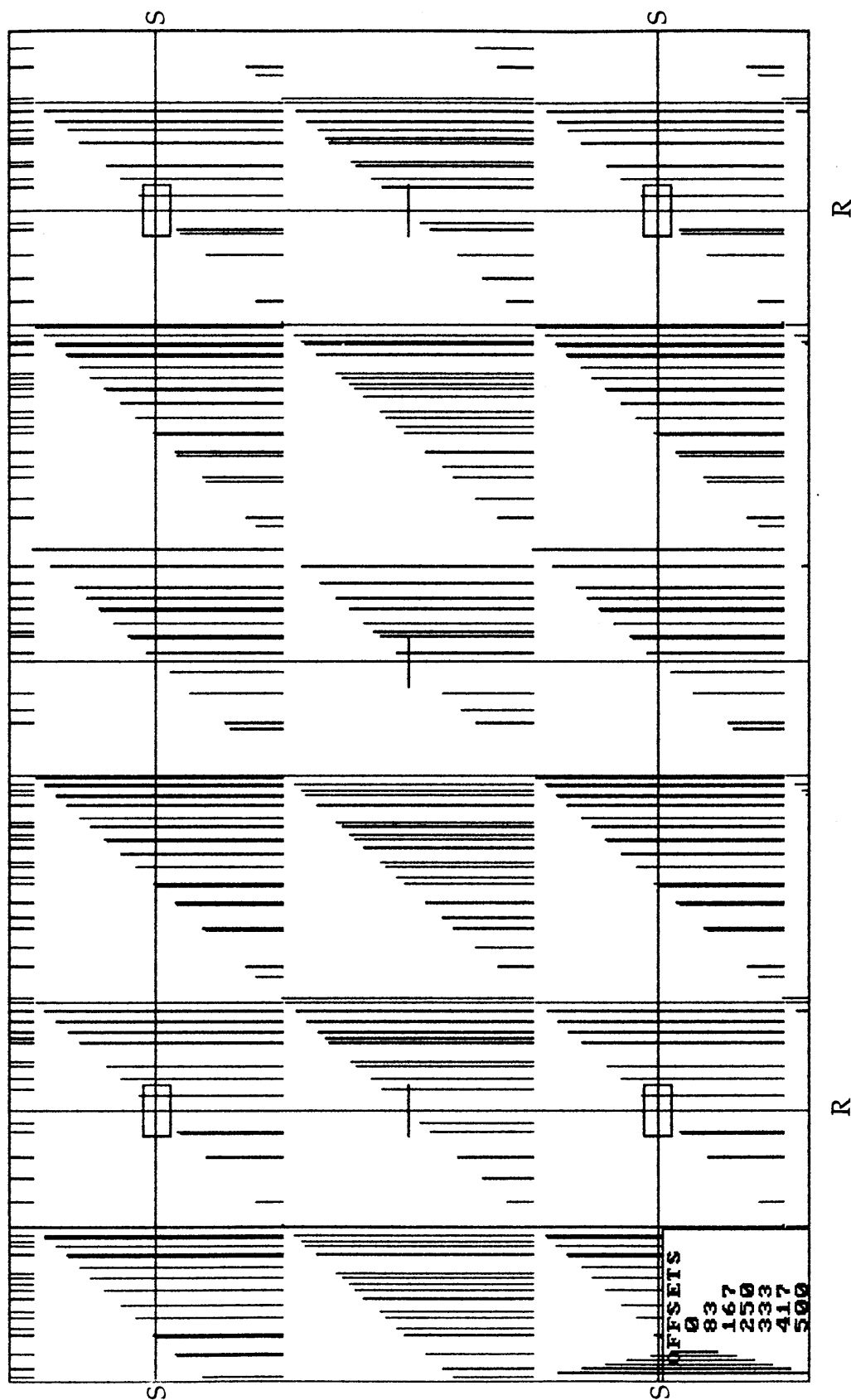
FIG. 5.16 Offset distribution for the near-offset range for the tight line spacing straight-line 3-D acquisition method.

OFFSETS
0
83
167
250
333
417
500
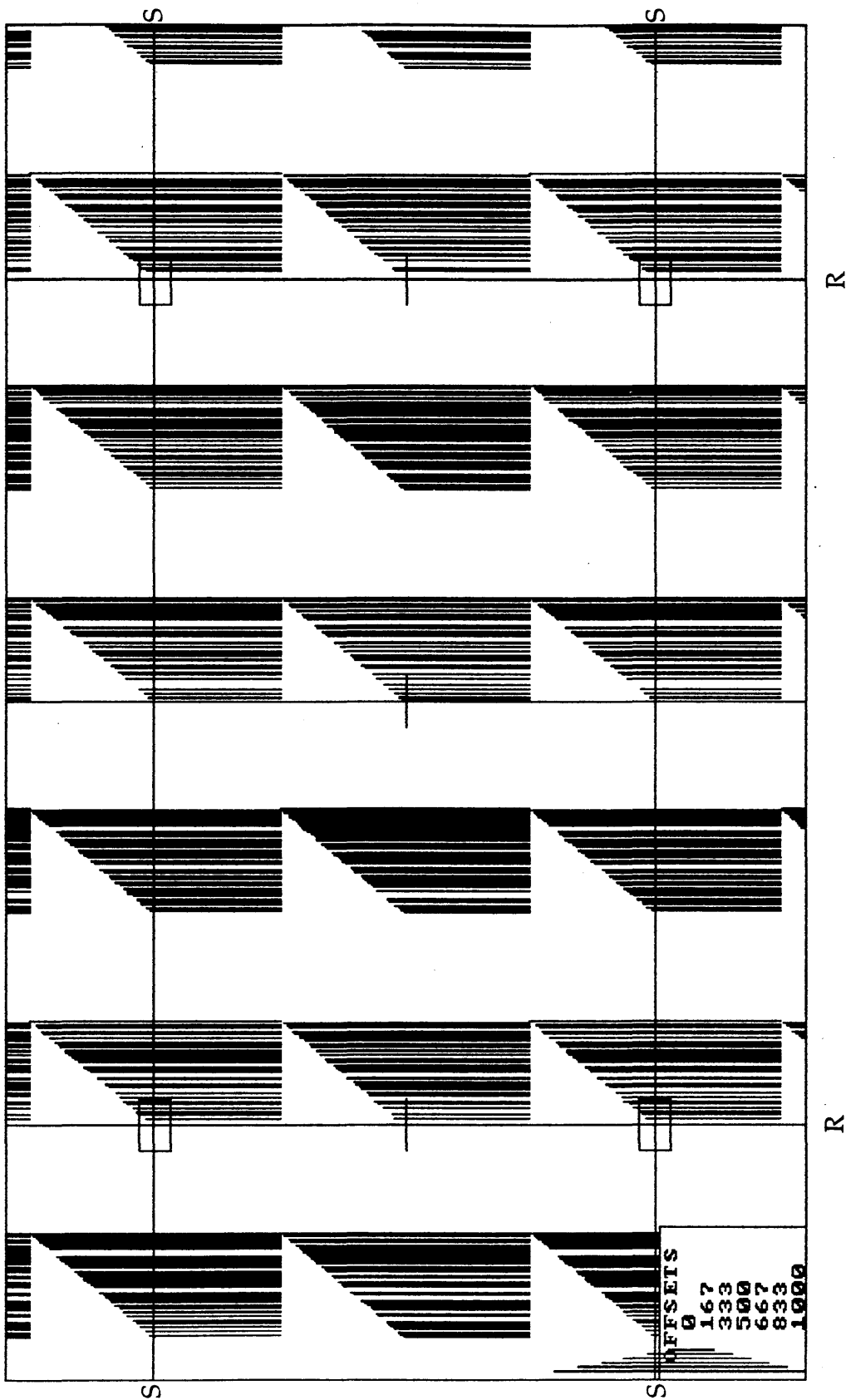
FIG. 5.17 Offset distribution for the mid-offset range for the tight line spacing straight-line 3-D acquisition method.

63
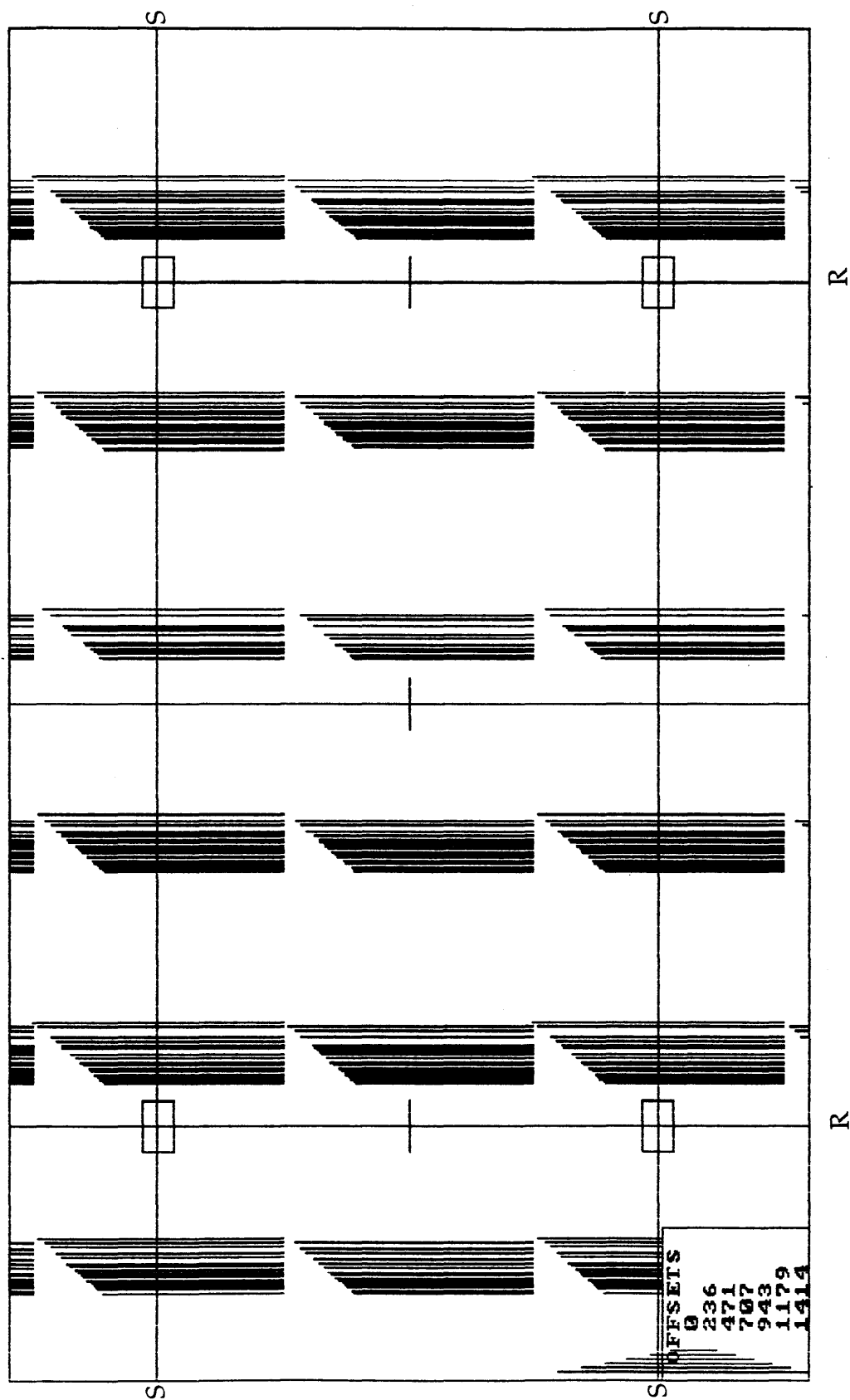
FIG. 5.18 Offset distribution for the far-offset range for the tight line spacing straight-line 3-D acquisition method.
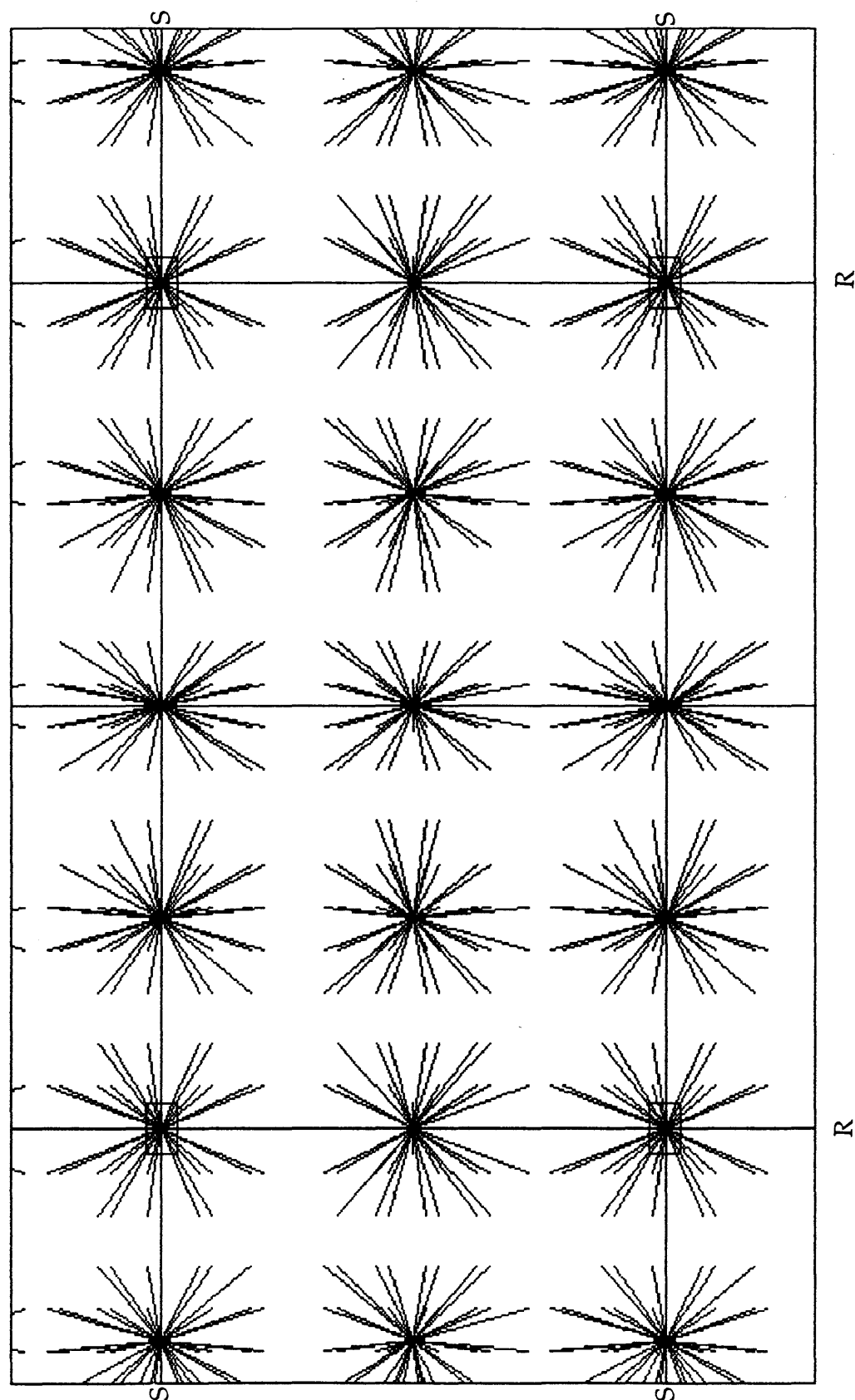
FIG. 5.19 Azimuth distribution for the near-offset range for the tight line spacing straight-line 3-D acquisition method.
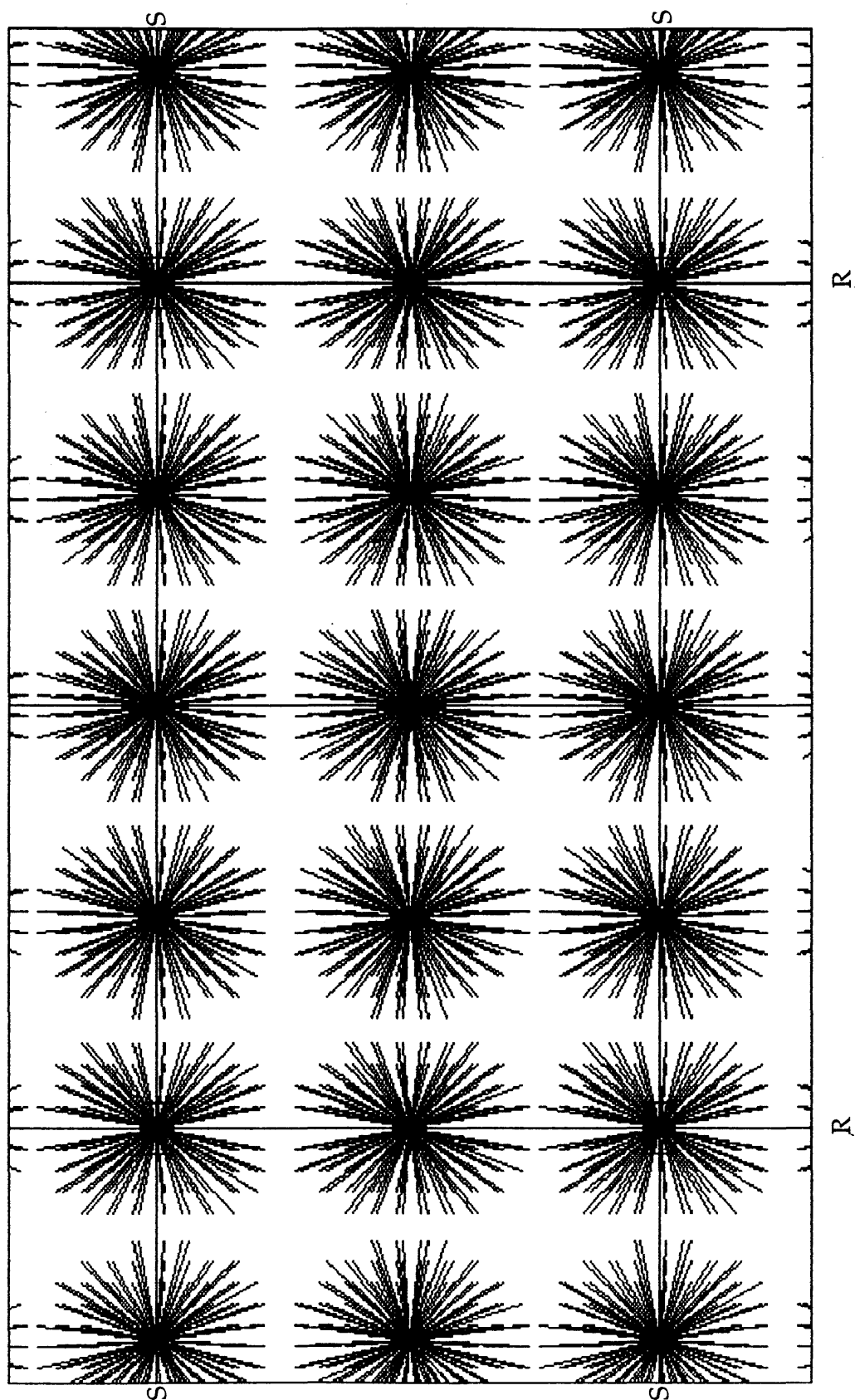
FIG. 5.20 Azimuth distribution for the mid-offset range for the tight line spacing straight-line 3-D acquisition method.
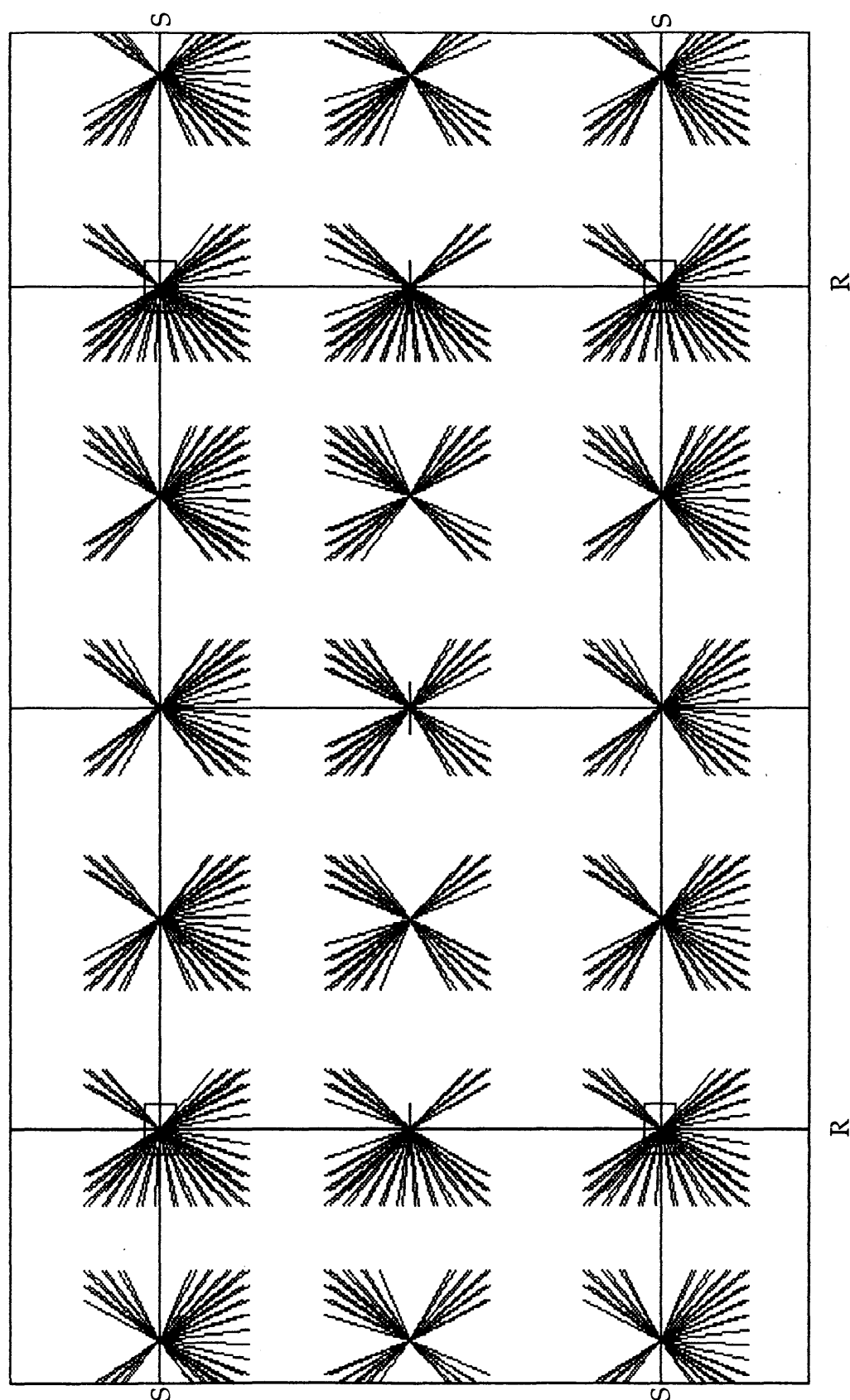
FIG. 5.21 Azimuth distribution for the far-offset range for the tight line spacing straight-line 3-D acquisition method.
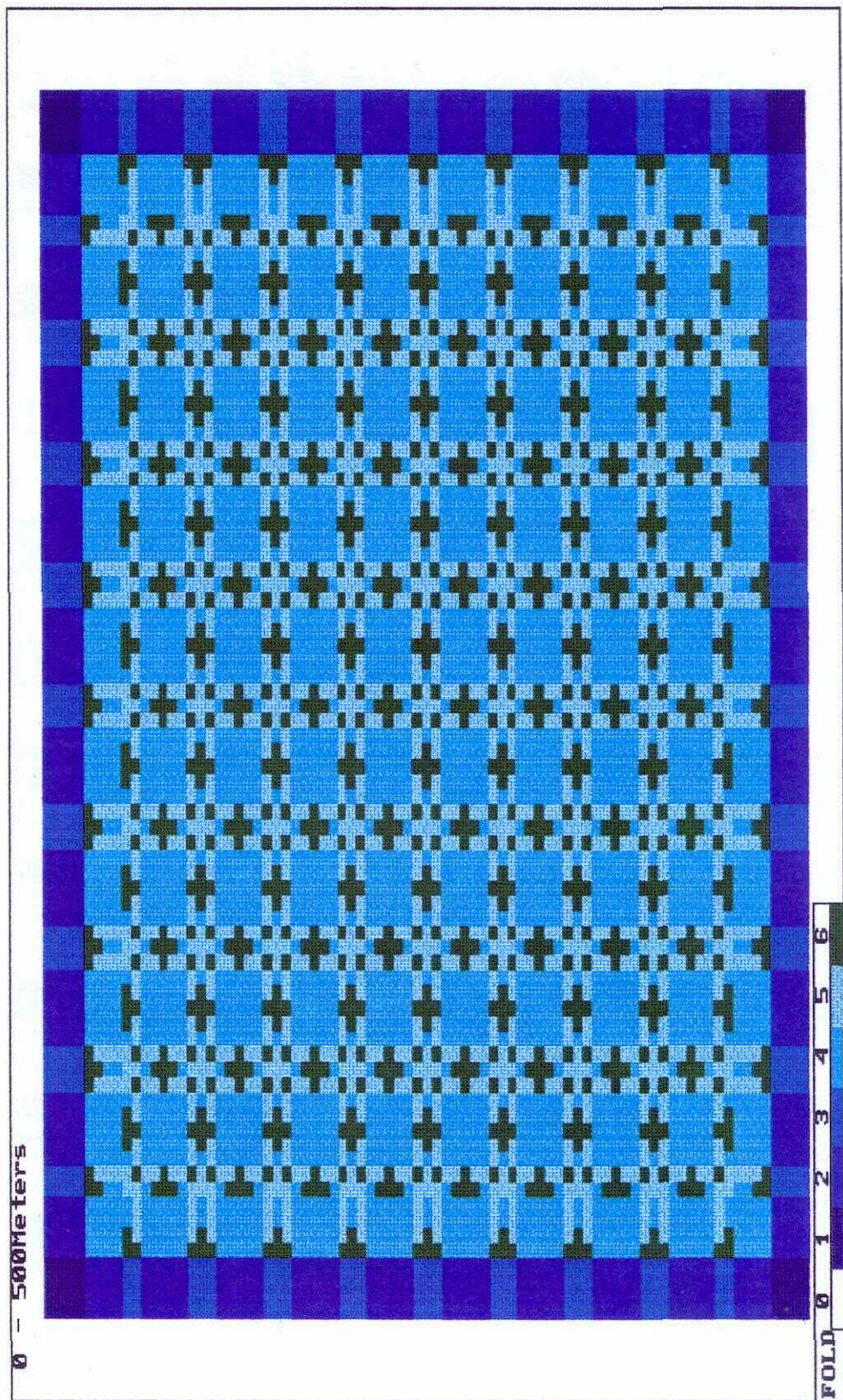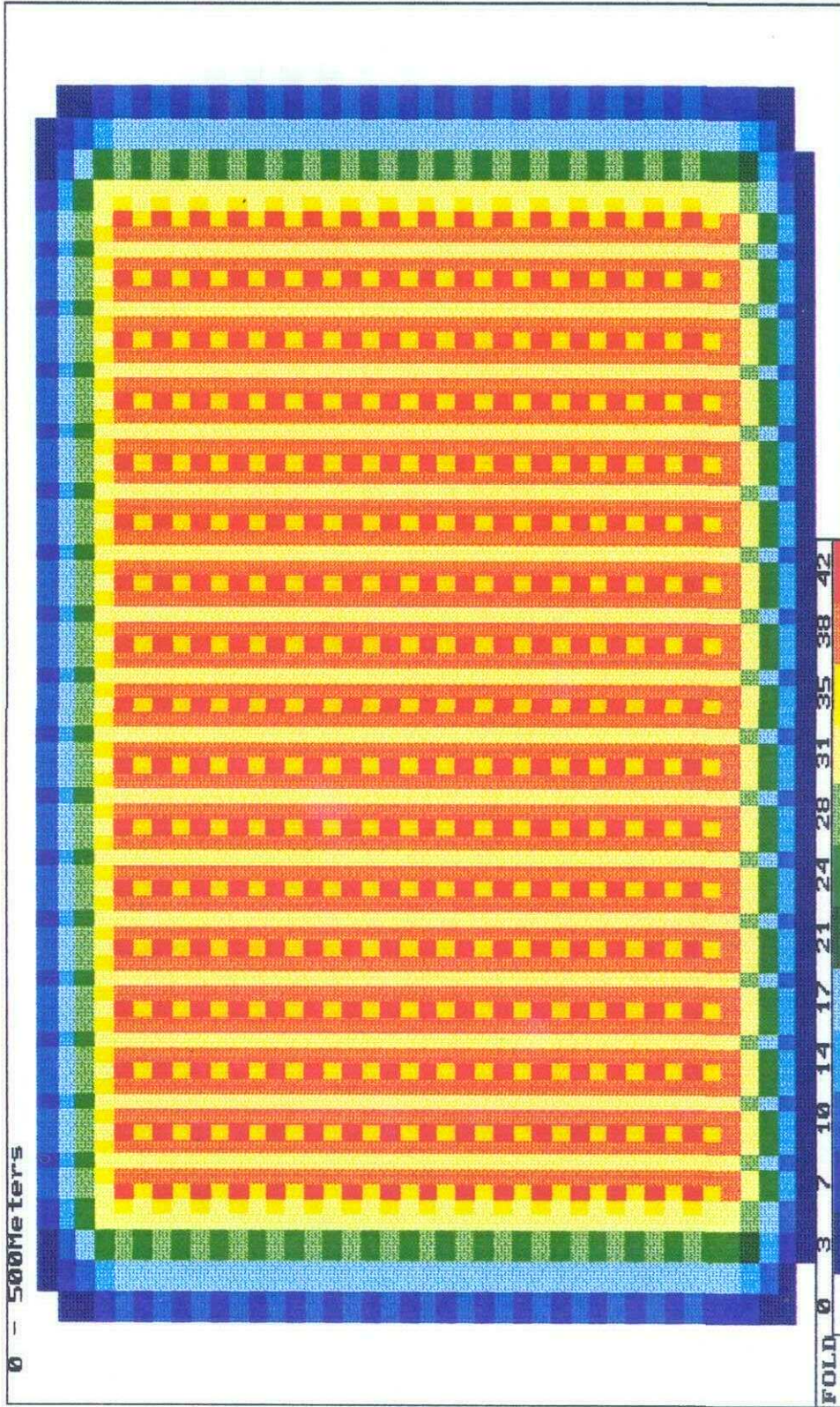
FIG. 5.22 Fold distribution for the near-offset range for the tight line spacing 3-D acquisition method.

69
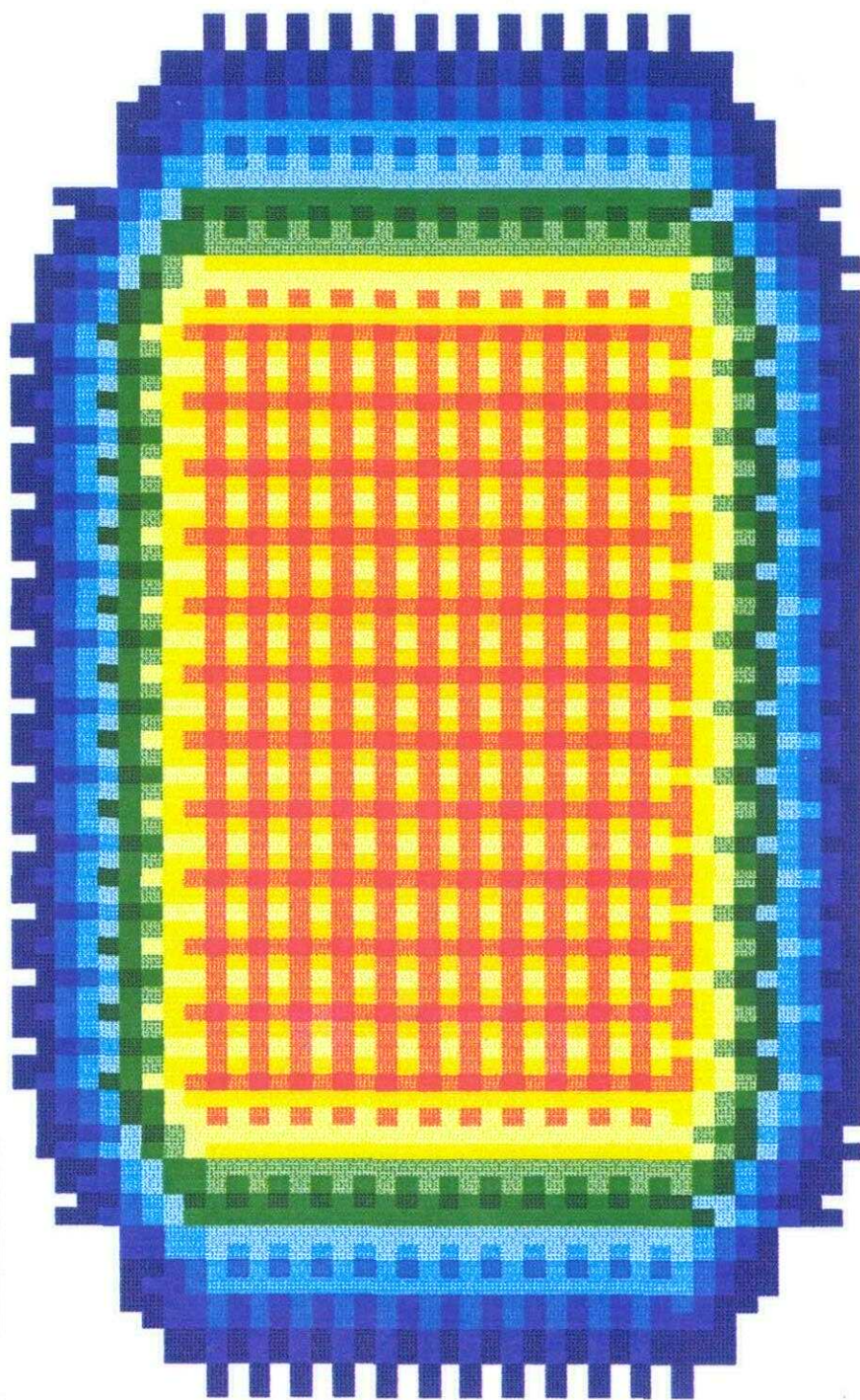
FIG. 5.23 Fold distribution for the mid-offset range for the tight line spacing straight-line 3-D acquisition method.
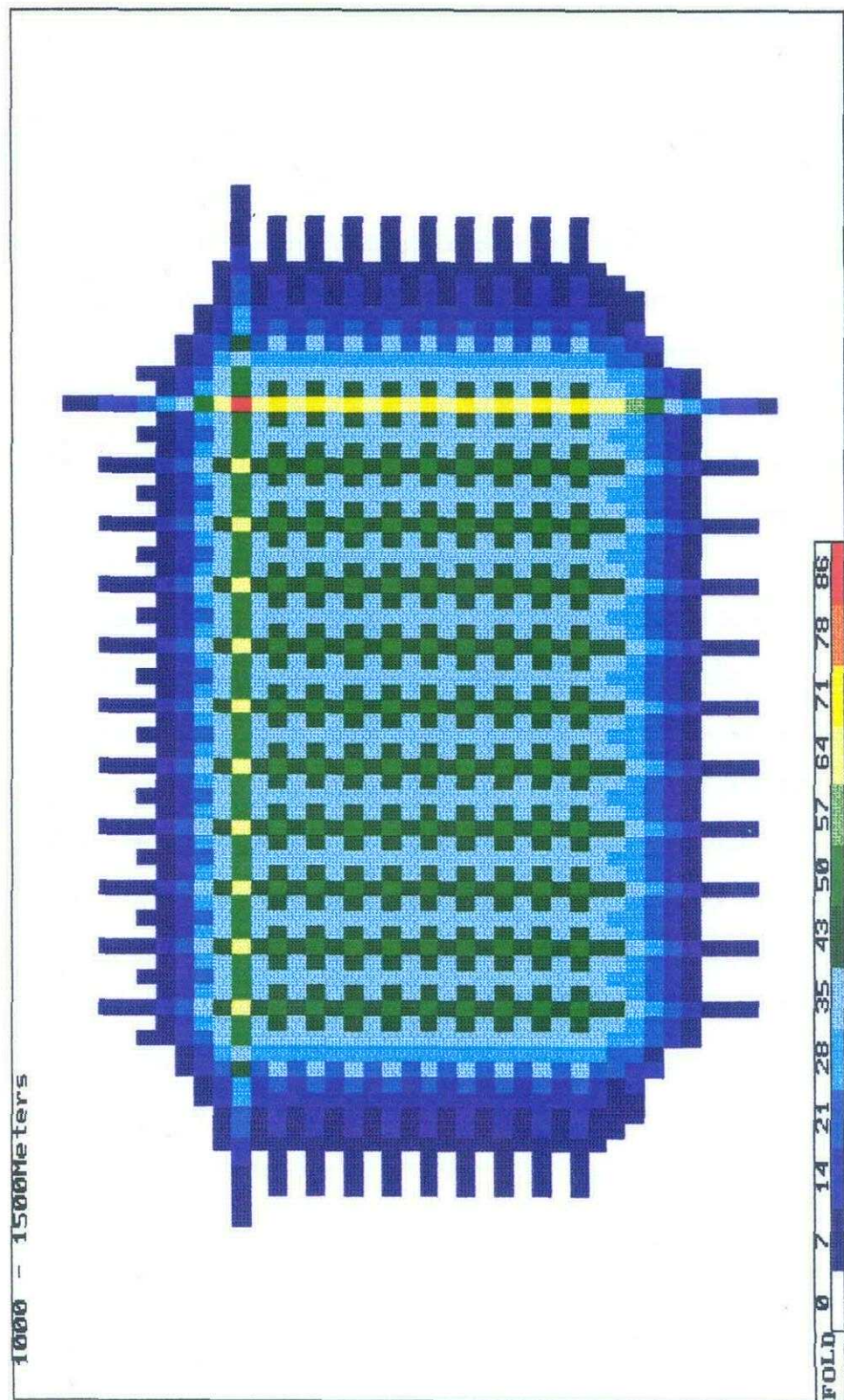
FIG. 5.24 Fold distribution for the far-offset range for the tight line spacing straight-line 3-D acquisition method.

noise cancellation in the stack. The largest near offset of 112 m is much smaller than for the conventional straight-line example which has a maximum near-offset of 282 m. The smaller near-offset range allows better illumination of shallow exploration targets and allows easier shallow velocity determination for refraction analysis. Azimuth distribution is more uniform at all offset ranges than for the conventional straight-line method of acquisition and this will provide a better static coupling between receivers and thus will make it easier to detect azimuth dependent variations such as anisotropy. Fold distribution follows similar pattern with offset range as the conventional straight-line method but fold distribution is more uniform over all offset ranges and this will improve velocity determination for proper NMO correction.

A variation on the straight-line method is the swath acquisition method. In the swath technique, all shots between receiver lines that are several lines apart are fired sequentially, after which the receiver patch is moved several lines and the sequence is repeated. This method provides a field operational advantage over the straight-line survey in that there is a minimum of equipment movement to acquire the seismic data. The disadvantage of this method is that there is poor distribution of offset and azimuth in bins.

The brick acquisition method (Figure 5.25) has an advantage over the straight-line method in that the largest minimum offset in the box is equal to the receiver line interval. The brick pattern allows a wider spacing between receiver lines to obtain the same minimum offset as the straight-line method. A wider receiver line spacing lowers acquisition cost. A second advantage of this method is that it provides reasonable offset and azimuth distribution in the bins. A disadvantage of this method is that surface access must be very open to allow specific placement of sources and receivers.
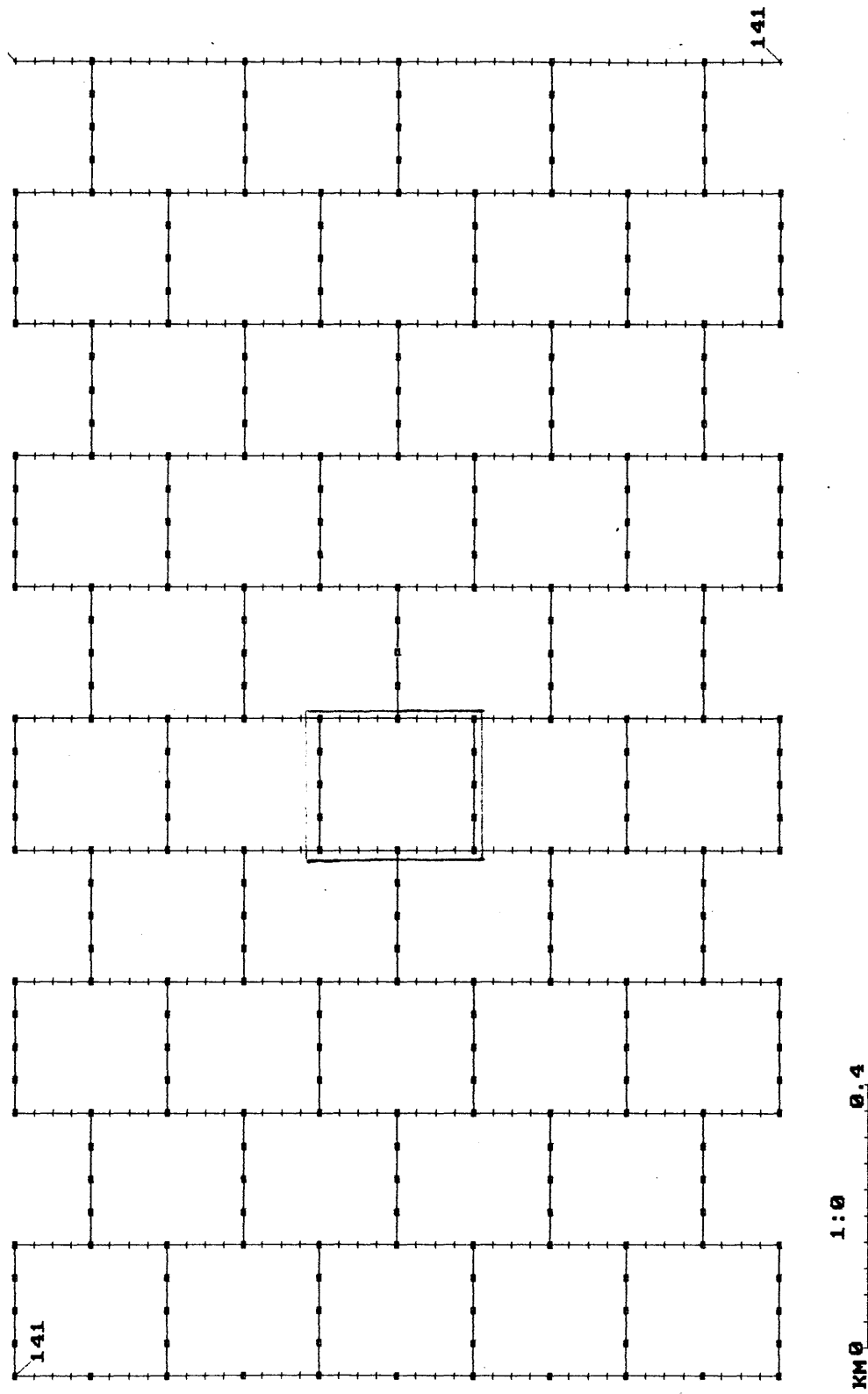
FIG. 5.25 Brick method of 3-D acquisition (+ = receiver locations, ■ = source locations). Small rectangular box is used for offset and azimuth analysis. The bin size is 25 X 25 m.

The offset, azimuth and fold distribution were examined for the brick acquisition method using the same survey size, source and receiver line spacing, source and receiver spacing and receiver patch size as the previous conventional straight-line method. These distributions were only examined over the full-offset range (0-1500m). Figure 5.26 defines the offset distribution for the 0-1500 m offset range. The offset distribution is moderately variable over this area with no pattern to the distribution. The largest near offset in the center bin of the box (A in Figure 5.26) formed by the adjacent source and receiver lines is 200 m. In general, offset distribution is slightly less uniform than the conventional straight-line acquisition method over the full-offset range (Figure A.1). Azimuth distribution for the full-offset range (Figure 5.27) indicates that there is a moderate variation in the azimuth distribution throughout this area. There is a denser azimuth sampling along lines parallel to the receiver lines which are at 1/2 receiver line spacing. This azimuth distribution is slightly less uniform then the conventional straight-line method over the full-offset range (Figure A.2). The fold distribution for the full-offset range (Figure 5.28) averages about 15-19 fold over most of the area which is lower then the 24 fold (Figure A.3) generated by the conventional straight-line method over the full offset range.

In summary offset distribution for the brick method is moderately variable over the full-offset range and is very comparable to the conventional straight-line method of acquisition over the full-offset range. The largest near offset is 200 m which is smaller than for the conventional straight-line 3-D acquisition method. The variation in offset distribution will make it slightly more difficult to determine stacking velocity and have coherent noise cancellation in the stack. Azimuth distribution for the brick method has a moderate variation throughout the survey area for the full-offset range and it is slightly less uniform than the
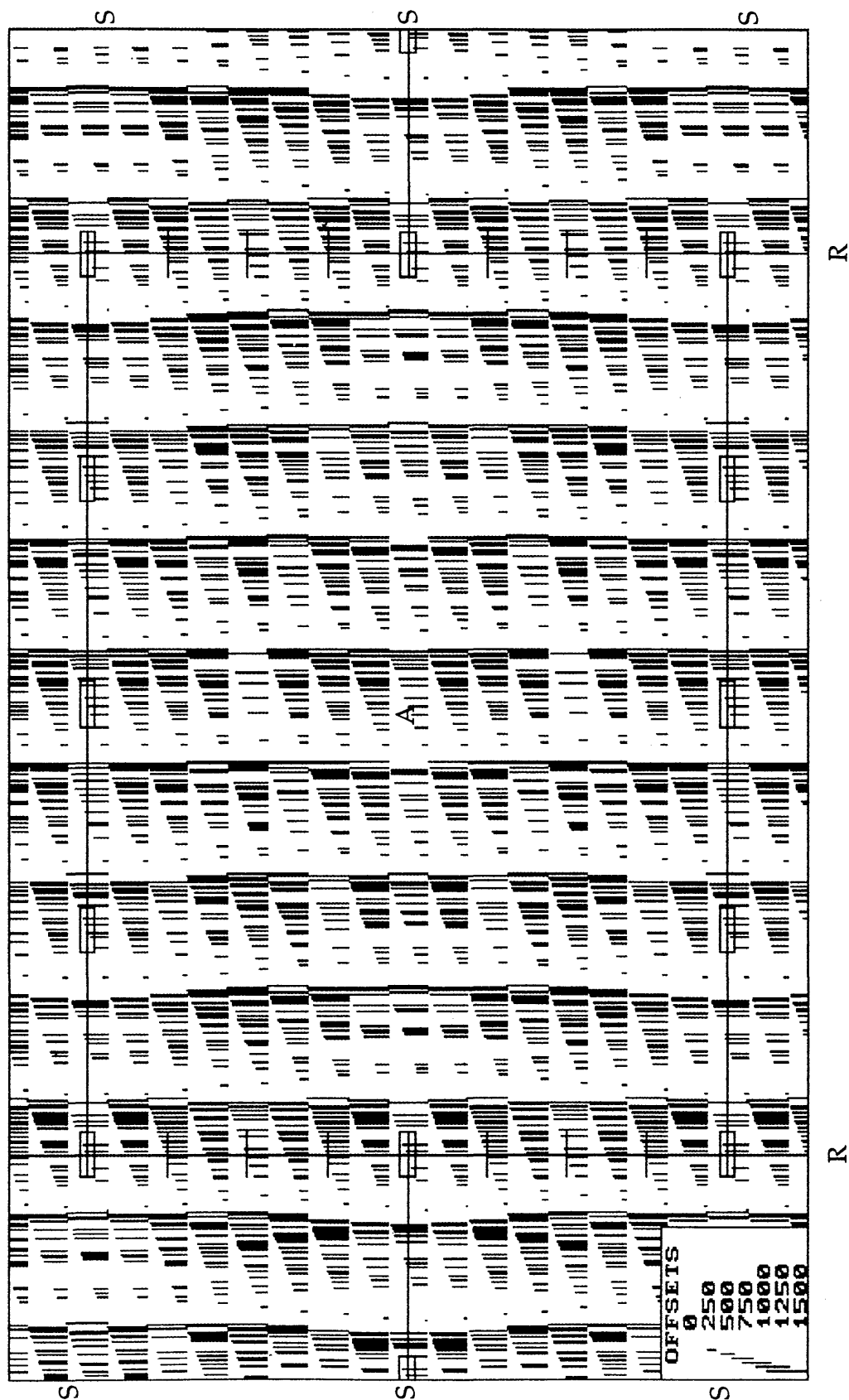
FIG. 5.26 Offset distribution for the full-offset range for the brick 3-D acquisition method.
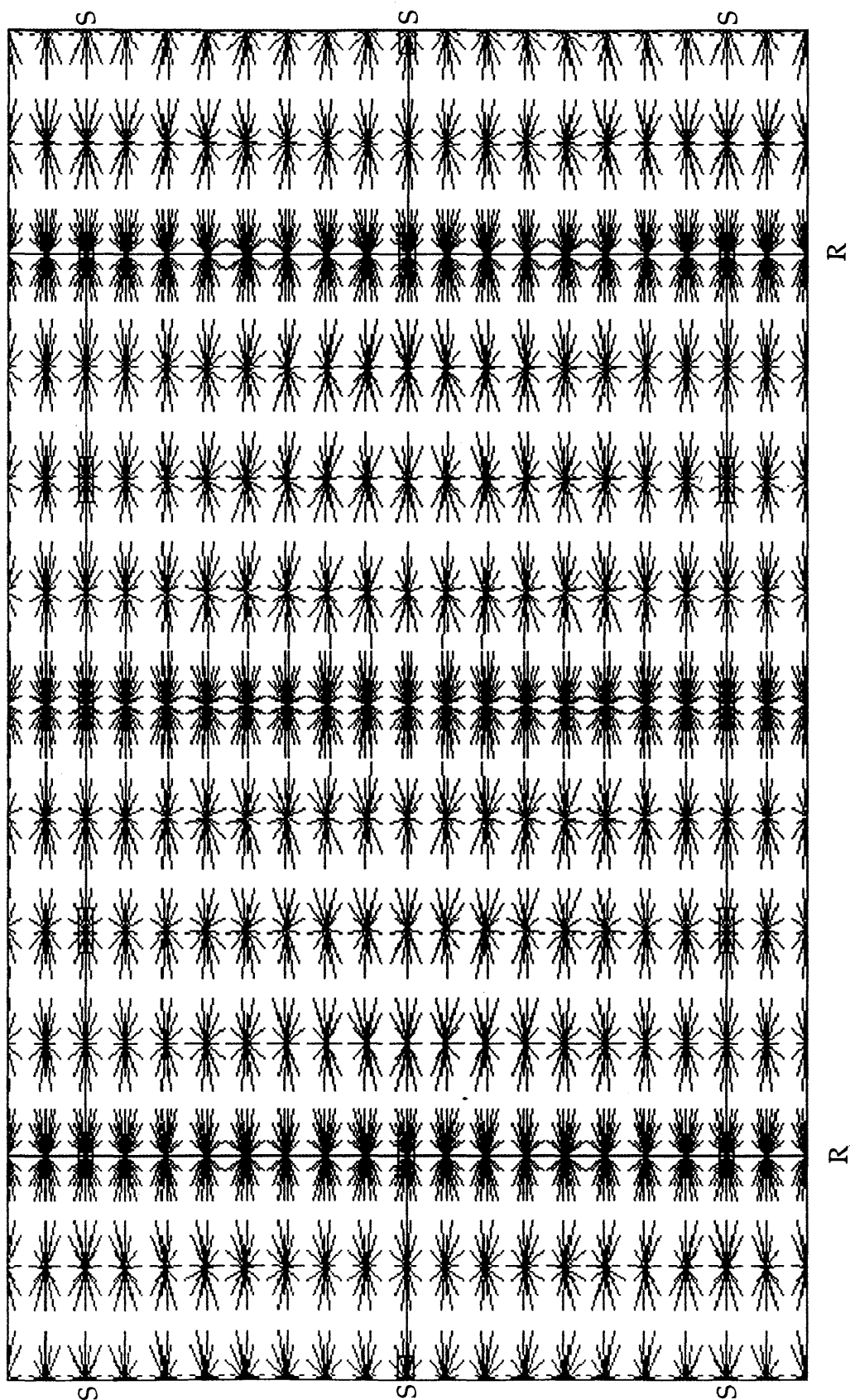
FIG. 5.27 Azimuth distribution for the full-offset range for the brick 3-D acquisition method.
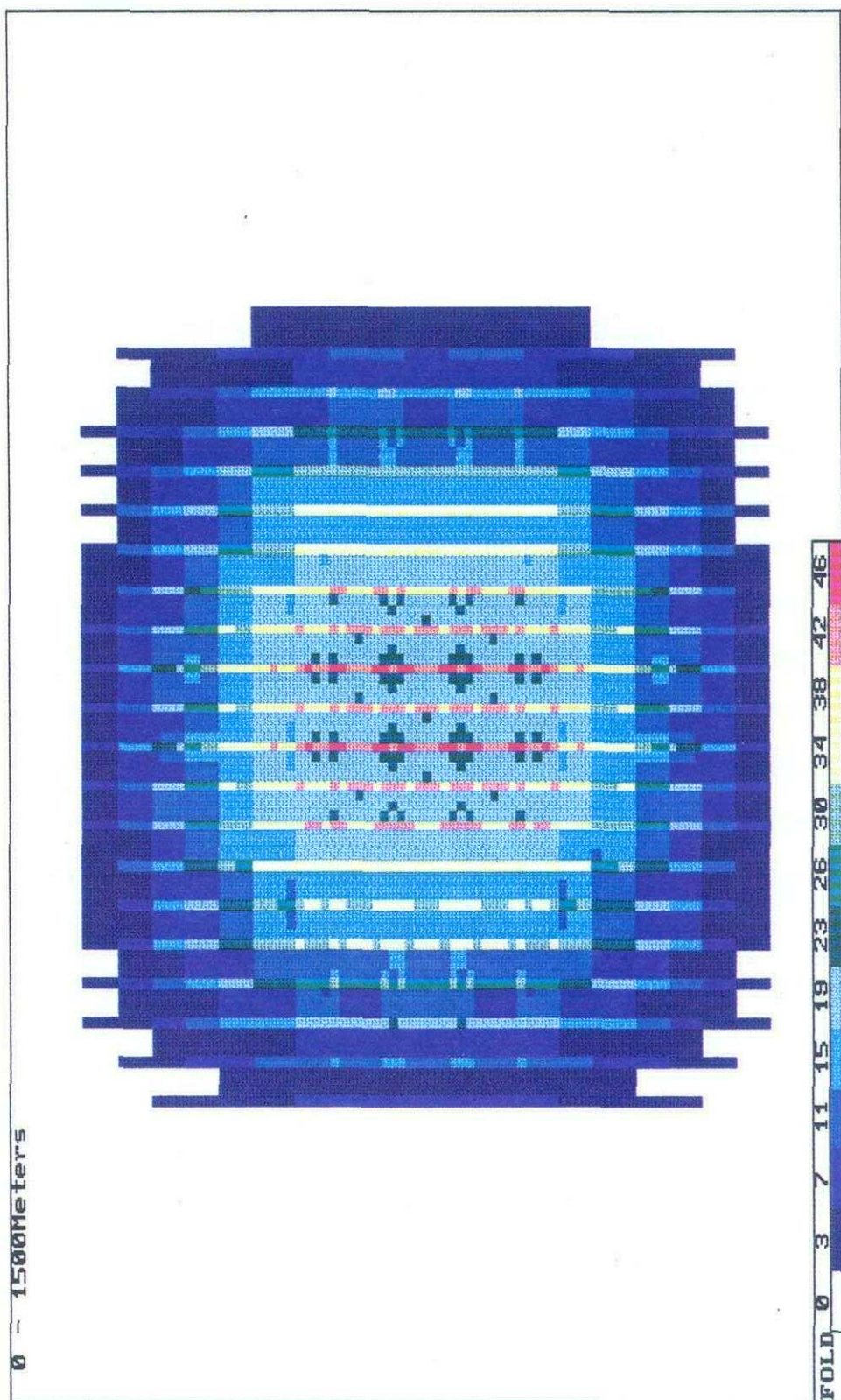
FIG. 5.28 Fold distribution for the full-offset range for the brick 3-D acquisition method.

conventional straight-line 3-D acquisition method over the full-offset range. Fold distribution for the brick method is lower than for the conventional straight-line method over the full-offset range. This lower fold distribution will affect signal to noise ratio and could make it difficult to determine proper velocity for NMO correction.

5.4 3-D Design and Acquisition for the Physical Model

For acquisition of the 3-D survey over the physical model it was decided to use a straight-line acquisition scheme as this provided a simple acquisition geometry which was easy to implement with the physical acquisition apparatus in the physical modeling tank. There are other methods that could have been used to acquire the data such as tight straight-line or brick acquisition method but these all had drawbacks. The tight straight-line method of acquisition would require a significantly longer acquisition time in the physical modeling tank for the same size survey area as the conventional straight-line method because of the higher density of the shots and receivers. The brick method of acquisition has a more variable azimuth distribution and fold distribution is lower for the full offset range compared to the conventional straight-line method.

To determine the proper acquisition parameters for a 3-D straight-line seismic survey over the physical model, both Seismic Image Software's FDTOOLS and FD33 software was used. The FDTOOLS software provides raytracing of a user input model to determine the source-receiver offset that is required to image the zone of interest on the user input model. This software was used to determine the source-receiver offset which is required to image a geological model consisting of a 600 m wide channel at a depth of 1000 m. The model which was input into FDTOOLS had P-wave formation velocities similar to the study area. It was found from this program that a offset range of at least

1000 m was required to image the 600 m wide channel. The minimum offset to obtain a reflection from the channel was 0 m. It was decided to use a 25 x 25 m bin size in the 3-D survey because this would provide a minimum of 12 bins over the 320 m wide point bar in the model. The bin size was fixed at 25 x 25 m and the source receiver offset was set at a minimum of 1000 m for maximum offset and minimum offset should be as small as physically possible.

Various shooting strategies were tested using the FD33 software to determine a reasonable fold coverage, azimuth and offset distribution for the 3-D seismic survey. A rectangular patch was used in all the shooting strategies by defining the number of receiver lines and the number of receivers to be live for each shot in the 3-D survey. The shooting pattern for each strategy was such that the first source line was shot sequentially, then the second source line was shot in reverse order to the first source line, as indicated in Figure 5.29. This pattern of alternating shooting direction on each source line is used for the rest of the source lines in the survey. For the geometry of this survey, four shots were acquired into each receiver patch before the receiver patch was moved. Thereafter, the receiver patch was moved by one receiver line after each four shots. This pattern was repeated until the receiver patch contained the maximum number of receiver lines that the user had defined for each receiver patch. In Figure 5.29, the "A" group of 4 shots fire into half of the receiver patch in both the X and Y directions but when the "B" group of 4 shots were acquired, the active receiver patch was still half the maximum patch size in the Y direction but has expanded by 2 receiver lines to the maximum receiver patch size in the X direction. After the "B" group of 4 shots were acquired on Figure 5.29 then the whole receiver patch will shift by one receiver line after each four shots were fired into a receiver patch. This pattern continues until the receiver patch
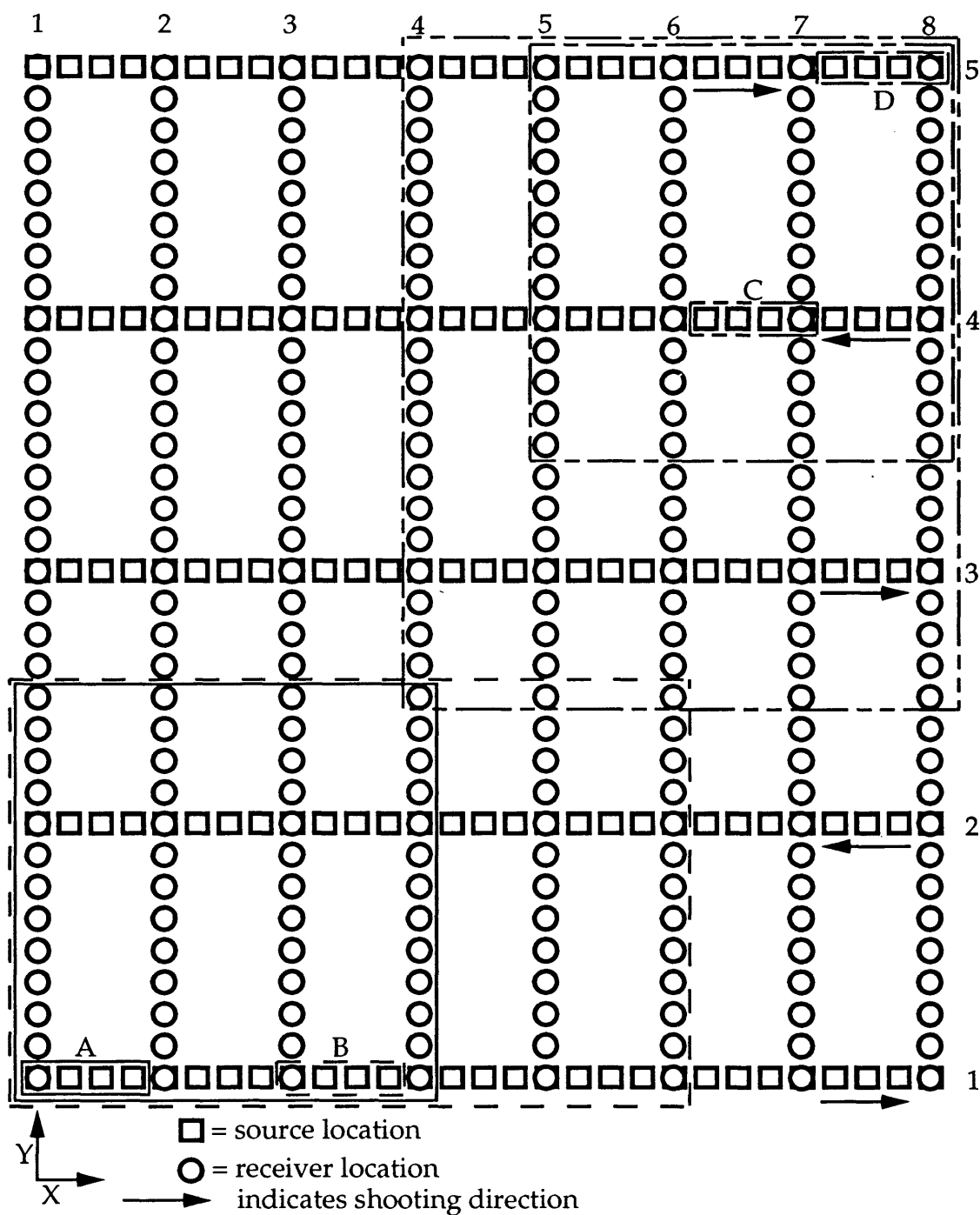
FIG. 5.29 Schematic diagram showing acquisition geometry used to model and acquire 3-D offset surveys. Source groups A and B respectively show receiver patch rolling-in the X direction to the full receiver patch in the X direction. Source groups C and D respectively show receiver patch rolling-out in both the X and Y directions to the half receiver patch in both the X and Y directions. The receiver patch for this shooting geometry is 6 receiver lines by 24 receivers per line.

reaches the edge of the survey where roll-out begins. This is indicated on Figure 5.29, as the receiver patch rolls out in both the X and Y directions between the acquisition of the "C" group of 4 shots and the "D" group of 4 shots. This continues until all the shots on each source line have been fired. The receiver patch is set up such that the first shot fired into a receiver patch is always in the center of the receiver patch.

The shooting strategy designed to acquire the tank data consisted of a 4000 x 4000 m straight-line survey with a 200 m receiver line spacing, 400 m source line spacing, and a 50 m source and receiver station spacing with a receiver patch of 48 receivers per line and 10 receiver lines for a patch size of 2400 by 2000 m. The subsurface fold coverage was calculated for this strategy using an offset range of 0-1500 m (Figure 5.30). There is a consistent fold coverage of 15 fold throughout the center of the survey. The offset distribution was also calculated for this strategy and it indicates the maximum offset for this strategy is 1562 m and the offset distribution is well distributed in each of the bins. Figure 5.31 shows the offset distribution in some of the bins in the center of the survey. The maximum near offset in any bin in the survey is found in the center bin of any box and this maximum offset is 447 m. The azimuth distribution was also calculated and Figure 5.32 shows the azimuth distribution in some of the bins in the center of the survey. The star shaped azimuth distribution in each bin indicates that there is a full 360 degree range of azimuths in the bins in the center of the survey area.

This strategy meets all the requirements for the 3-D survey but there is a problem in that there are too many traces in the survey so that the acquisition time for this survey would be significant. This survey was modified by decreasing the number of source lines and receiver lines in the survey while

81
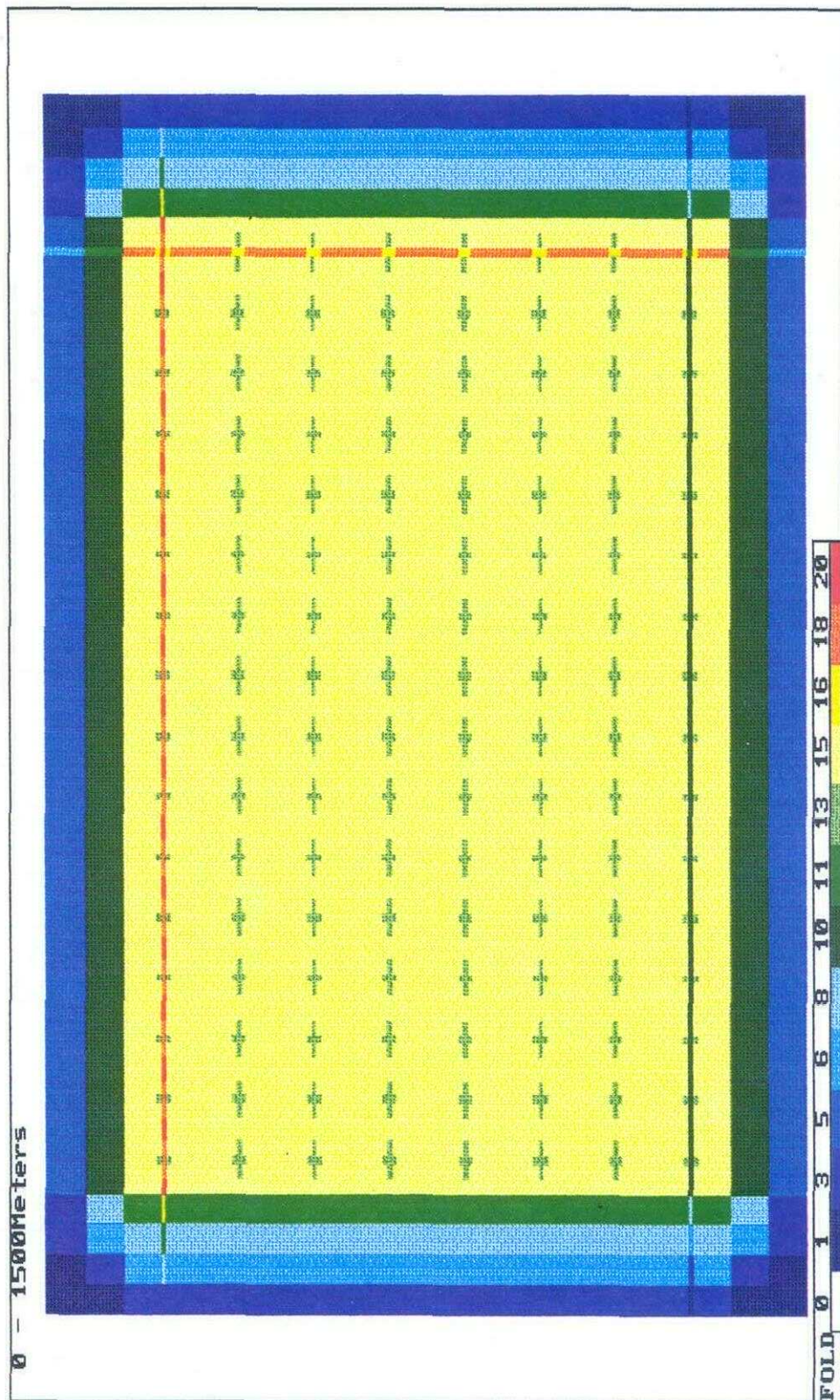
FIG. 5.30 Fold distribution for 0-1500 m offset range.

FIG. 5.31 Offset distribution for 0-1500 m offset range.
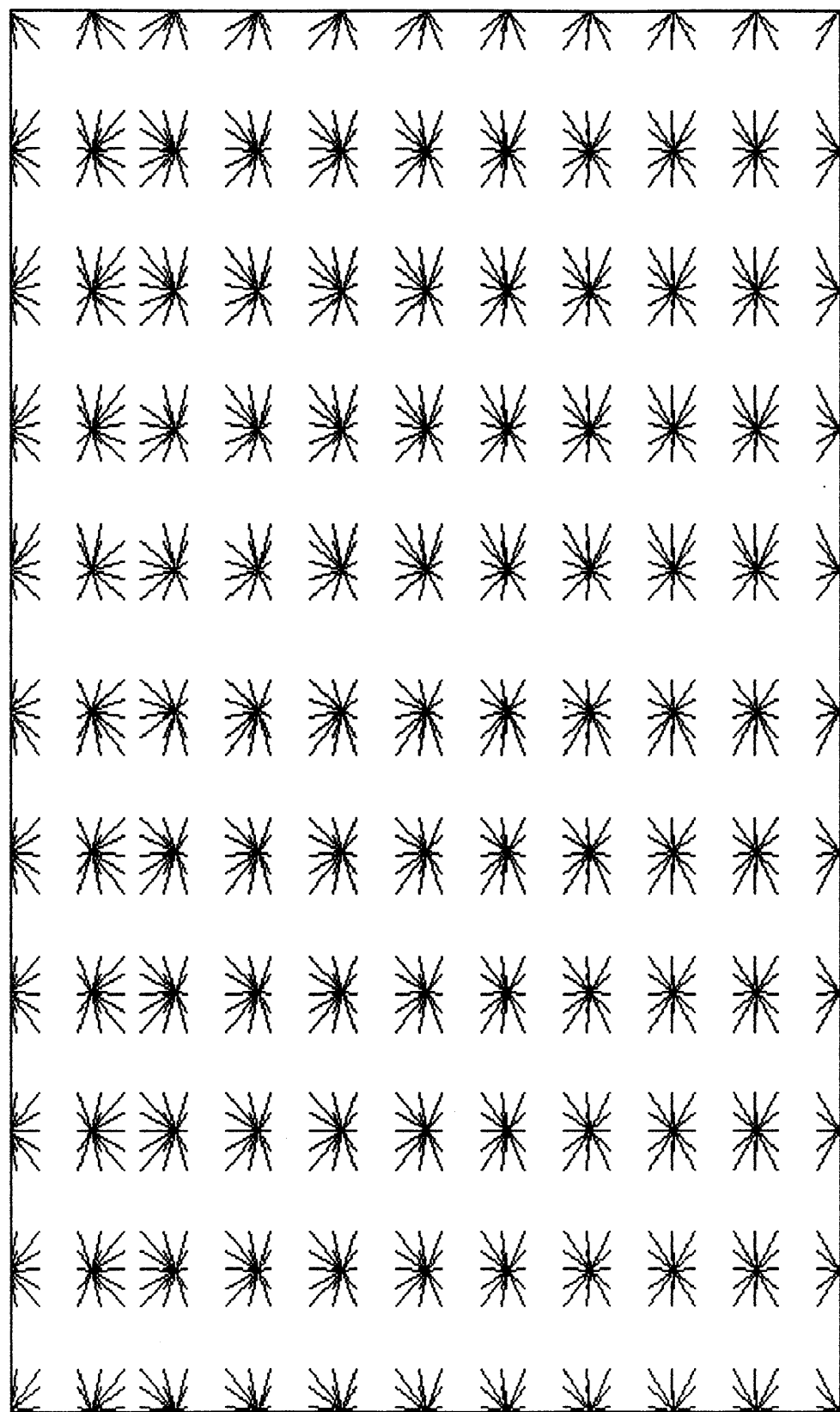
FIG. 5.32 Azimuth distribution for 0-1500 m offset range .

maintaining the same receiver patch of 10 receiver lines and 48 receivers per line. The survey size was reduced so there were only 7 source lines and 10 receiver lines in the survey. The survey was further modified by deleting source points at each end of the source lines and deleting receivers which lay beyond the edge of the grid produced by the source lines (Figure 5.33). These modifications to the survey reduced the number of traces recorded in the survey and reduced the center of the subsurface fold coverage to 14 and reduced the area of 14 fold to a rectangle of 1100 m E-W by 1600 m N-S. The full fold coverage zone for this strategy is sufficiently large that the 3-D seismic survey shot in the modeling tank will have full constant fold over the channel surrounding the point bar including the channel splay and approximately half the lateral bar.

□ = source location
O = receiver location

392 m

196 m
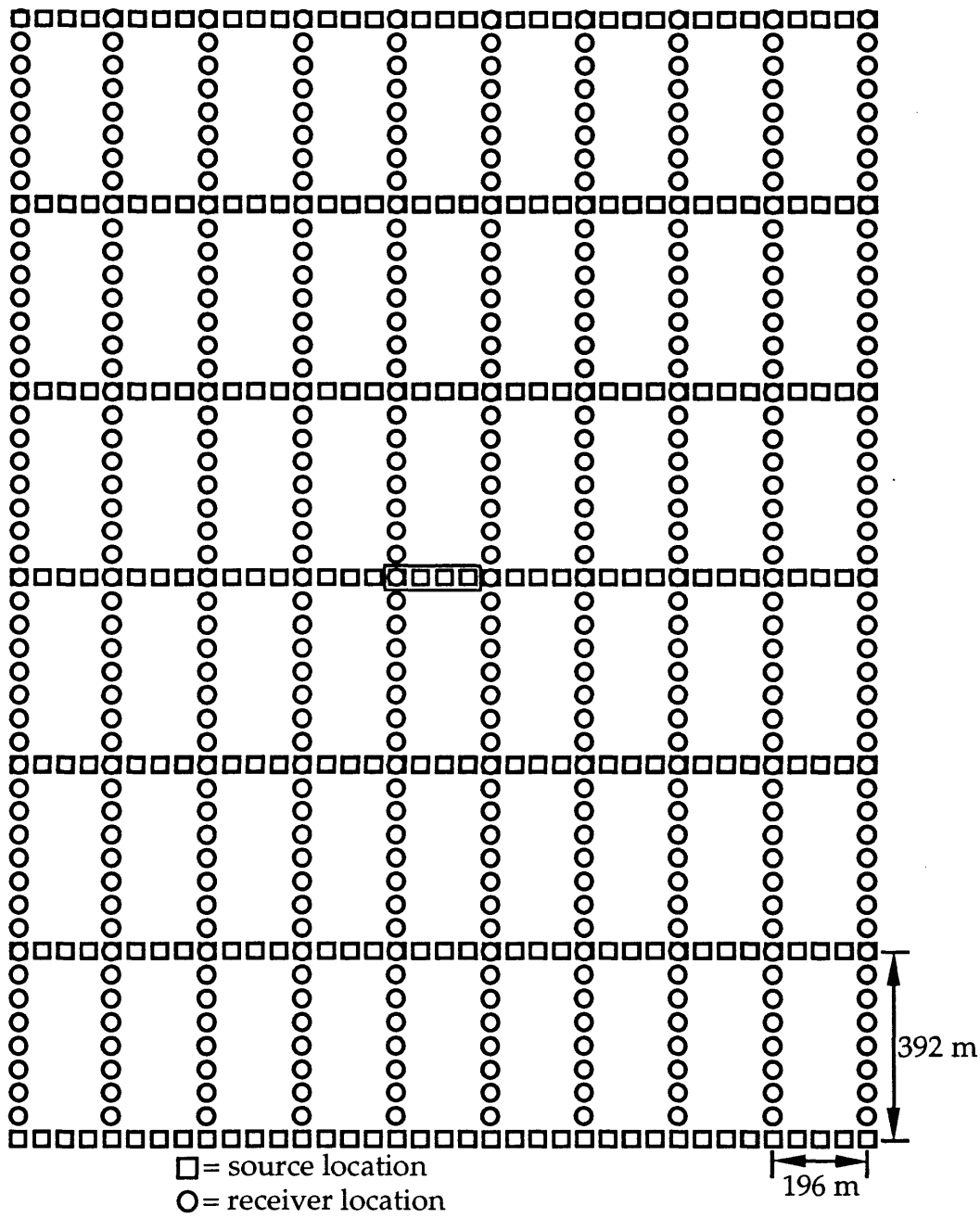
FIG. 5.33 This diagram indicates the full 3-D survey showing the source and receiver locations used in the acquisition of the full-offset 3-D survey in the physical modeling tank. This diagram also shows that all the receivers are active for the four highlighted sources. The receiver patch consists of 10 receiver lines by 48 receivers per line for a total receiver patch of 480 receivers for each source location.

CHAPTER 6   3-D PHYSICAL MODELING DATA

6.1 Introduction

Two sets of 3-D seismic data; a zero-offset and a full-offset 3-D data set, were acquired over the physical model using the University of Calgary's physical modeling tank. The data sets were acquired using the physical acquisition hardware in the modeling tank and a Perkin Elmer minicomputer was used to store the seismic data. The seismic data were processed using ITA/Landmark processing software on the Sun workstation cluster at the University of Calgary.

The physical model was constructed using a 1:7000 distance scale factor, a 1:5000 time scale factor and a 1:1.4 velocity scale factor. These scale factors allow a significant area to be model with a reasonably sized physical model. All figures and maps in this chapter are shown in world (scaled) units.

6.1.1 Implementation 3-D survey design in physical modeling tank

Two 3-D surveys were acquired over the physical model in the physical modeling tank. These two surveys both used the same time, distance and velocity scale factors of 1:5000, 1:7000 and 1:1.4 respectively. The first 3-D survey acquired was a zero-offset 3-D which encompassed the lateral bar, channel splay and point bar. The acquisition parameters for this survey are indicated in Table 6.1. This data set was acquired as a series of closely spaced 2-D lines with a single receiver active for each source location and was processed as a 3-D volume.

The second 3-D data set acquired over the physical model was a full-offset 3-D survey. This survey encompassed the point bar, channel splay and lateral bar. The acquisition parameters for this survey are indicated in Table 6.2. To acquire this 3-D survey, two receivers were active for each source location in the tank.

This allows the recording of a patch of receivers about a source beam position without having to move the model or source. Data were recorded at stations on one side of the source location with one receiver and on the other side of the source location with the second receiver. A receiver patch was recorded for each source location by having the source move to the correct location, then the two receivers simultaneously moved through all the receiver locations for that particular patch. This produced 100 individual receiver patches for the entire 3-D survey.

TABLE 6.1   3-D zero-offset acquisition parameters (world units)

900 m between the top of the model and the plane of the transducers

24.5 m station interval for shot and receivers

24.5 m line interval for shot and receiver lines

99 shot lines with 100 source locations

100 receiver lines with 99 receiver locations

3.5 m offset between source and receiver

TABLE 6.2   3-D full-offset acquisition parameters (world units)

900 m between the top of the model and the plane of the transducers

7 source lines at 392 m spacing

10 receiver lines at 196 m spacing

49 m source and receiver spacing

receiver patch consists of 480 channels (10 receiver lines by 48 receivers)

6.2 Zero-offset 3-D data processing

A zero-offset 3-D survey, consisting of 100 crosslines by 99 inlines, was acquired over the physical model, as shown in Figure 6.1. This zero-offset survey was then processed using ITA's 3-D processing software. Table 6.3 lists the data
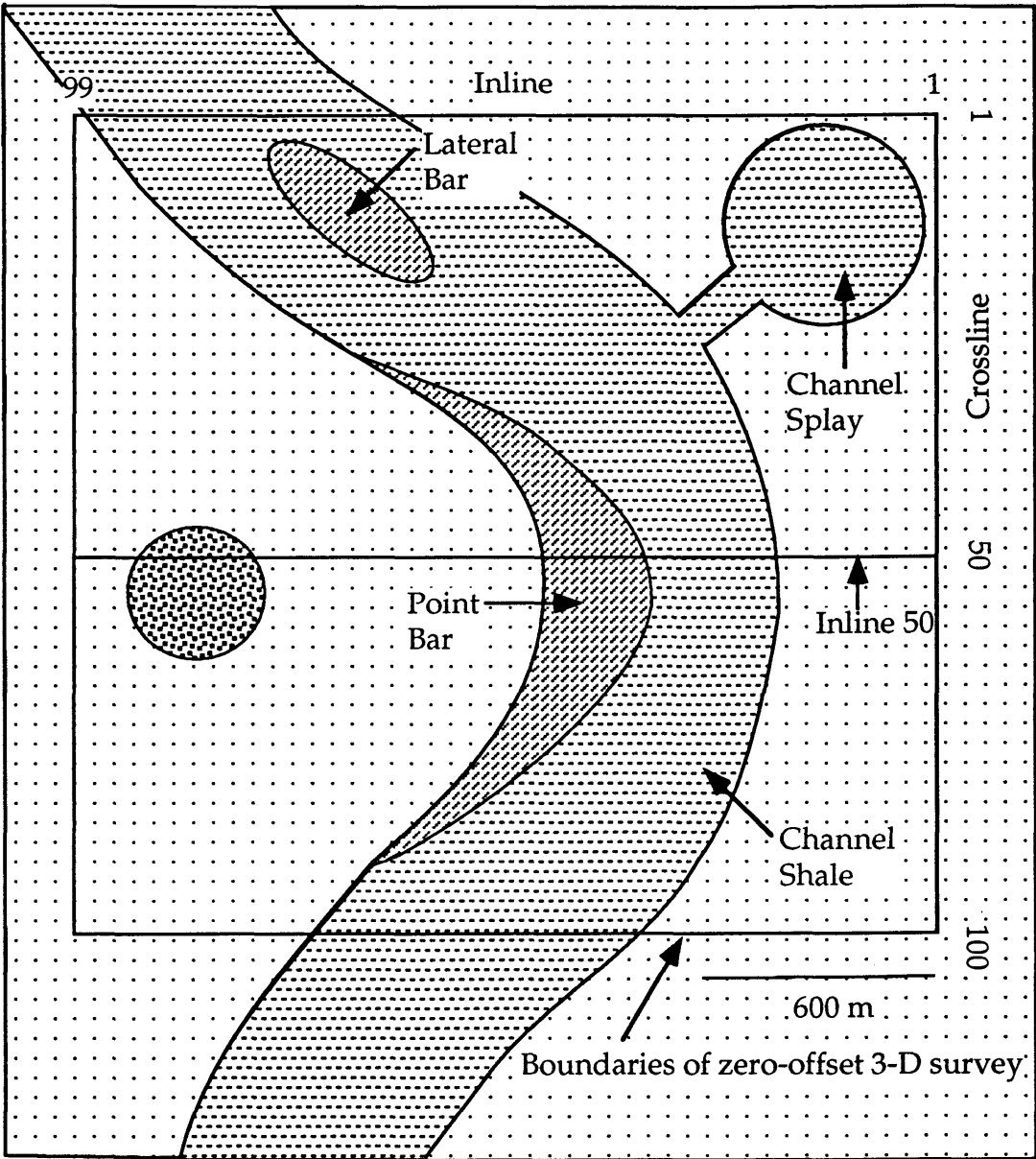
FIG. 6.1 A schematic diagram of the physical model with the top layer removed (Mannville Formation) showing the location over the physical model of the zero-offset 3-D survey consisting of 100 crossline by 99 inlines. The horizontal dashes are the channel shale, angled dashes are the point and lateral bars, dots are Glauconitic Formation and circle to the left of the point bar is the high spot in the Bantry shale.

processing procedure.

Table 6.3   3-D zero-offset processing procedure

Geometry

↓

Flat Mute ——►Predictive Deconvolution

↓

Fill-3D

↓

Migration
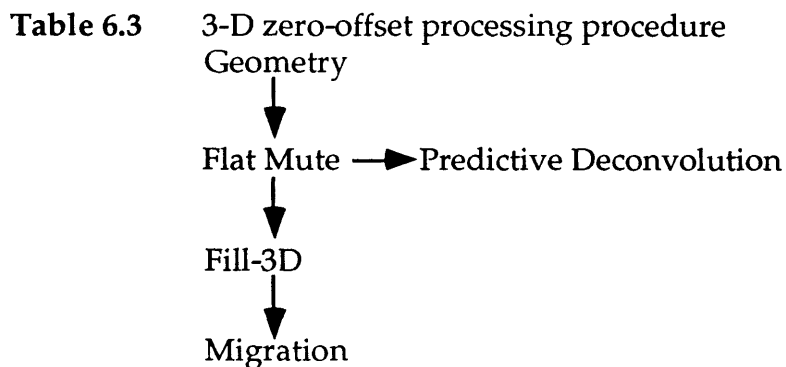
6.2.1 Geometry

The data recorded in the physical modeling tank are recorded in sequential format so no demultiplexing of the data is required. Therefore, the geometry step consists of converting the closely spaced 2-D acquisition geometry to 3-D acquisition geometry. Figure 6.2 shows a schematic diagram of the initial 2-D acquisition geometry in the physical modeling tank and the conversion to 3-D acquisition geometry. The data was initially recorded as a series of 2-D lines with one receiver used for each source location. The offset distance between the source and receiver was so small that it was not necessary to make an NMO correction. Figure 6.2 shows that receiver position $R11$ was used for source position $S11$ and receiver position $R12$ was used for source position $S12$ etc. Once the 3-D geometry is inserted into the trace headers, the 2-D lines in Figure 6.2 become source lines (inlines) whereas the first receiver position on each 2-D line indicates the position of the first receiver line (crossline) in the 3-D volume and the second receiver position on each 2-D line indicates the position of the second receiver line in the 3-D volume etc. This conversion of the 2-D lines forms the 3-D volume.

6.2.2 Mute

Because this survey was recorded in the physical modeling tank, no refraction or elevation statics were applied to the data and the direct arriving energy could be muted from each trace on every shot in the entire survey using a common mute pattern. Figure 6.3 shows inline 50 from the 3-D volume after the

Line 4 (inline 4)   (S41) [R41]   (S42) [R42]   (S43) [R43]

Line 3 (inline 3)   (S31) [R31]   (S32) [R32]   (S33) [R33]

Line 2 (inline 2)   (S21) [R21]   (S22) [R22]   (S23) [R23]

Line 1 (inline 1)   (S11) [R11]   (S12) [R12]   (S13) [R13]

(crossline 1)   (crossline 2)   (crossline 3)
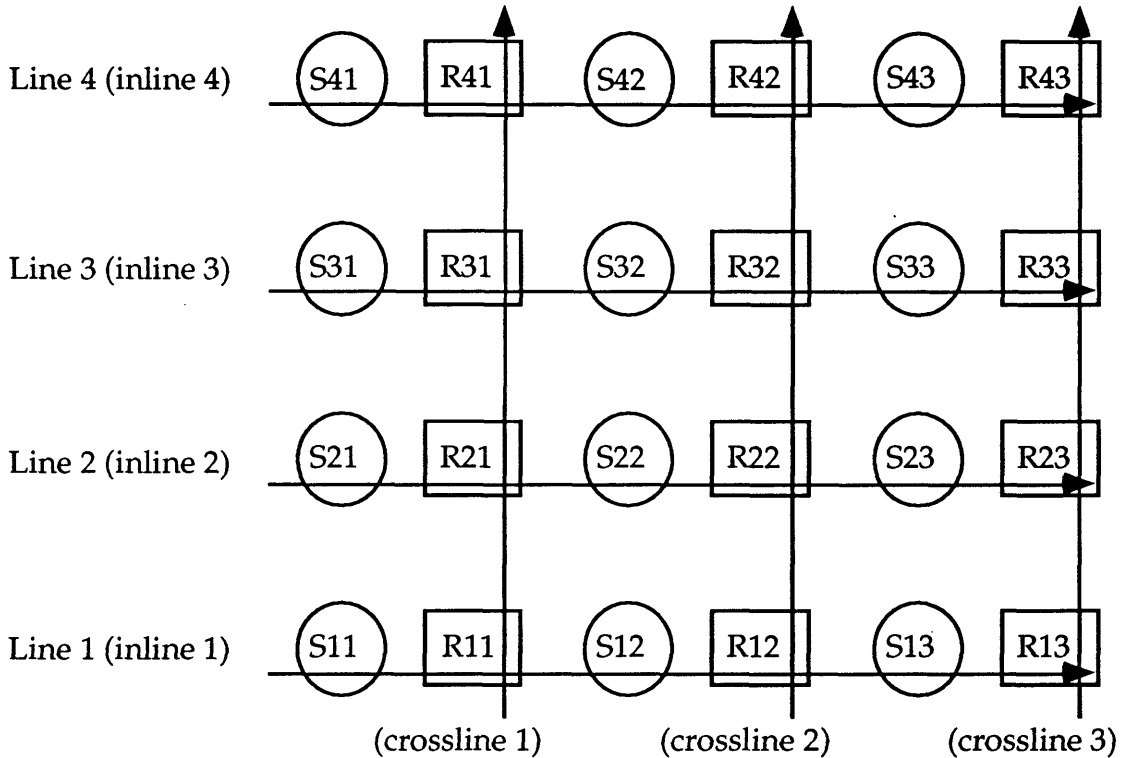
FIG. 6.2 3-D zero-offset acquisition scheme. The unbracketed seismic line captions are the initial 2-D seismic lines acquired in the physical modeling tank and the bracketed line captions are after the application of 3-D geometry.

flat mute was applied to the data. Figure 6.1 indicates the location of inline 50 with respect to the physical model and it shows that inline 50 is perpendicular to the channel bend and that it passes almost through the center of the point bar.

The Mannville event is at approximately 0.92 s on Figure 6.3 and it is indicated by the *KM* event on this figure. It is a strong amplitude peak with good continuity across the section. A strong amplitude peak-trough doublet that
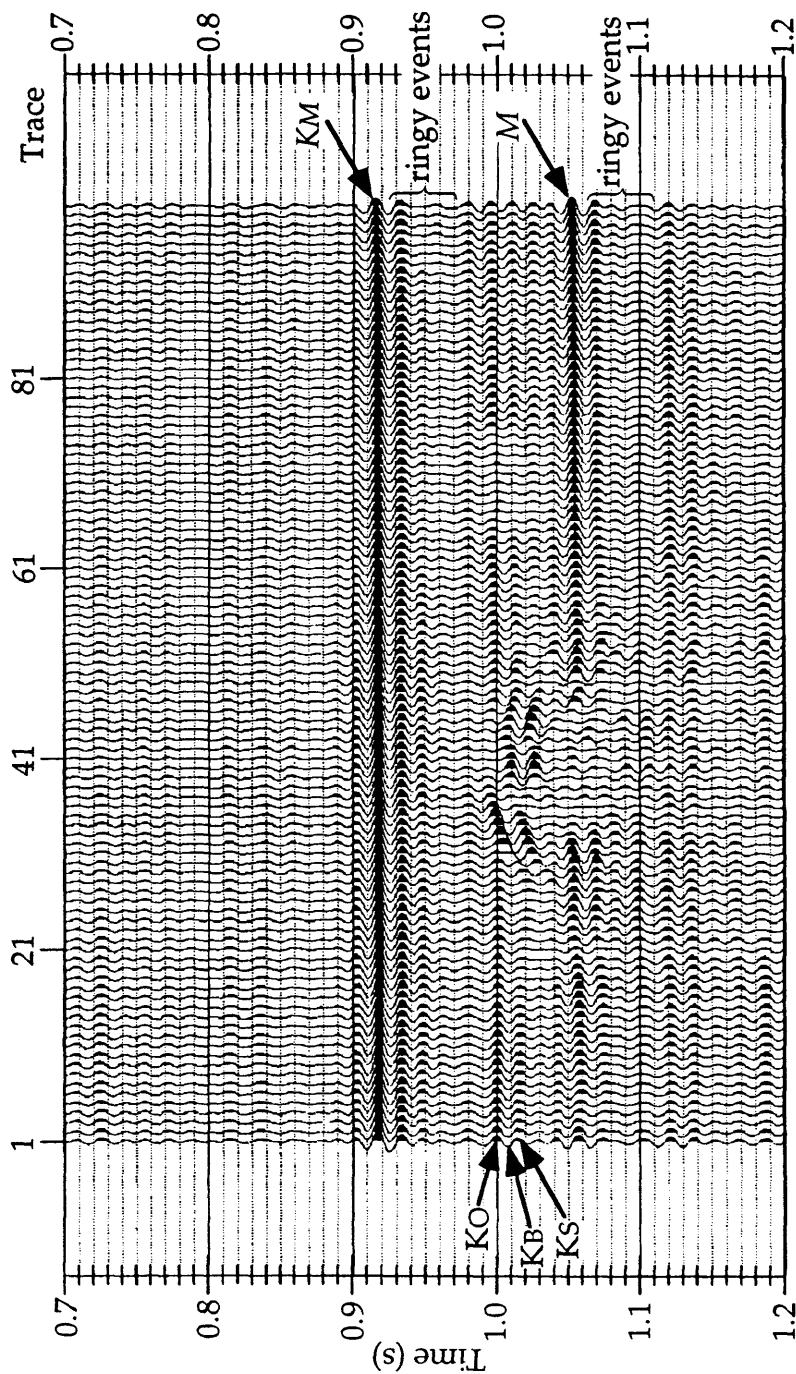
FIG. 6.3 Inline 50 from the zero-offset 3-D which lies perpendicular to the channel bend and passes almost through the center of the point bar. The events marked *KM* and *M* represent reflected energy from the top of the physical model and the top of the aluminum plate which represent the Mannville and Mississippian formations respectively. The ringy events are caused by a ringy wavelet used in the physical modeling tank when acquiring the seismic data. The trace spacing is 3.5 meters.

occurs at 1.0 to 1.07 s on Figure 6.3 represents the Ostracod limestone (KO) and Bantry shale (KB) respectively. The Ostracod limestone event disappears on Figure 6.3 between traces 66 and 76 corresponding to the Bantry shale high shown in Figure 6.1. There is a weak peak directly below the Bantry trough that represents the top of the Sunburst Formation (KS). The strong peak at 1.055 s on Figure 6.3 represents the top Mississippian event (M). The trough of the Bantry shale and weak Sunburst peak decline in amplitude approximately at trace 16 and this is interpreted to indicate the start of the channel. This decline in amplitude of the trough-peak doublet also corresponds to a pull-up on the Mississippian event caused by the high-velocity channel shale. There is a slightly left dipping event on traces 28 to 38 occurring between 1.00 to 1.028 s that is from the top of the point bar. This event declines in amplitude and levels out at 1.001 s at trace 40 and it stays as a very weak peak to trace 45 where it appears to merge back into the Bantry event. The point bar seems to attenuate all the energy passing through it so there appears to be a break in the Mississippian reflector below.

Inline 50 from the zero-offset 3-D survey (Figure 6.3) nearly coincided with the location over the physical model of the high resolution 2-D line (Figure 4.8). The high resolution 2-D line seems to image the top and dipping face of the point bar and the topographic high in Bantry Shale better than the 3-D zero offset line. This may be due to the higher fold coverage (20 fold) on the 2-D verses the single-fold coverage on the zero-offset 3-D line.

6.2.3 Predictive deconvolution

There are a series of low amplitude peaks immediately following the KM and M events on Figure 6.3 that are caused by a ringy seismic wavelet used to acquire the data set in the physical modeling tank. To remove this ringy appearance a

conventional spiking deconvolution was applied to the data set but it did not have much effect on the ringy appearance of the data. It was then decided to treat these ringy events following the *KM* and *M* events on the data set as multiples and try to remove them using a predictive or gap deconvolution. There are two critical parameters when designing a predictive deconvolution; the gap length or prediction distance and the prediction length (see Figure 6.4). The
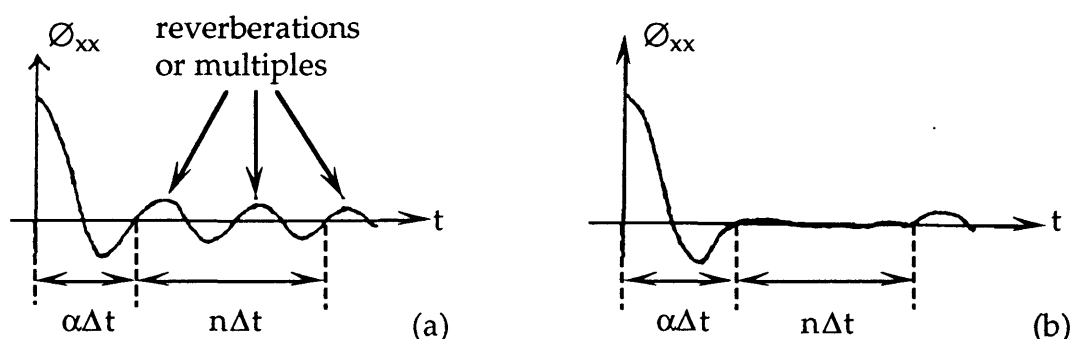
$\alpha\Delta t$ = prediction distance

$n\Delta t$ = prediction length

$\varnothing_{xx}$ = autocorrelation of trace

FIG. 6.4 The autocorrelation of the trace: a) before and b) after predictive deconvolution (Krebes, 1989).

prediction distance must be of sufficient length to pass the wavelet information but must be short enough to suppress multiples. The prediction length is a parameter that specifies the range of reverberatory energy to be suppressed. To determine the correct prediction distance, the autocorrelation of the seismic trace is calculated and the prediction distance is taken as the second zero crossing of the autocorrelation (Robinson and Treitel, 1980), or it can also be determined by trial and error by applying different prediction distances to the stacked section, and choosing the prediction distance that suppresses the multiples. Figure 6.5 shows inline 50 from the 3-D volume that has had a predictive deconvolution
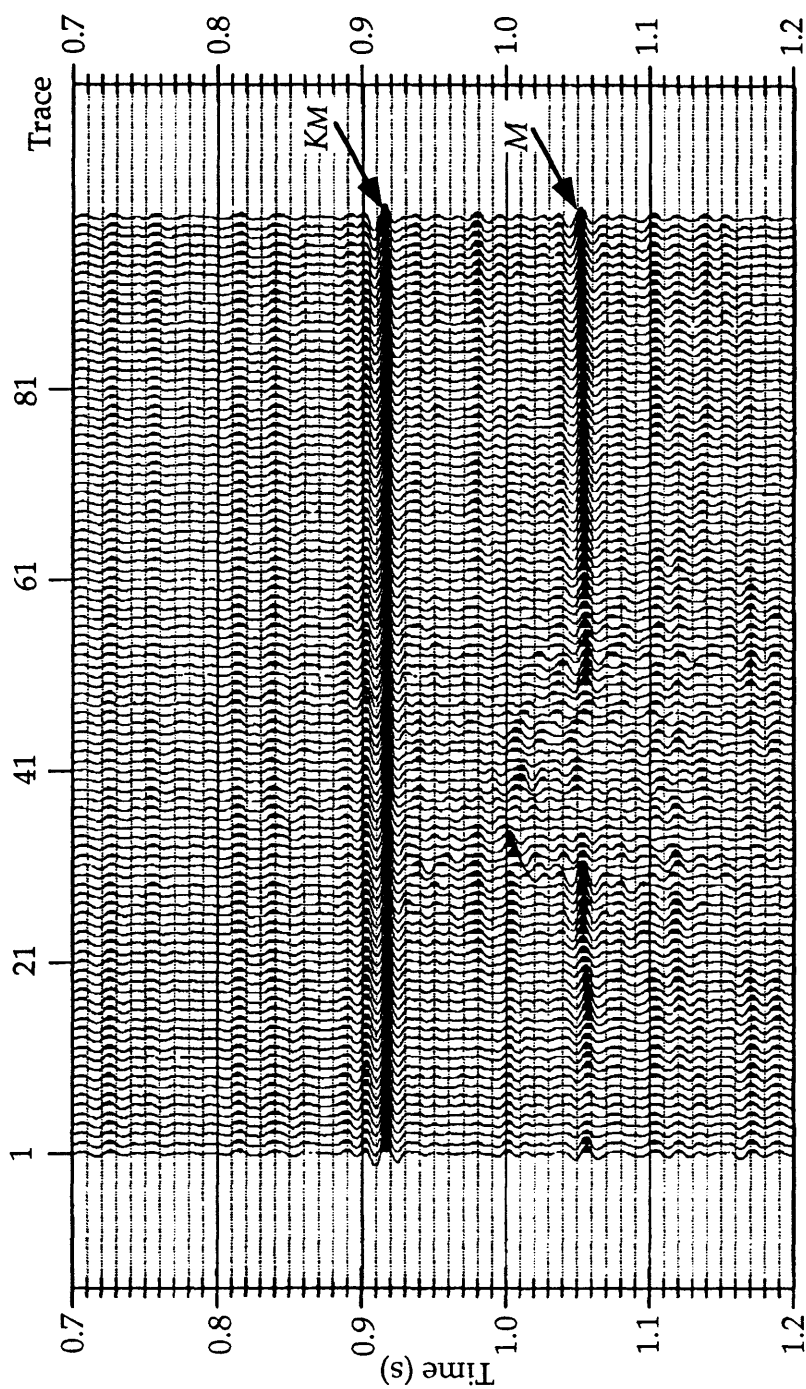
FIG. 6.5 Inline 50 from the zero-offset 3-D which has had a predictive deconvolution with a 18 millisecond prediction distance and a 80 millisecond prediction length applied to the stacked data. The events marked *KM* and *M* represent reflected energy from the top of the physical model and the top of the aluminum plate which represent the Mannville and Mississippian formations respectively. The trace spacing is 3.5 meters.

with a 18 ms prediction distance and a 80 ms prediction length applied to the section. This has largely removed the ringy events that follow the *KM* and *M* events on this section. The predictive deconvolution has also removed the Sunburst event from the section and it has mostly removed the Ostracod Bantry peak-trough doublet from the section leaving these events only on traces 1 to 30. There is another event at 0.98 s on Figure 6.3 that is above the Ostracod/Bantry events. This event becomes the primary event in the predictive deconvolution design and Ostracod, Bantry and Sunburst events are taken to be multiples and suppressed. This is undesirable, so predictive deconvolution was not used for the 3-D zero-offset survey. It was decided to leave the multiples alone as they only affect the velocity analysis by making it hard to pick the normal move out velocity but since the offset is so small in the zero-offset survey there is no need to apply a normal move out correction.

6.2.4 Fill-3D

The data volume was then processed using an ITA program called "Fill-3D" that fills in any missing traces if the 3-D volume is not square or rectangular. Also at this time the format of the data in the cubed volume was changed from each trace in the data volume being an individual record to each inline forming an individual record with the crosslines becoming traces in each record. This format is required by any of the ITA poststack processes such as poststack migration.

6.2.5 Migration

The filled 3-D volume was then migrated using a one-pass 3-D phase-shift migration to collapse diffractions and move dipping reflectors to their true subsurface position (Yilmaz, 1987). In Figure 6.5, diffractions can be observed

from the channel structure between 1.0 to 1.05 seconds on traces 28 to 35 and 37 to 53. These diffractions are collapsed on Figure 6.6 to form the channel event between 1.0 and 1.03 seconds.

The migrated zero-offset line (Figure 6.6) produces a low resolution image of the point bar, channel shale and topographic high on the Bantry Shale compared to the migrated versions of the 2-D high resolution line (Figures 4.9-4.11). The better imaging on the 2-D line has to be due to the higher fold coverage (20 fold) on the 2-D line than the single-fold coverage on the zero-offset 3-D line.

6.3 Interpretation

Figure 6.7a is a horizon map with the Mannville event interpreted on every tenth line of the phase-shift migrated 3-D volume in both the inline and crossline directions. This figure indicates that the Mannville horizon is fairly flat (extensive purple color on Figure 6.7a) except for about a 10 millisecond pull-up (to the red color on Figure 6.7a) between inlines 1 to 35 and crosslines 1 to 90.

Figure 6.7b shows a horizon map with the top of the Mississippian event interpreted on every tenth line of the migrated 3-D volume in both the inline and crossline direction. The channel is indicated on this figure by the pull-up of approximately 4 milliseconds on the Mississippian horizon from the green background color to the red color on Figure 6.7b. This pull-up is caused by the high-velocity shale that fills the channel and the channel splay. The point and lateral bars are indicated by the push-down of the Mississippian horizon in the channel to the blue color for the point bar and the green color for the lateral bar which is approximately 8 and 3 milliseconds respectively and is caused by the low-velocity sand in the bar complexes.
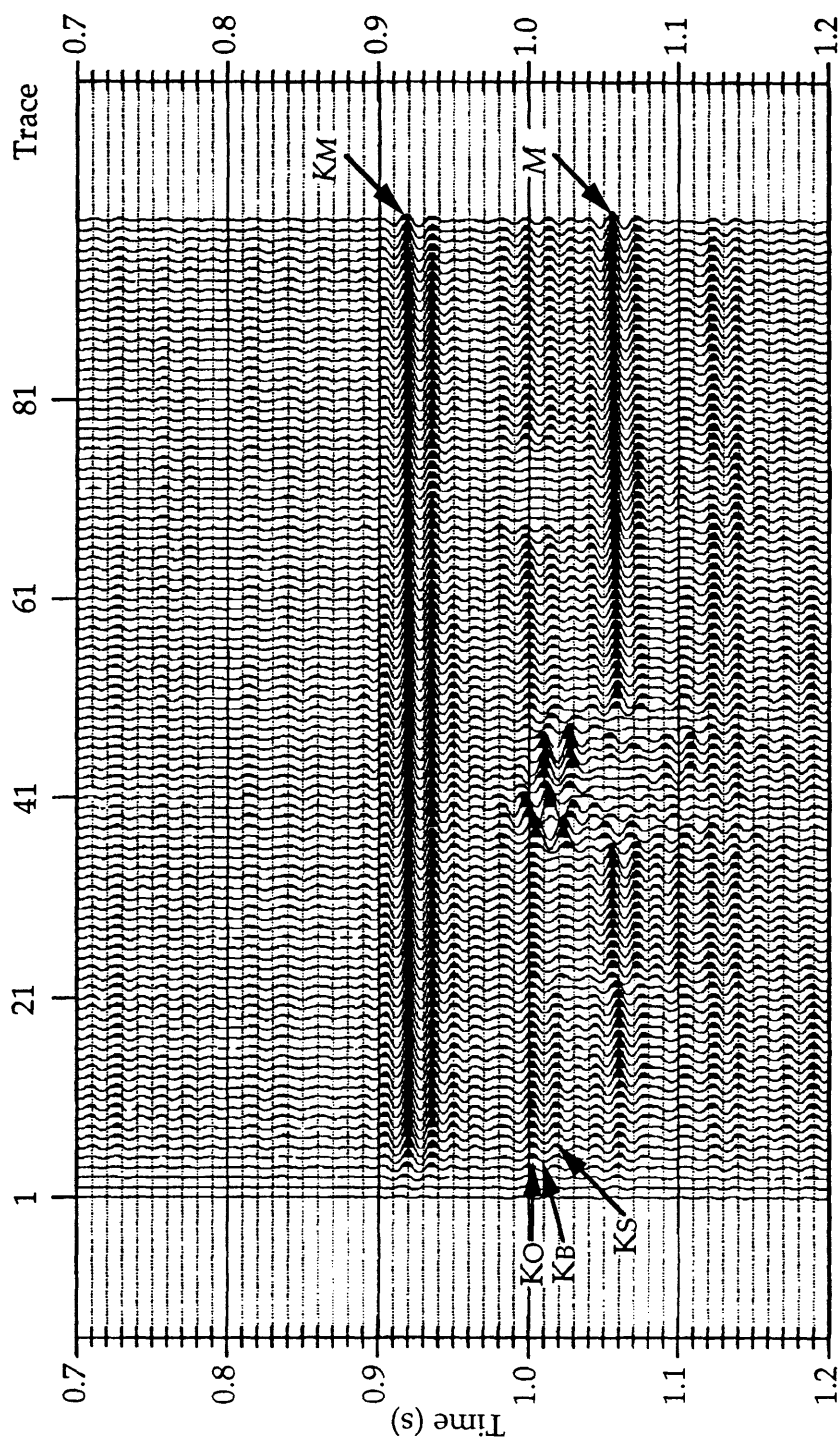
FIG. 6.6 Inline 50 from the zero-offset 3-D data volume which has been migrated using a one-pass 3-D phase-shift migration. The events marked KM and M represent reflected energy from the top of the physical model and the top of the aluminum plate which represent the Mannville and Mississippian formations respectively. The trace spacing is 3.5 meters.
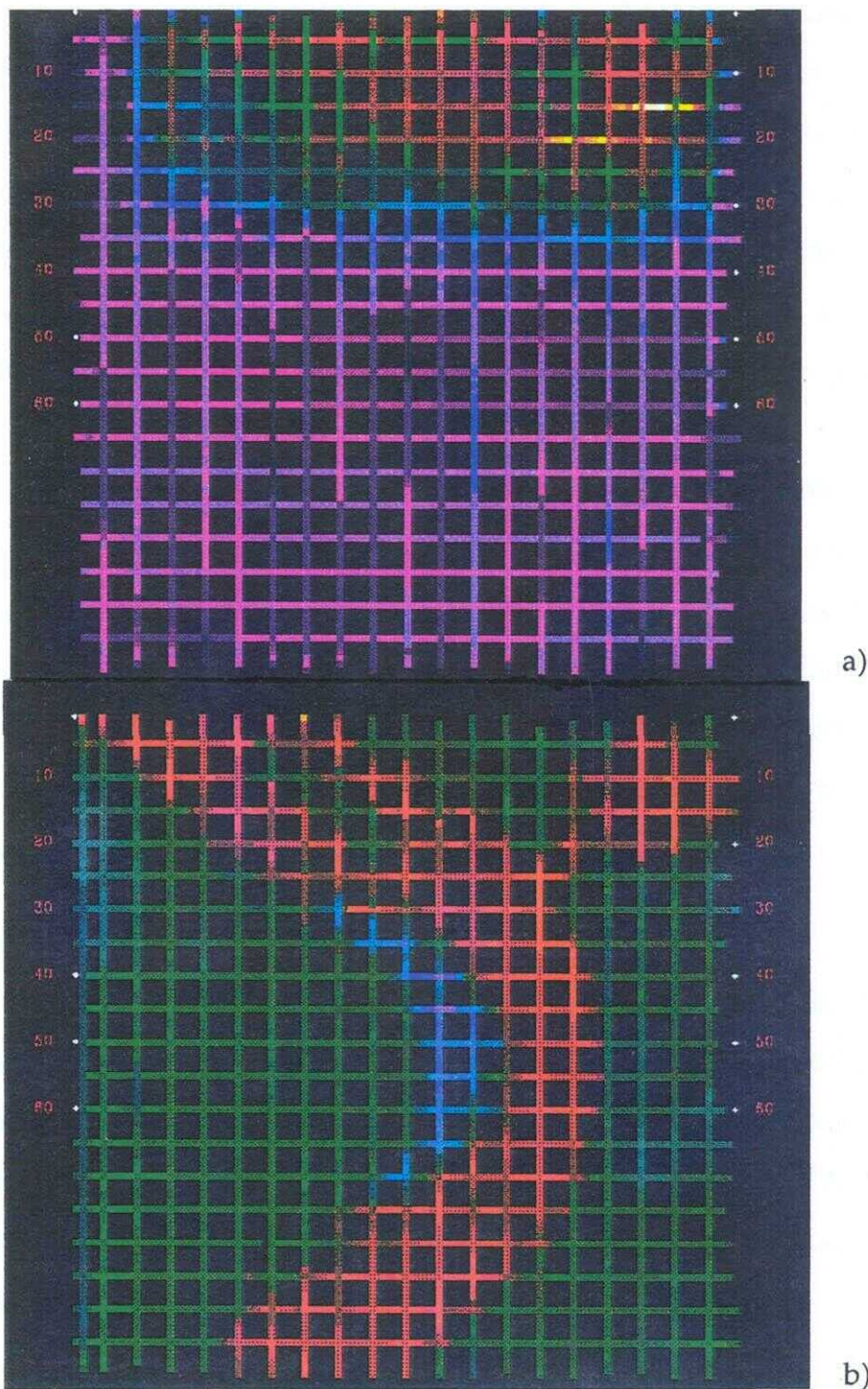
FIG. 6.7 Horizon maps from the zero-offset 3-D survey indicating a) top Mannville Formation and b) top Mississippian Formation. Color scheme is yellow is the shallowest time and red, green, blue, and purple are succesively deeper times on each diagram.

Figure 6.8a is a time slice at the 0.980 s level from the migrated zero-offset 3-D data set and it indicates the amplitude of the reflected energy from the physical model at this travel time. This figure shows the circular topographic high on the Bantry shale as a slight decrease in amplitude of the reflection produced by defocusing of the reflected energy from the top of the dome structure. The tops of the point and lateral bars are indicated on this figure by a decrease in amplitude of reflection from these structures compared to the surrounding events.

A time slice at the 1.016 s level from the migrated zero-offset 3-D data set is shown in Figure 6.8b. The shale-filled channel and channel splay are indicated on this figure by a decrease in the amplitude of the reflection from these structures compared to the surrounding events. The point and lateral bars are indicated on this figure by a larger negative amplitude reflection from these features compared to the shale filled channel and events surrounding the channel.

6.4 Full-offset 3-D survey

A full-offset 3-D survey was acquired as a true 3-D volume with 480 receiver positions recorded for each source location. Figure 6.9 shows the location of this 3-D survey (7 source lines and 10 receiver lines) with respect to the physical model. The 3-D survey was processed using ITA/Landmark processing software. Table 6.4 lists the data processing procedure which was used to process this survey.

6.4.1 Geometry, flat mute and predictive deconvolution

The data were recorded in the physical modeling tank in a trace sequential format so no demultiplexing of data was required. The geometry consisted of
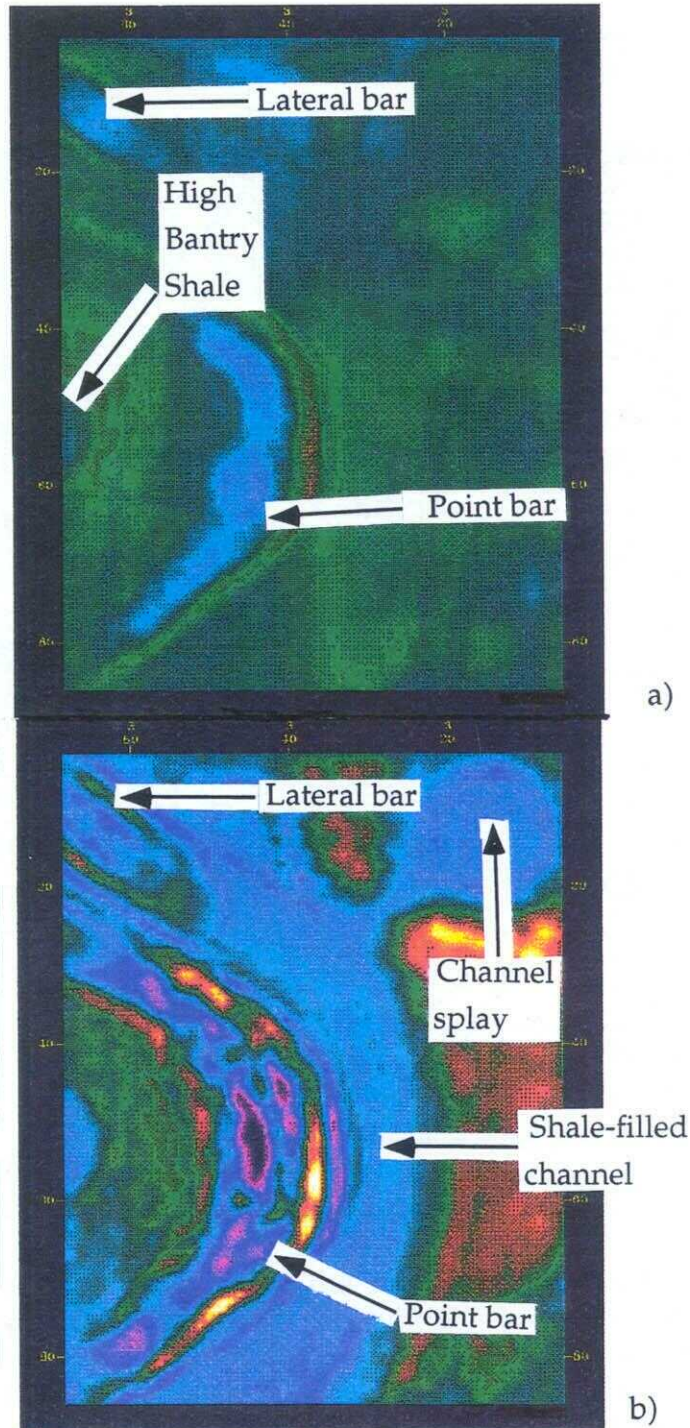
FIG. 6.8 Time slices from the zero-offset 3-D survey at a) 980 ms and b) 1016 ms, indicating topographic high in the Bantry shale, point and lateral bars, shale-filled channel and splay. Color scheme is yellow is largest positive amplitude and amplitudes decline through red, green, blue, purple and black which is largest negative amplitude on each diagram.
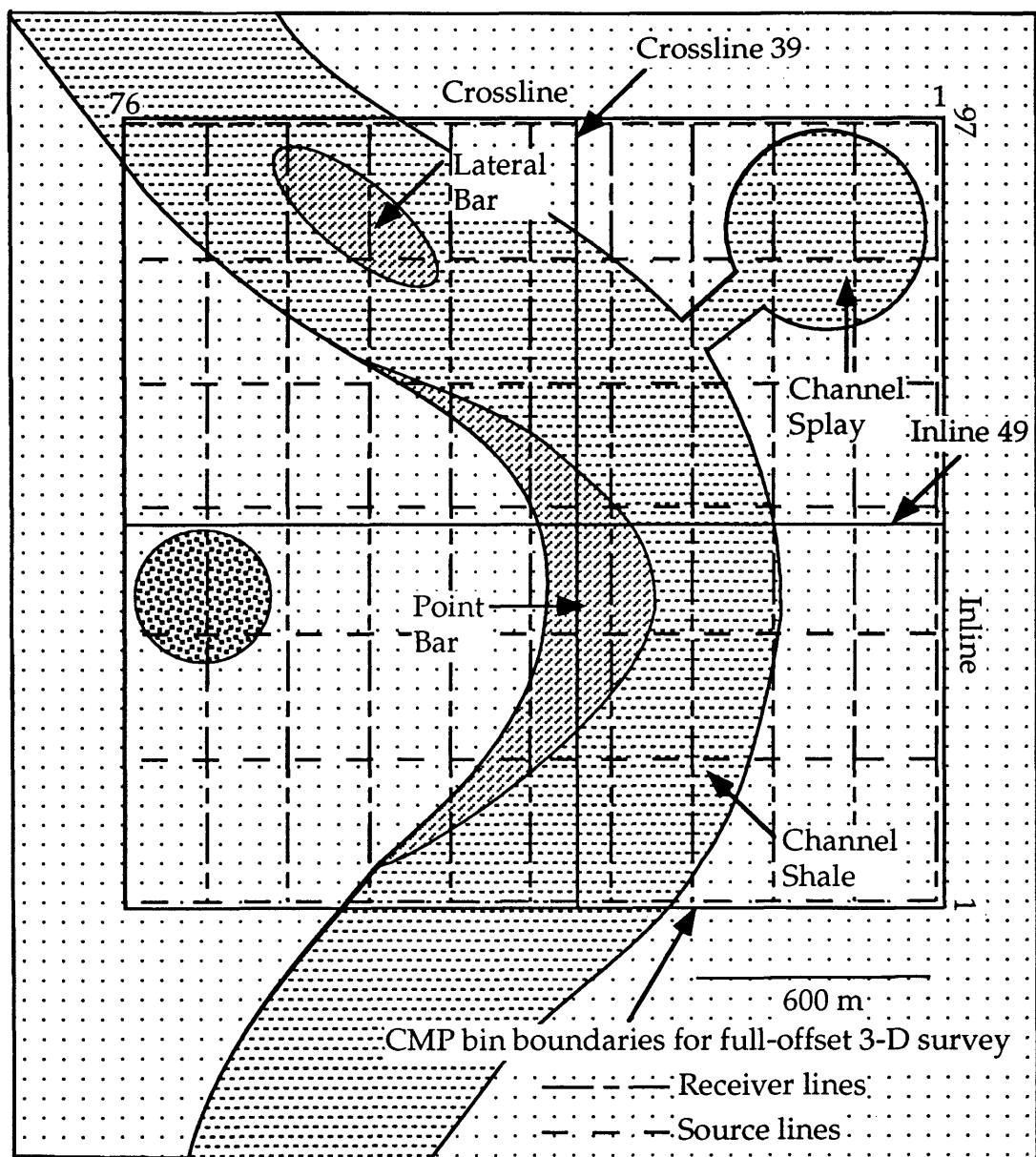
FIG. 6.9 A schematic diagram of the physical model with the top layer removed (Mannville Formation) showing the location over the physical model of the full-offset 3-D survey which consisted of 7 source lines and 10 receiver lines and produces a survey with 97 inline CMP bins by 76 crossline CMP bins. The short dashed lines are source lines while mixed long and short dash lines are receiver lines. The horizontal dashed objects are the channel shale, angled dash objects are the point and lateral bars, dotted objects are Glauconitic Formation and circle to the left of point bar is a high spot in the Bantry shale.

placing the 3-D field geometry into the trace headers of each shot and editing out the bad traces. A flat mute at all offsets was applied to each shot to remove the direct arriving energy and leave only the reflected energy. One shot shown in Figure 6.10 is presented to illustrate the muted raw shot data. This shot is displayed without any amplitude scaling and is a true amplitude plot. There are a series of low amplitude events (peaks) immediately following the *KM* and *M* events on Figure 6.10 and these are caused by the ringy wavelet used in the acquisition of this data in the physical modeling tank. This ringiness of the

Table 6.4   Full-offset 3-D processing procedure

Geometry

↓

Flat Mute

↓

Predictive Deconvolution

↓

Sort to Common Midpoint

↓

Velocity Analysis   Residual Statics

↓

Normal Move Out Correction

↓

Mute

↓

Stack

↓

Bandpass Filter

↓

Dejaggle

↓

Fill-3D

↓

Migration
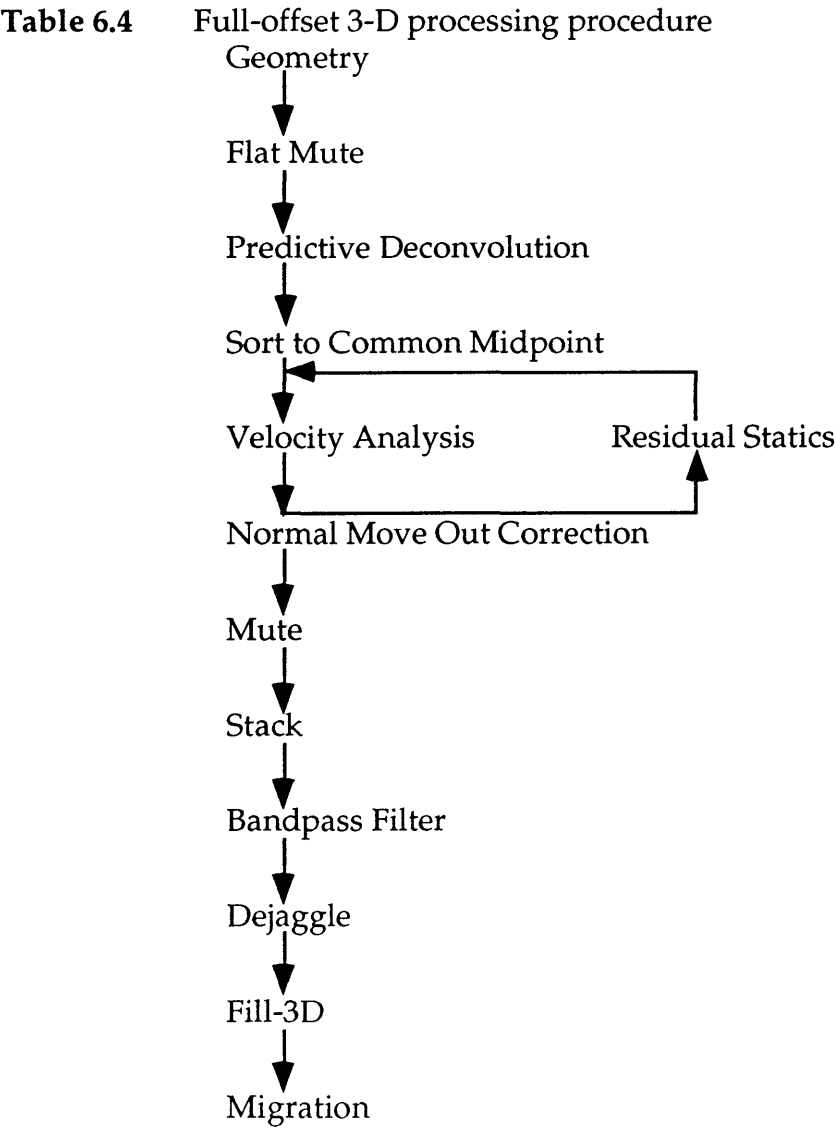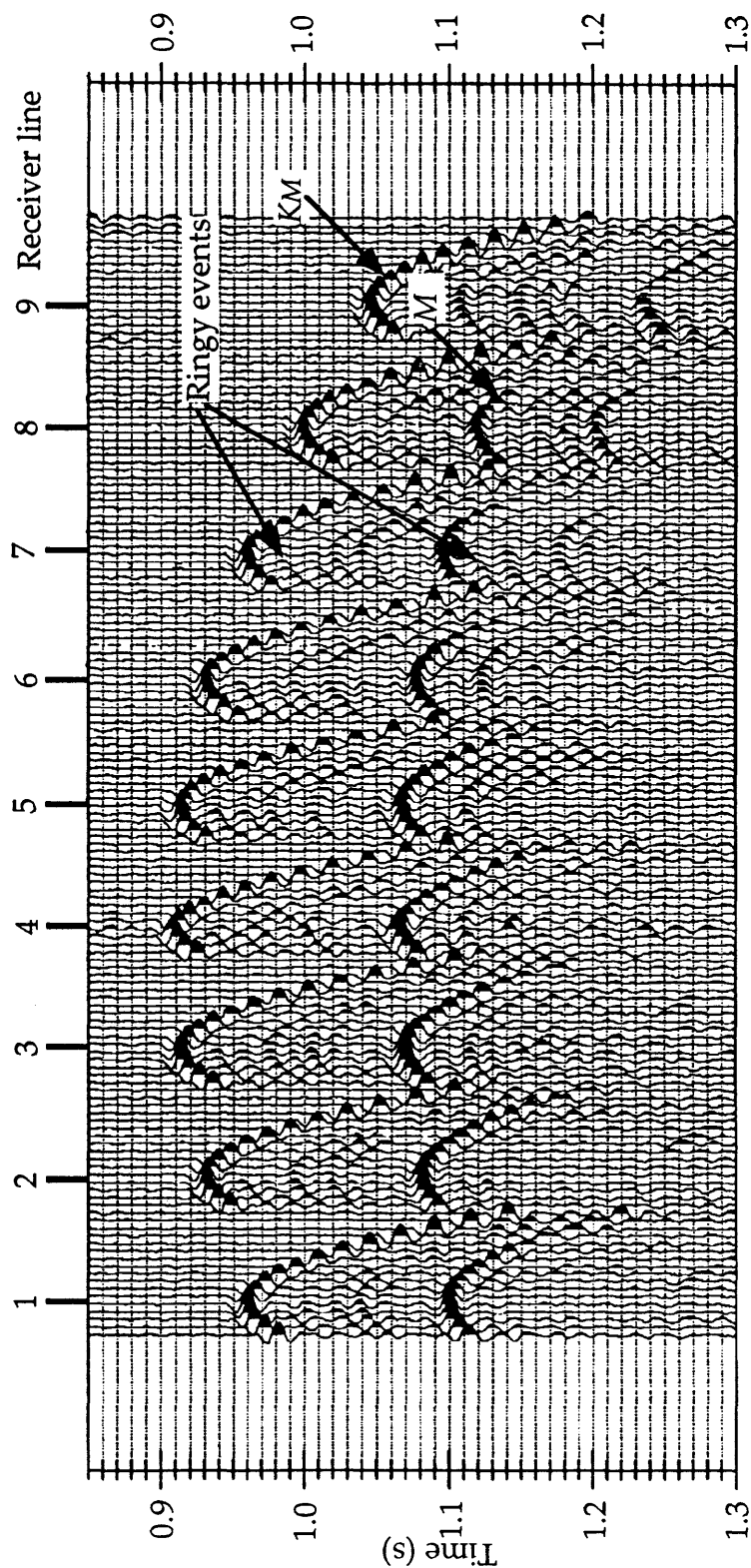
FIG. 6.10 A shot from the full-offset 3-D survey which has been muted with a flat mute at all offsets to remove direct arriving energy. The events marked *KM* and *M* represent reflected energy from the top of the physical model and the top of the aluminum plate which represent the Mannville and Mississippian formations respectively. The ringy events are caused by a ringy wavelet used in the physical modeling tank when acquiring the seismic data.

wavelet was suppressed by applying a predictive deconvolution with a 24 ms prediction distance and a 80 ms prediction length to the shot data. This was a different prediction distance than the zero offset survey because the wavelet used in the acquisition of this data set was slightly longer than the wavelet used in the zero offset survey and this is due to the adjustably of the duration of the wavelet used in the physical modeling tank. Figure 6.11 is the same shot as Figure 6.10 with the predictive deconvolution applied. It has reduced the amplitudes of the peaks immediately following the *KM* and *M* events on this shot record. This predictive deconvolution was used on the full-offset 3-D survey as it reduced the multiples following major events on the section and this made the velocity analysis much easier and much more reliable. The predictive deconvolution was not applied to the zero offset 3-D survey as velocity analysis was never performed on that data set as the offset distance between the source and receivers are so small that normal move out correction was not needed.

6.4.2 CMP, velocity analysis and residual statics

The muted shots were then sorted into common midpoint (CMP) bins to produce a 3-D data volume that consists of 97 inline bins by 76 crossline bins. A semblance velocity analysis was performed upon 3 X 3 superbins to determine stack or normal move out (NMO) velocity. It was decided to use 3 X 3 superbins during the velocity analysis as this gave a full range of offsets and made it easier to pick reliable NMO velocities. For every velocity analysis location, the ITA program uses five pairs of semblance records which contain source-receiver azimuthal information from; a) all azimuths, b) -22.5 to 22.5 and 157.5 to 202.5 degrees, c) 22.5 to 67.5 and 202.5 to 247.5 degrees, d) 67.5 to 112.5 and 247.5 to 292.5 degrees and e) 112.5 to 157.5 and 292.5 to 337.5 degrees. One of the superbins showing the normal move out velocity picks used in the velocity
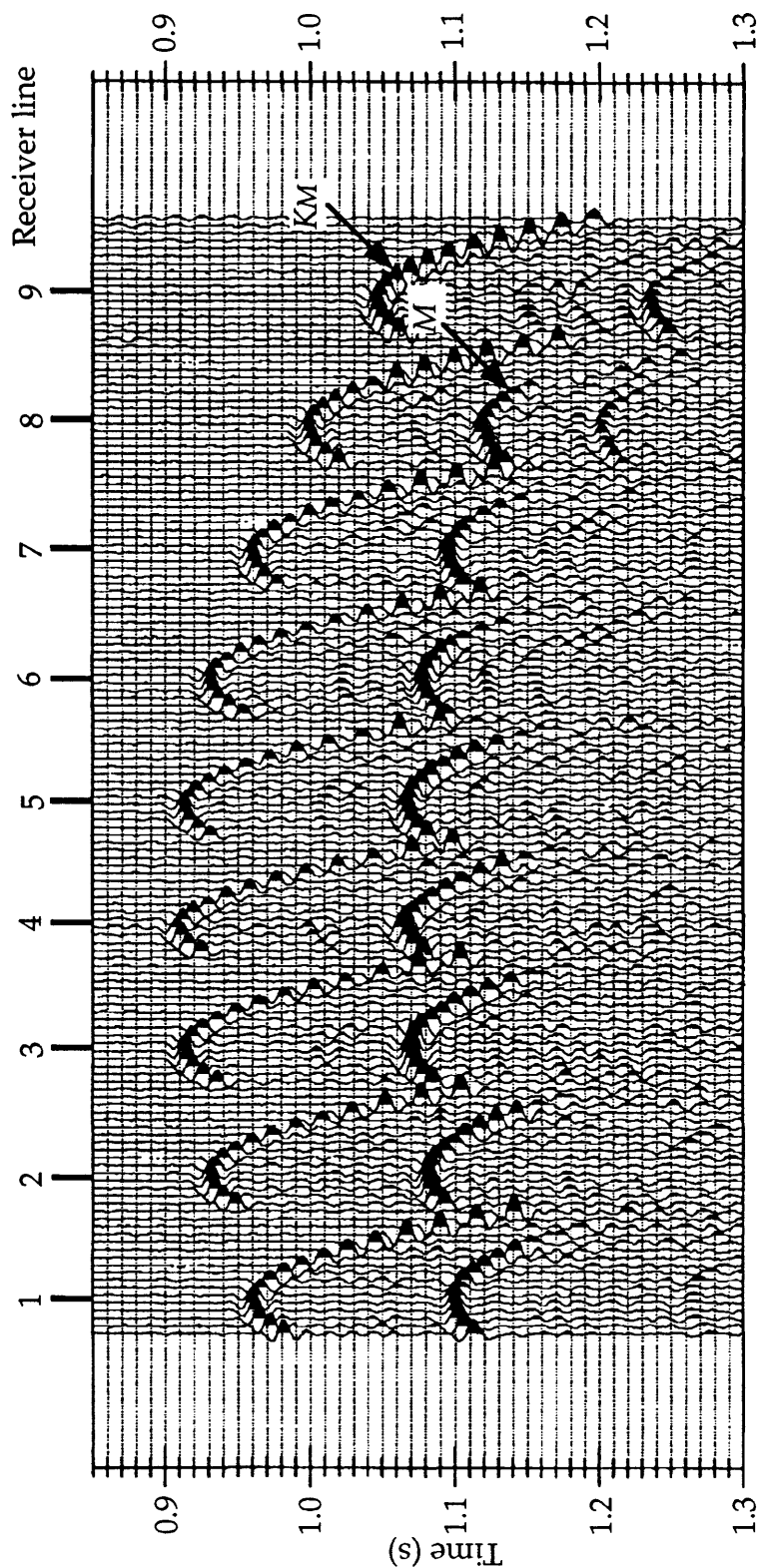
FIG. 6.11 A muted shot from full-offset 3-D which has had a predictive deconvolution with a 24 millisecond prediction distance and a 80 millisecond prediction length applied to the shot data. The events marked *KM* and *M* represent reflected energy from the top of the physical model and top of aluminum plate which represent Mannville and Mississippian formations respectively. The ringy events following the *KM* and *M* events have been largely removed by the application of predictive deconvolution.

analysis is shown in Figure 6.12. The 3 bins which contributed to each velocity analysis location are indicated by the shifts in the hyperbolic move out of each horizon on Figure 6.12, as well as the corresponding shifts in the NMO hyperbolas on this figure. Each horizon which has its velocity picked on Figure 6.12 has a ragged appearance caused by small time shifts in traces in each bin, and the NMO hyperbolas do not exactly match the hyperbolic move out of the horizons on this figure. This ragged appearance of the horizons appears to be caused by a short wavelength static in the data so it was decided to apply correlation or residual statics to the bins after each bin had been NMO corrected. The static in each bin could be caused by positioning errors of the source and receivers in the physical modeling tank. If the source and receivers are not in the correct location the offset between the source and receivers is not correct and the reflected energy from the physical model arrives later or earlier than expected and this causes the small time shifts in the horizons observed in the bins. A residual static correction was therefore applied to each bin after which the traces were re-sorted into 3 X 3 superbins and semblance velocity analysis was rerun to calculate the new NMO velocity function at each velocity location.

6.4.3 NMO correction, mute, stack and bandpass filter

The new NMO velocity functions, calculated from the 3 X 3 superbins with residual statics applied, was used to correct all traces in each bin, for NMO. There was some frequency distortion of events at the largest source-receiver offset in each bin and this was caused by NMO stretch. These distortions in each bin were removed by applying a second mute to the data to prevent distortion of events on the stacked CMP bins.

The remuted NMO-corrected bins were then stacked to improve signal to noise ratio by canceling random noise. To further remove any random noise and
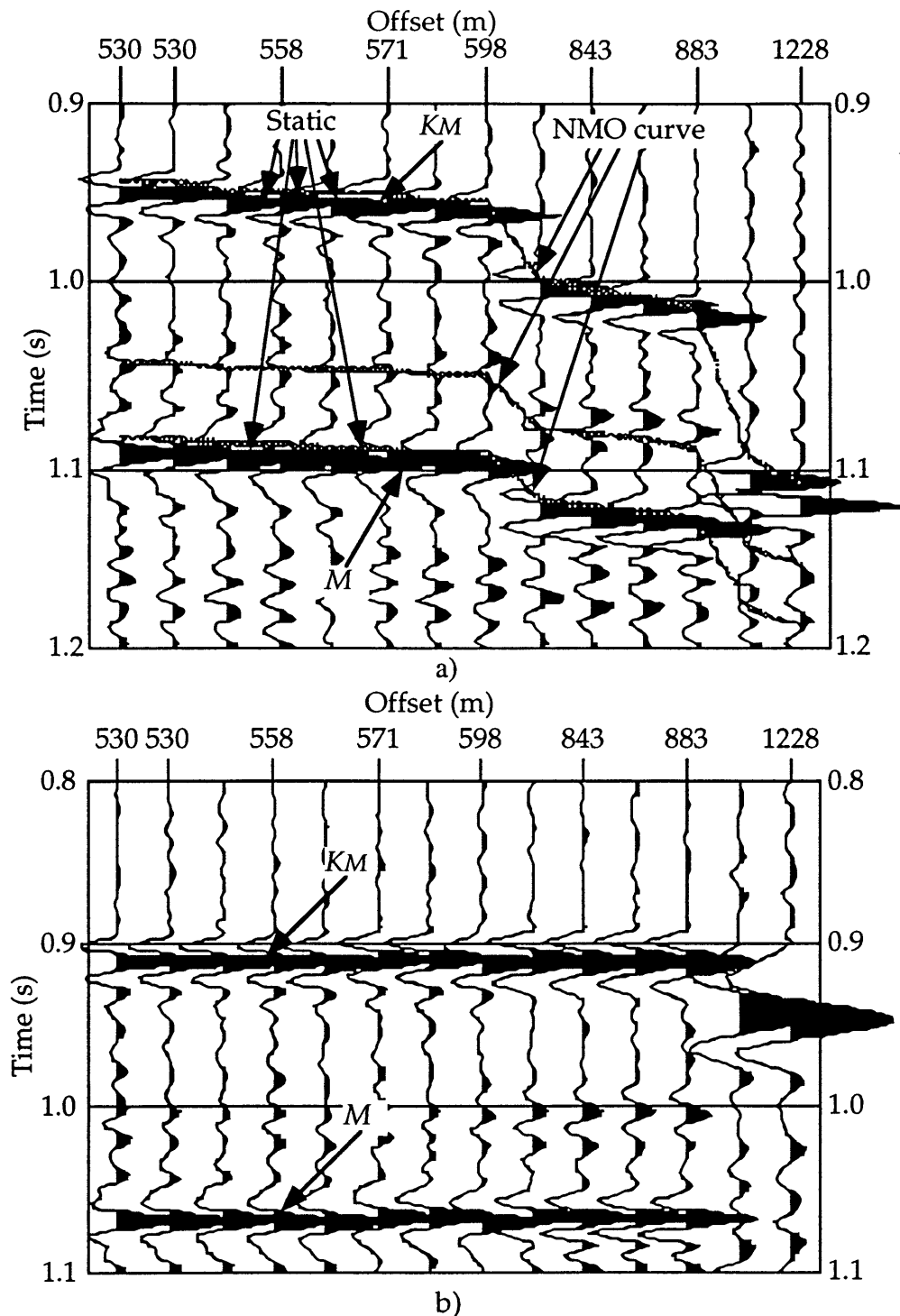
FIG 6.12 a) A 3 X 3 superbin used in the velocity analysis procedure. The events marked *KM* and *M* represent reflected energy from the top of the physical model and the top of the aluminum plate which represent the Mannville and Mississippian formations respectively. The source-receiver offset distance ranges from 530 to 1228 m in the 3 bins forming the superbin. b) same 3 X 3 superbin with normal move out correction applied.

unwanted energy outside of the desired pass band of the data, a bandpass filter was applied to the stacked data set. Figures 6.13 to 6.14 show crossline 39 and inline 49 respectively from the 3-D data volume, whose locations are indicated on Figure 6.9. The Mannville event at approximately 0.91 s on Figures 6.13 and 6.14 is a strong amplitude peak with good continuity across the sections. A medium amplitude peak-trough doublet at 1.02 s on Figures 6.13 and 6.14 represent the Ostracod limestone and Bantry shale respectively. There is a weak amplitude peak at approximately 1.025 s directly below the Bantry shale trough on Figures 6.13 and 6.14 and this represents the Sunburst Formation. The strong amplitude peak at 1.05 to 1.07 s, marked event M on Figures 6.13 and 6.14 represents the Mississippian Formation. The point bar indicated by PB on Figures 6.13 and 6.14 produces a push-down of Mississippian horizon and appears to attenuate a large portion of the high frequencies passing through the bar and this produces a lower frequency Mississippian event below the point bar on Figures 6.13 and 6.14.

The positioning error with the location of the source and receivers in the physical modeling tank also manifests itself by the curving up of all horizons on the end of the lines in the 3-D volume as shown in Figures 6.13 to 6.14

6.4.4 Event flattening

To solve the problem of the horizon curvature at the end of each line in the 3-D volume an ITA program called "dejaggle" was run on the stacked data volume. This program determines a trace by trace time shift over a window which included both the KM and M events, to produce the maximum lateral correlation on a stacked line of data. The dejaggle program was run both in the inline and crossline direction. It was found that if dejaggle was run only in the inline direction then inline stacked lines would be flat but the crossline

FIG. 6.13 Crossline 39 from the full-offset 3-D seismic data volume. The events marked *KM*, *M* and *PB* are the reflections from the top of the model which represents the Mannville Formation, the top of the aluminum plate which represents the Mississippian Formation and point bar respectively. The trace spacing is 24.5 meters.
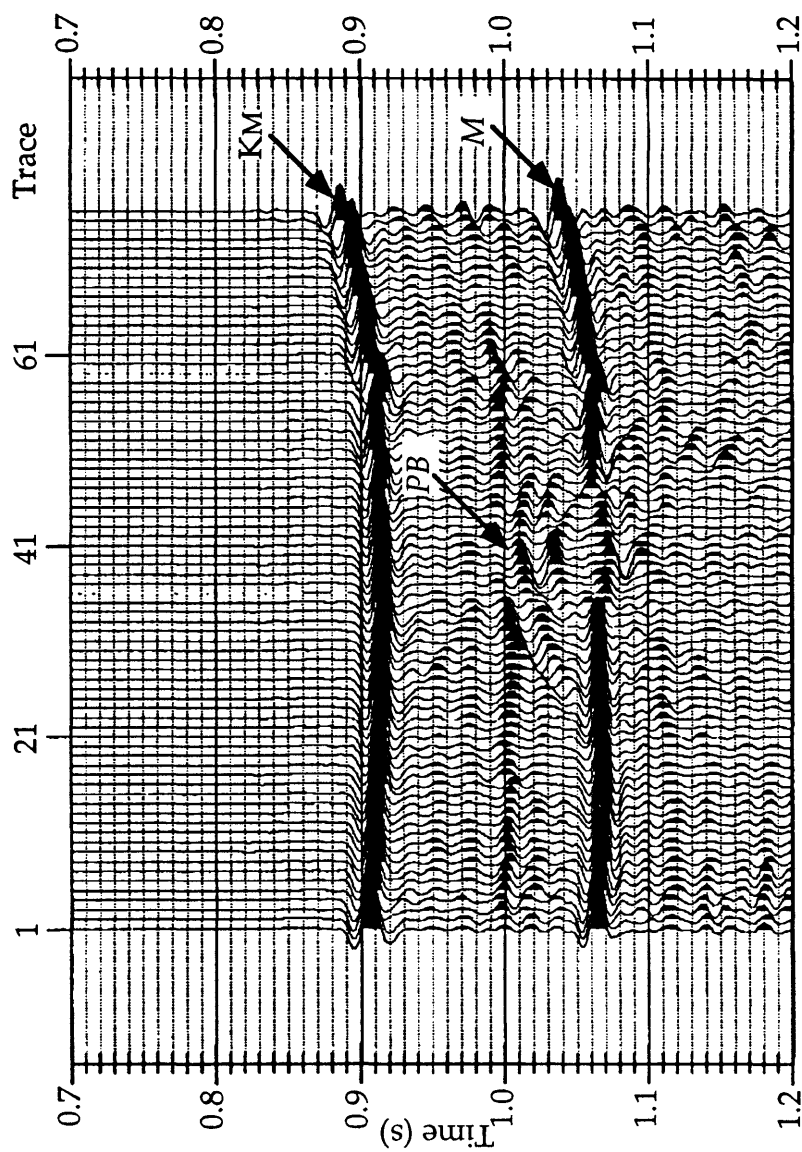
FIG. 6.14 Inline 49 from the full-offset 3-D seismic data volume. The events marked *KM*, *M* and *PB* are the reflections from the top of the model which represents the Mannville Formation, the top of the aluminum plate which represents the Mississippian Formation and the point bar respectively. The trace spacing is 24.5 meters.

stacked lines would still have horizon curvature at the end of each line. To implement the program, each line in the inline direction was input into the dejaggle program and a pilot trace was constructed for each line which is cross-correlated with each trace in that line to determine the required time shift for each trace on this line. Then this time shift was applied to each trace and the data were output and next inline stacked line was input into the program. This procedure continued until all inline stacked lines had been processed. The 3-D volume was then rotated 90 degrees and each crossline was processed and the required time shifts were calculated and applied to each trace on these lines. Then the 3-D volume was rotated back to the original line geometry. Figures 6.15 to 6.16 are the same crossline and inline as in Figure 6.13 to 6.14 but after the "dejaggle" process had been applied. The routine has removed most of the curvature of horizons on these stacked lines.

There is a pull-up of the Mississippian event beginning on trace 20 on Figure 6.15 and trace 21 on Figure 6.16 and this indicates the intersection of the line with the high-velocity channel shale. The Mississippian event is also pushed-down between traces 29 to 58 on Figure 6.15 and traces 34 to 46 on Figure 6.16 due to the low-velocity channel sand (point bar), indicated by the high amplitude trough marked *PB* at 1.2 s on traces 35 to 53 on Figure 6.15 and traces 37 to 41 on Figure 6.16. Inline 49 from the full-offset 3-D survey (Figure 6.16) was located in almost the same location over the physical model as the high resolution 2-D line (Figure 4.8) and inline 50 from the zero-offset 3-D survey (Figure 6.3). Figures 6.16 and 4.8 are similar. They both have a high quality image of the point bar and similarly image the topographic high in the Bantry shale but the 2-D line images the top of the point bar a bit better than the full-offset 3-D line and this may be due to the slightly higher fold coverage on the 2-D
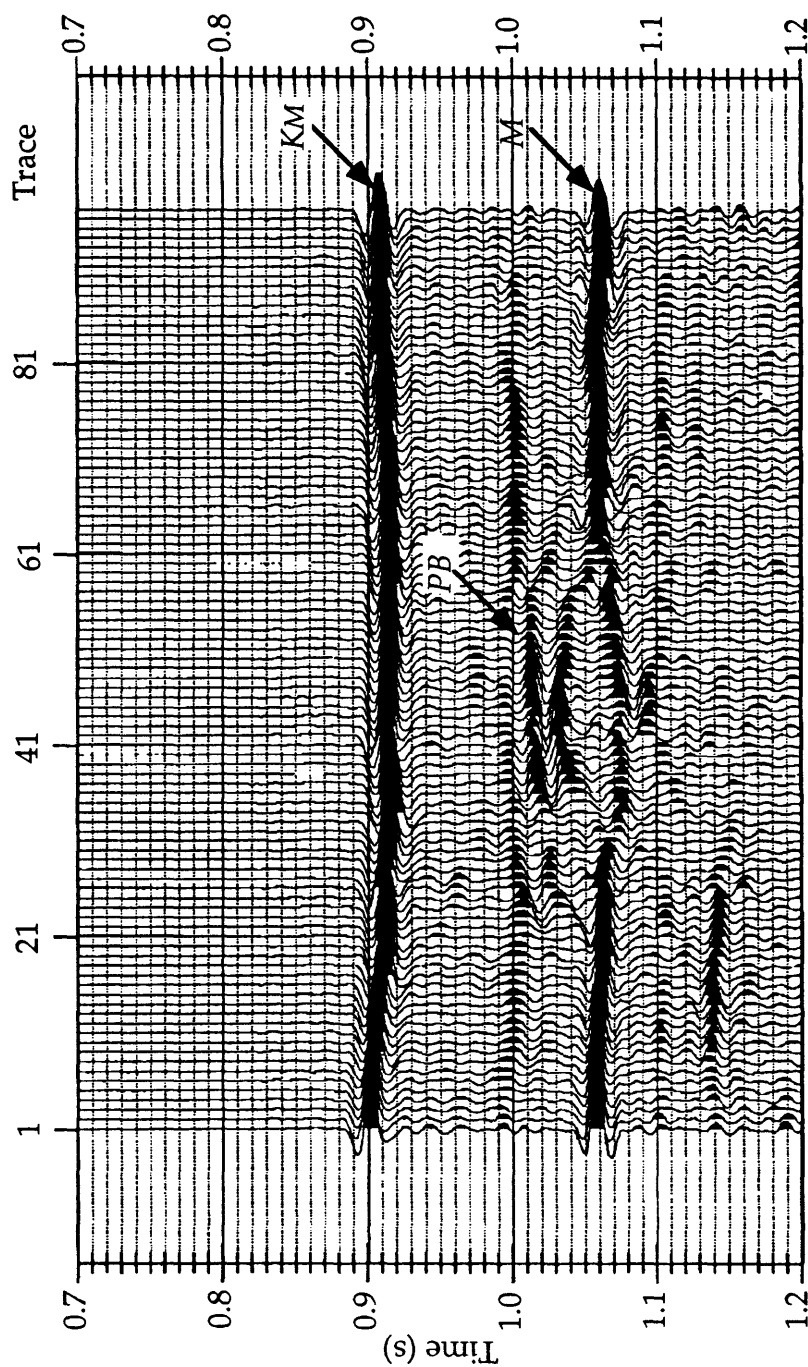
FIG. 6.15 Flattened crossline 39 from the full-offset 3-D seismic data volume. The events marked *KM*, *M* and *PB* are the reflections from the top of the model which represents the Mannville Formation, the top of the aluminum plate which represents the Mississippian Formation and the point bar respectively. The trace spacing is 24.5 meters.
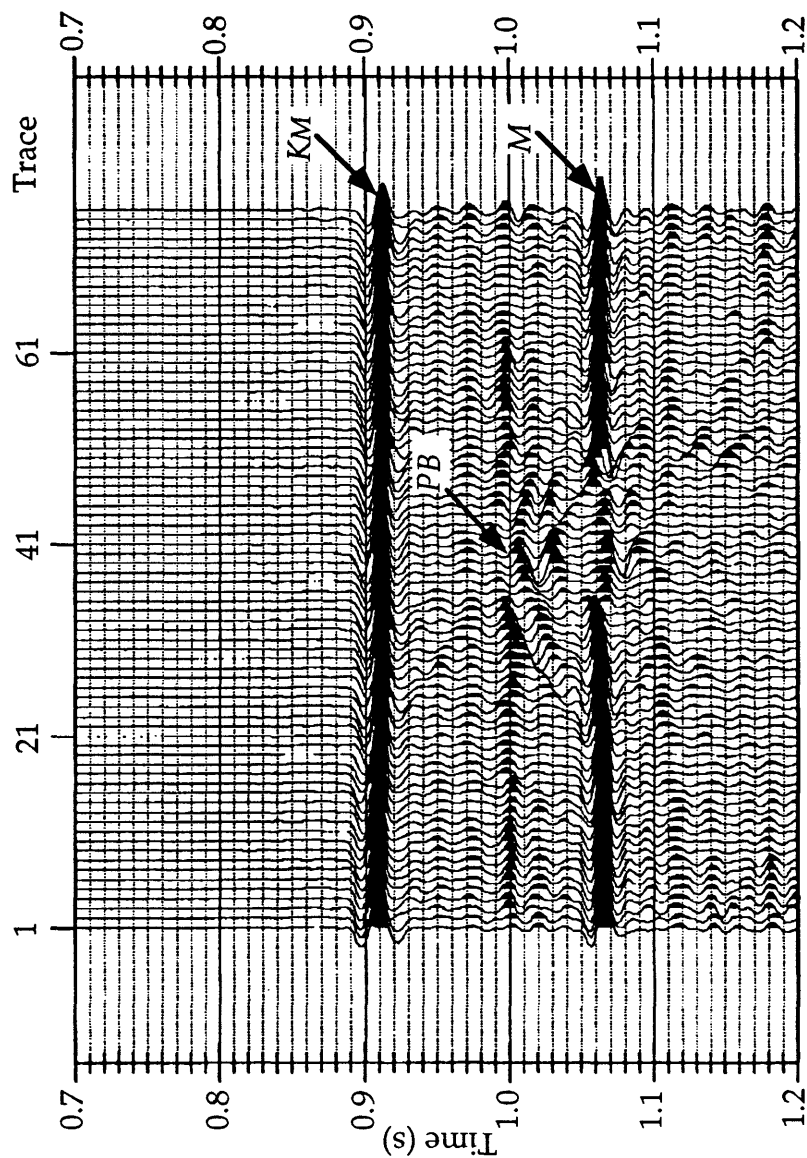
FIG. 6.16 Flattened inline 49 from the full-offset 3-D seismic data volume. The events marked *KM, M* and *PB* are the reflections from the top of the model which represents the Mannville Formation, the top of the aluminum plate which represents the Mississippian Formation and the point bar respectively. The trace spacing is 24.5 meters.

line (20 fold) than the 15 fold on the full-offset 3-D line. Inline 49 from the full-offset 3-D survey (Figure 6.16) produce a higher resolution image of the point bar and topographic high on the Bantry shale than inline 50 from the zero-offset 3-D survey (Figure 6.3). This improvement in the resolution of full-offset line over the zero-offset line is due to the increased fold and full 3-D imaging of the subsurface with the full-offset 3-D survey. Figure 6.16 produces a much better image of the Mississippian Formation under the point bar than either Figures 4.8 or 6.3 and this is due to the full 3-D imaging of the subsurface on the full-offset 3-D survey.

6.4.5 Fill-3D

The stacked data volume was filled to a cube data volume and the record format of the traces was changed in preparation for the 3-D post-stack migration.

6.4.6 Poststack migration

The flattened stacked data volume was migrated using a one-pass 3-D phase-shift migration to collapse diffractions and move dipping reflectors to their true subsurface position. The 3-D volume was migrated using one velocity function from the center of the point bar which should collapse any diffractions associated with the channel and point bar. In Figure 6.15 there is a diffraction which can be observed in the channel structure between 0.99 and 1.05 seconds on traces 50 to 71. There is also a diffraction (peak/trough/peak) on Figure 6.15 between 1.02 to 1.03 seconds on traces 23 to 30. These two diffractions on the migrated section are partially collapsed to form the dipping edges of the point bar (Figure 6.17). In Figure 6.16 there is a high amplitude diffraction between 1.005 and 1.05 second on traces 25 to 41 which has been partially collapsed on the migrated section (Figure 6.18). There is also a dipping event earlier than the
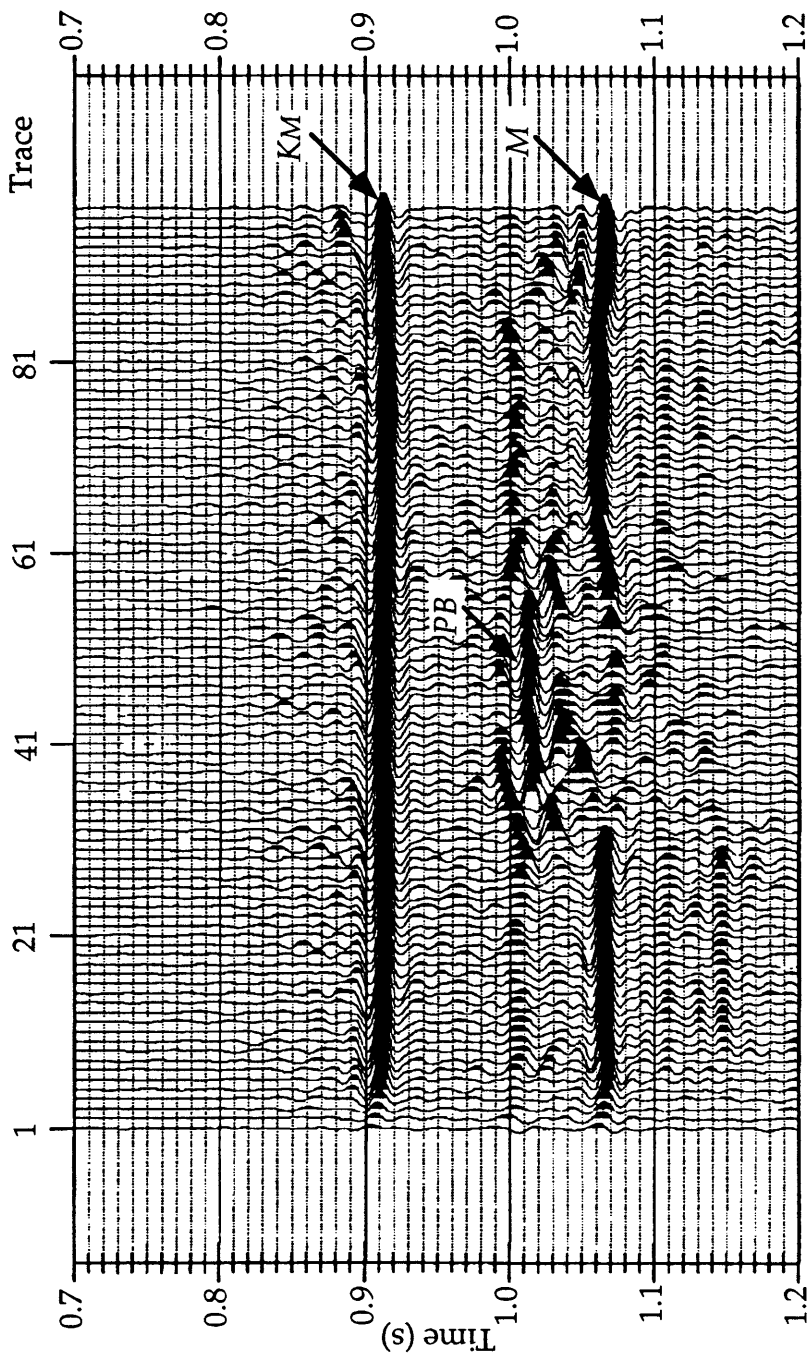
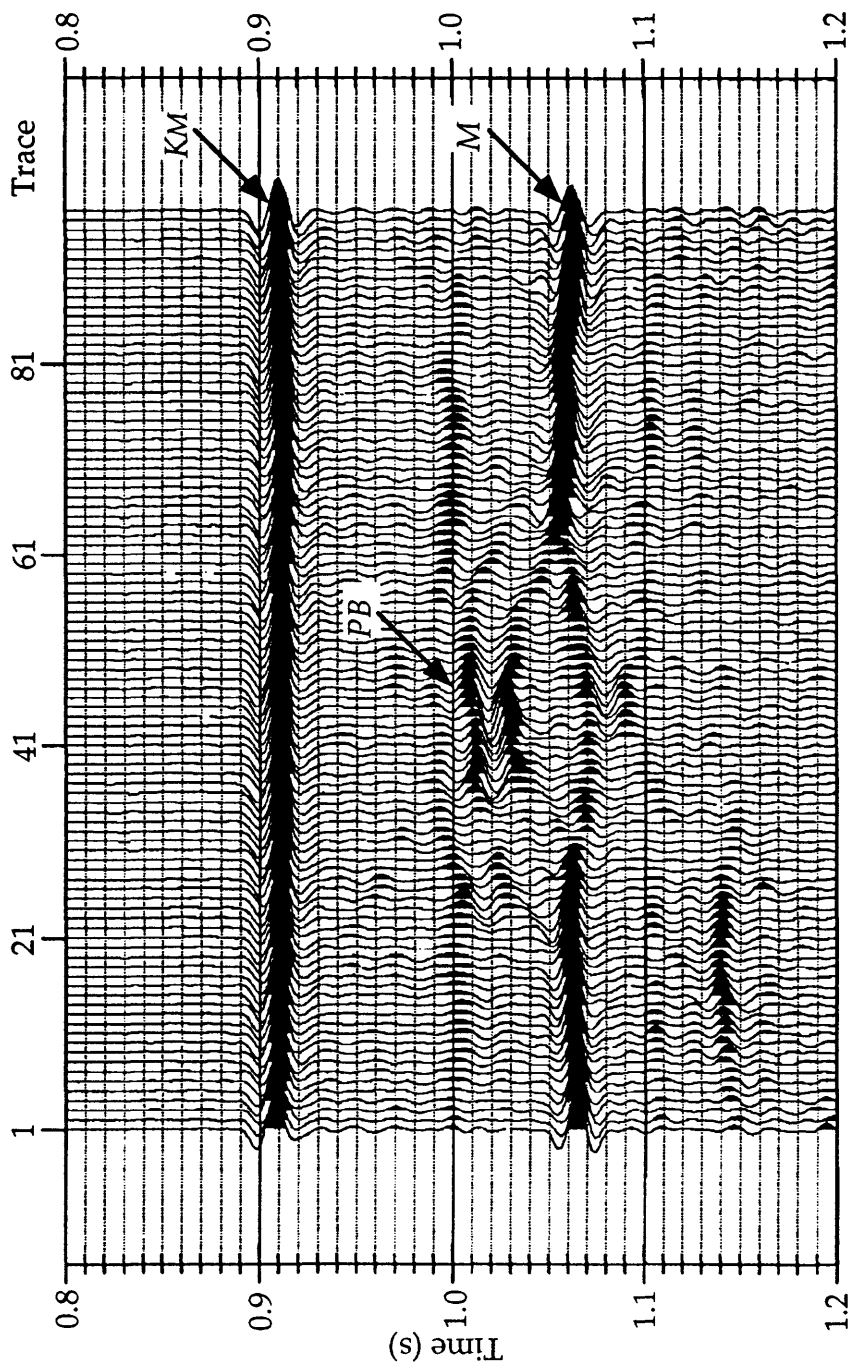FIG. 6.17 Migrated flattened crossline 39 from the full-offset 3-D seismic data volume. The events marked *KM*, *M* and *PB* are the reflections from the top of the model which represents the Mannville Formation, the top of the aluminum plate which represents the Mississippian Formation and point bar respectively. The trace spacing is 24.5 meters.
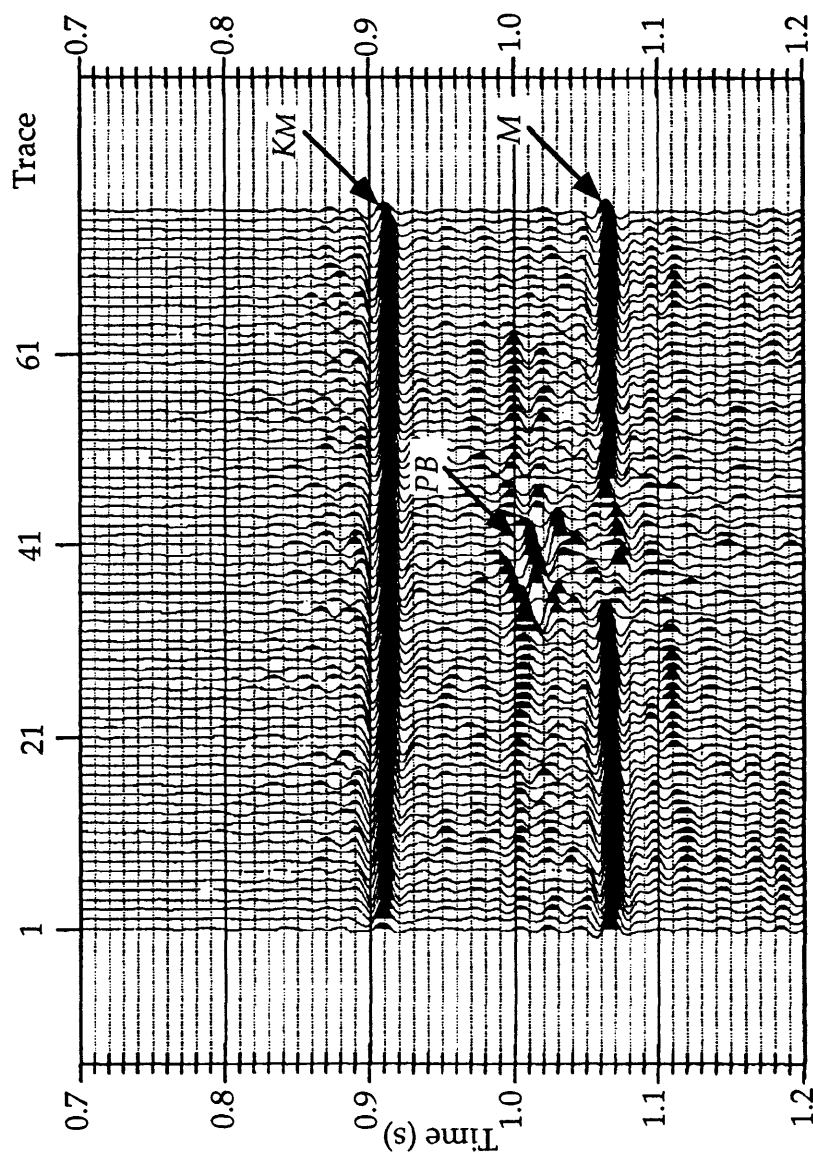
FIG. 6.18 Migrated flattened inline 49 from the full-offset 3-D seismic data volume. The events marked *KM*, *M* and *PB* are the reflections from the top of the model which represents the Mannville Formation, the top of the aluminum plate which represents the Mississippian Formation and the point bar respectively. The trace spacing is 24.5 meters.

diffraction on Figure 6.16 which moves up-dip to the right and steepens on the migrated section (Figure 6.18).

The migrated inline 49 (Figure 6.18) produces a lower resolution image of the top of the point bar compared to the migrated versions of the high resolution 2-D line (Figure 4.9-4.11). This lower resolution image may be due to the positioning errors with the sources and receivers which were occurring in the physical modeling tank and it could also be caused by the slightly lower fold (15 fold) on the 3-D line compared to the 20 fold on the high resolution 2-D line. The migrated 3-D line produces a better image of the Mississippian Formation under the point bar than the migrated versions of the high resolution 2-D line which must be caused by the better imaging of the subsurface with the 3-D than the 2-D. The migrated inline 49 from the full-offset 3-D volume images the point bar and the Mississippian Formation under the point bar better than inline 50 from the zero-offset 3-D survey (Figure 6.6). This improved imaging must be caused by the increased fold on the full-offset 3-D line as well as the 3-D imaging of the subsurface on the full-offset 3-D volume.

6.5 Interpretation

Figure 6.19a is a horizon map with the Mannville horizon interpreted on every fifth crossline of the phase-shift migrated 3-D volume. This figure indicates that the Mannville horizon is fairly flat (blue to purple color on this figure) except for about a 6 millisecond residual dejaggle error (red color on this figure) between inlines 1-15 and crosslines 1-25.

Figure 6.19b is a horizon map with the top of the Mississippian horizon interpreted on every fifth line of the phase-shift migrated 3-D volume in both the inline and crossline directions. There are hints of the channel structure on this figure indicated by the red, yellow and green colors versus the blue color on
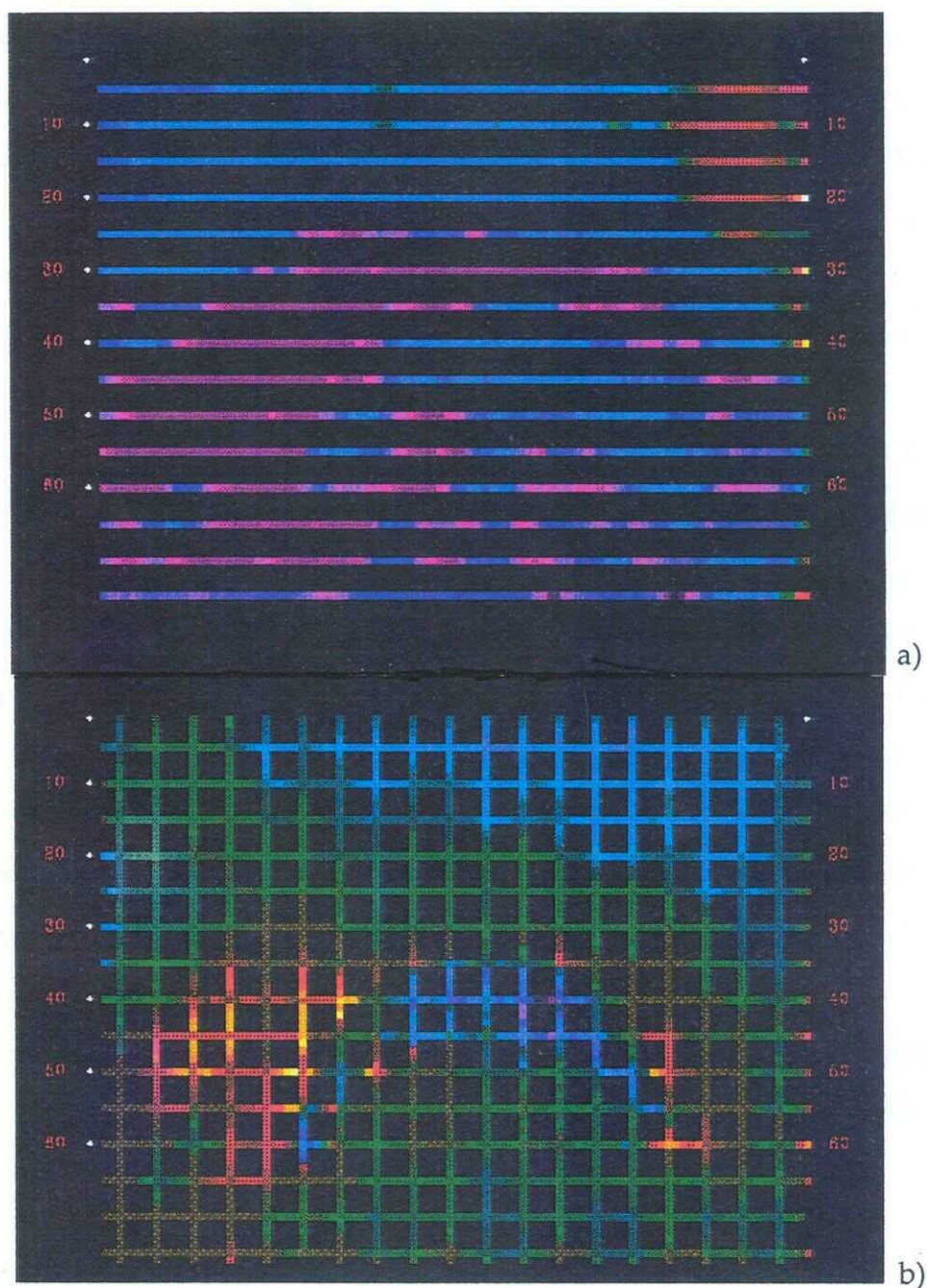
FIG. 6.19 Horizon maps from the full-offset 3-D survey indicating a) top of the Mannville Formation and b) top of the Mississippian Formation. Color scheme is yellow is the shallowest time and red, green, brown, blue and purple are succesively deeper times on each diagram.

crosslines 1-25 and inlines 1-75. This indicates a pull-up of 4 to 8 milliseconds caused by the high-velocity channel shale. The point and lateral bars are indicated by the push-down of the Mississippian horizon in the channel to the blue color for the point bar and green color for the lateral bar. This is a push-down of approximately 4 milliseconds from the surrounding channel shale caused by the low-velocity channel sand contained in the bar complexes.

A time slice at the 1.0 s level from the migrated full-offset 3-D volume is shown in Figure 6.20a. This slice is approximately at the Ostracod limestone interval in the physical model and it shows the high in the Bantry shale as well as the point and lateral bars. The topographic high on the Bantry shale as well as, and both point and lateral bars are indicated by a decrease in the amplitude of the reflection from these structures compared to the surrounding events. This decrease in reflection amplitude from the Bantry structure is caused by the defocusing of the reflected energy from the top of the dome structure. The decrease in reflection amplitude from the point and lateral bars is due to a small or negative reflection coefficient for the bars compared to the surrounding Ostracod limestone.

Figure 6.20b is a time slice at the 1.004 s level from the migrated full-offset 3-D data set. This time slice is still in the Ostracod interval but it is later than the previous slice. The shale-filled channel and splay as well as the point and lateral bars are visible, the shale-filled channel and splay are indicated by a strong positive reflection from these features while point and lateral bars are indicated by a strong negative reflection from the bars. These variations in amplitude of the reflections are caused by the variations in the reflection coefficients of the different materials which make up these structures.

A time slice at 1.016 s level from the migrated full-offset 3-D is shown in
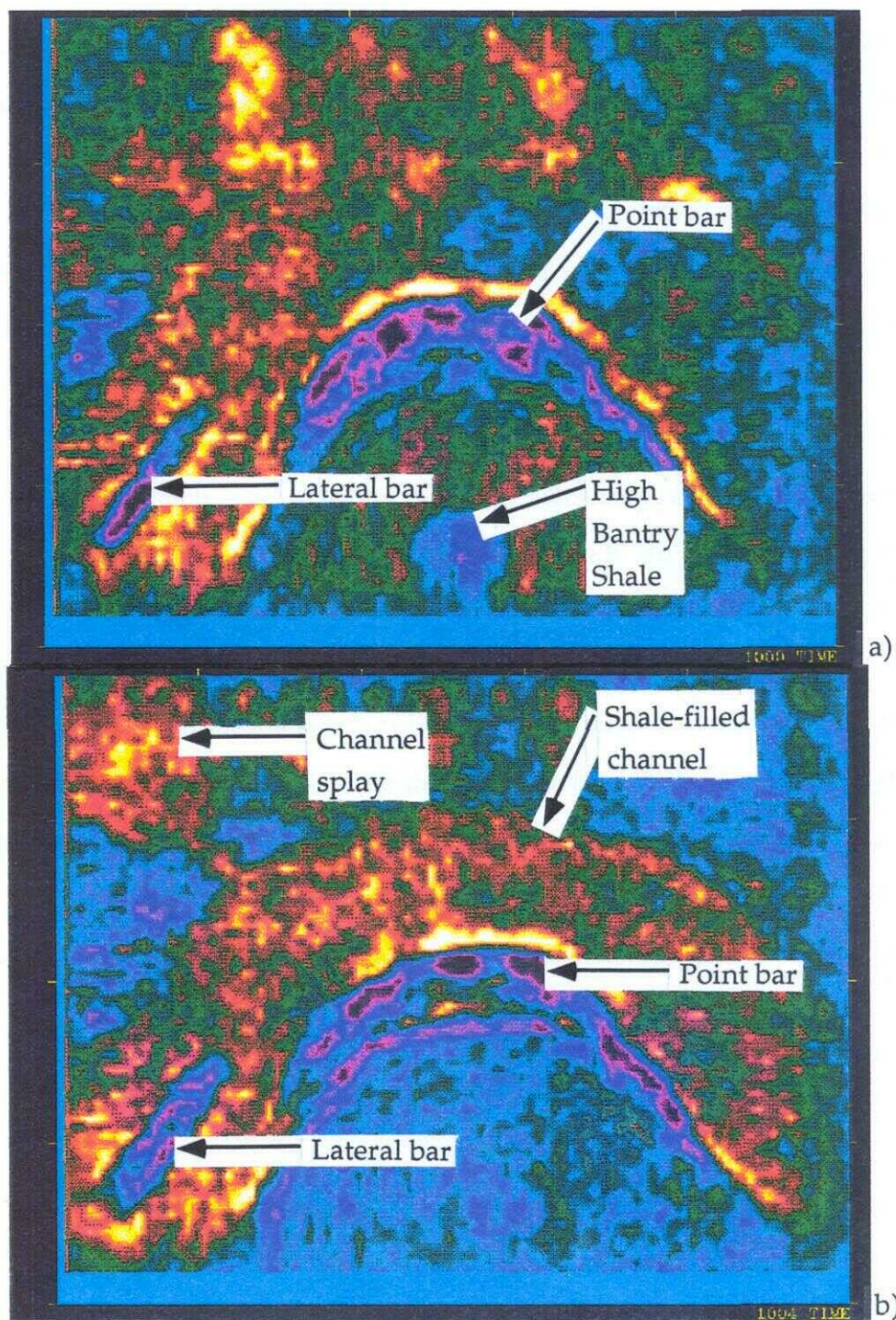
FIG. 6.20 Time slices from the full-offset 3-D survey at a) 1000 ms and b) 1004 ms indicating the topographic high in the Bantry Shale, point and lateral bars, shale-filled channel and splay. Color scheme is yellow is largest positive amplitude and amplitudes decline through red, green, blue, purple and black which is the largest negative amplitude on each diagram.

Figure 6.21a. This slice is at the Bantry shale level on the physical model and it clearly shows the variations in the amplitude of the reflections from the shale-filled channel and splay, point and lateral bars and surrounding Bantry shale. The shale-filled channel and splay produce a strong negative amplitude reflection compared to the surrounding Bantry shale whereas the lateral bar has a slightly negative amplitude reflection and the reflection from the point bar varies widely from a strong positive to a strong negative amplitude.

Figure 6.21b is a time slice from the migrated full-offset 3-D data set at the 1.072 s level, which is close to the top of the Mississippian event on the physical model. This figure shows an amplitude anomaly on the Mississippian event caused by the velocity anomaly from the overlying channel shale and channel sand. The lower velocity channel sand and higher velocity channel shale compared to the material surrounding the channel event produces a push-down and pull-up of Mississippian events below each of these materials respectively. These velocity anomalies respectively increase and decrease the arrival time of the reflection from the top of the Mississippian event and this produces the modulation in amplitude of the Mississippian reflection shown in this figure.

122
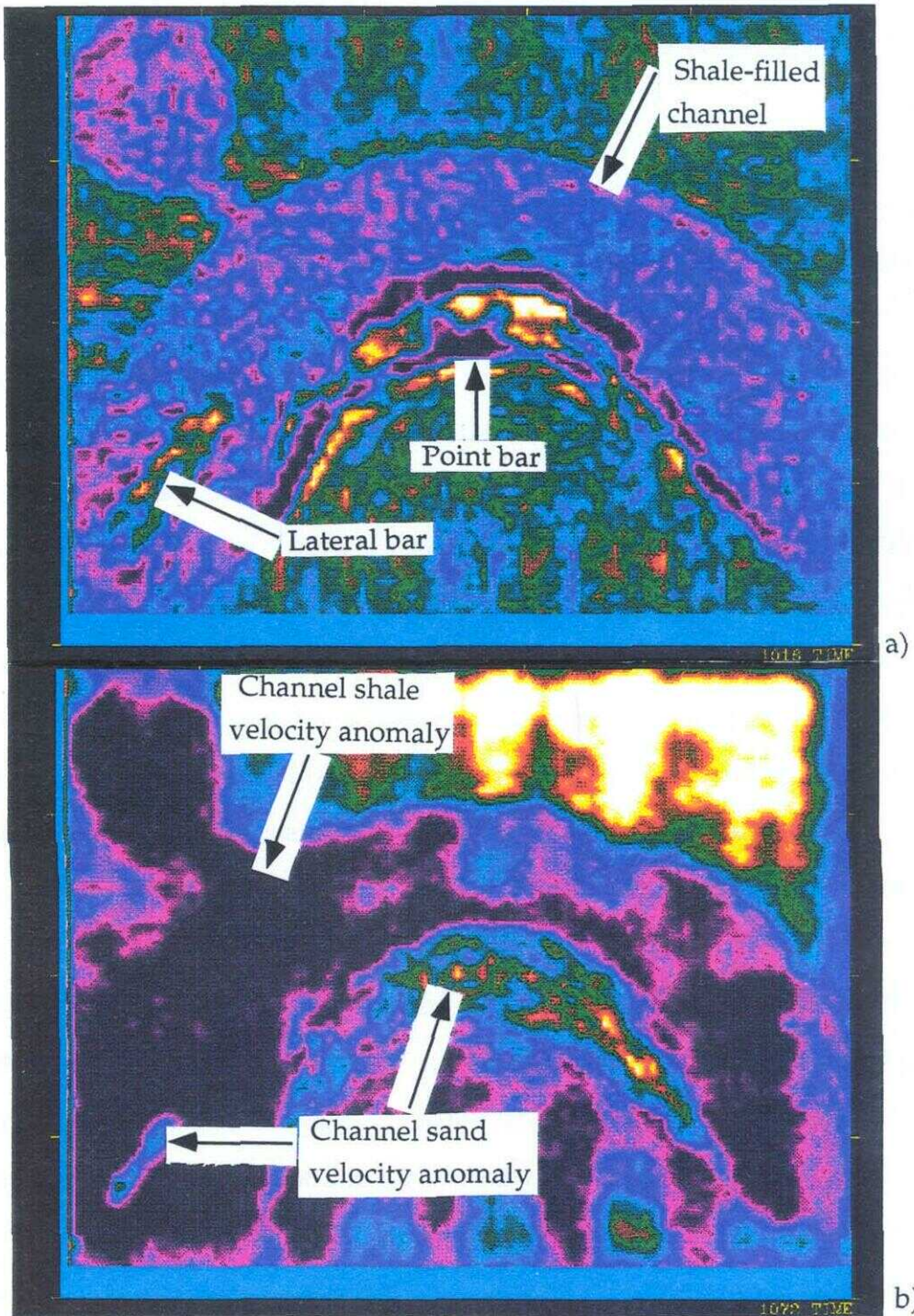
FIG. 6.21 Time slices from the full-offset 3-D survey at a) 1016 ms and b) 1072 ms indicating shale-filled channel and splay, point and lateral bars and velocity anomaly from the overlying channel sand and shale. Color scheme is white is largest positive amplitude and amplitudes decline through yellow, red, green, blue, purple and black which is the largest negative amplitude on each diagram.

CHAPTER 7 DISCUSSION AND CONCLUSIONS

7.1 Discussion

During the construction of the physical model a problem developed in that there is a very limited range of acoustic interval velocities available for modeling materials. This is especially true for modeling materials which have an acoustic interval velocity between 3000 to 4000 m/s. To produce materials which have an acoustic interval velocity in this range required the use of composite materials such as epoxy resins and plaster of Paris with the addition of different proportions of various sized glass beads. The use of composite materials in the physical model construction produced numerous problems. One problem that occurred was that there can be inhomogeneities in the composite material caused by incomplete mixing of the components of the composite material or by settling out of the components of the composite material. A second problem occurred when these composite materials were poured onto the physical model. To pour the composite material onto the physical model required that dams be placed around the boundary of the physical model, then when the composite material was poured onto the model it formed a meniscus against the dam and this made it difficult to determine the actual thickness of the composite. A third problem which can occur with composite materials is that most use a chemical reaction which produces heat to harden the material. If the composite material is poured in a thick layer this heat builds up quickly and can crack or craze the composite material and allow air to enter the material and produce an inhomogeneity in the material. This can be compensated for by reducing the amount of hardener in the composite material but there is a risk that the composite material may not harden properly.

The first two problems with composite materials may have lead to small errors in interval velocities and rms velocities for composite materials. The interval velocity of a composite is calculated using a sample of the composite material. If this sample is not representative of the composite material then an erroneous interval velocity is obtained for that layer in the model. The rms velocity is calculated using Dix equation and if the interval velocity or thickness of the layers is incorrect this will produce an erroneous rms velocity. This type of error is evident from the data in Table 4.2 where the calculated rms velocity and processing stacking velocity from velocity analysis were compared for a specific CMP. In this table there is about a 10 % difference between stacking velocity and calculated rms velocity.

In chapter 4, a high resolution 2-D line was acquired along a line perpendicular to and through the center of the point bar. This line was acquired to obtain a high quality seismic signature of the channel and point bar which could be later used to help with the interpretation of the 3-D datasets. Also these data were used to evaluate a theory of Noah et al., (1992) that sideswipe energy from out-of-plane parts of the sand body affects the amplitudes of events on the 2-D seismic sections and this makes it difficult to determine variation in the thickness of the sand body.

There is no variation in amplitude of the seismic response on the high resolution 2-D data as the point bar thickness varies from 0-30 m. The Fresnel zone radius is defined by the following equation.

$$Fr = \left(\frac{V}{2}\right)\left(\frac{t}{f}\right)^{\frac{1}{2}}$$
7.1

Fr = Fresnel radius in meters
V = seismic velocity through material
t = two way time to top of the reflector
f = dominant frequency of the source wavelet

For the point bar in the physical model the Fresnel radius is:

$$Fr = \left(\frac{3045}{2}\right)\left(\frac{1.0}{50}\right)^{\frac{1}{2}} \qquad\qquad 7.2$$

$$= 215 \text{ m}$$

Therefore any sand bodies within 215 m of the 2-D line will affect the amplitude of the seismic response.

Time slices from both the zero-offset and full-offset 3-D survey of the physical model were chosen to coincide at the level of the point bar sand body but do not show any significant amplitude variations with respect to sand body thickness. This lack of variation may be a result of the single-fold coverage in the zero-offset 3-D and a result of the poor resolution in the full-offset 3-D survey. The full-offset 3-D survey had a problem with positioning of the source and receivers in the physical modeling tank. This positioning error scatters the traces randomly around in the CMP bin instead of grouping the traces in the center of the CMP bin and this tended to lower the resolution of the full offset 3-D offset data survey. The lower resolution would tend to smear the seismic amplitude response thereby producing an average seismic amplitude response for all events in the model.

In chapter 5, it was stated that the prime objective of any 3-D survey design is to produce an interpretable seismic volume. This objective is partially fulfilled by designing a 3-D survey such that the minimum fold to be able to image the target adequately is always obtained and fold is increased in poor signal to noise ratio areas. Other factors which affect the design of a 3-D survey include: fold distribution, offset distribution and azimuth distribution. The fold distribution in each bin will affect signal to noise ratio and ability to determine velocity distribution for proper normal move out correction. Regular offset distribution within bins is desired in order to determine a stable velocity field, to

have coherent noise cancellation in the stack and to attenuate multiples. A wide range of offsets in each bin is necessary because short offsets are required for shallow exploration targets and shallow velocity determination in refraction analysis while long offsets are required for robust stacking velocities and deeper refractor velocities for long-wavelength statics analysis. A uniform distribution of source receiver azimuths is required to provide robust refraction statics corrections and to help detect azimuth-dependent variations from dipping horizons.

Various 3-D survey designs such as: straight-line, tight straight-line, swath, and brick method of acquisition were examined to determine the advantages and limitations of each design. The fold, offset and azimuth distribution for the straight-line and tight straight-line method of acquisition were examined over a near (0-500m), mid (500-1000m) and far offset (1000-1500m) range while the brick method of acquisition, was examined over the full-offset range (0-1500m) to determine the distribution of each of these parameters over the various offset ranges.

The straight-line method of 3-D acquisition has the advantages that it is easy to layout in the field, has straight-forward roll-along of the receiver patch and geometry for processing is simple. Since it is easy to layout in the field this reduces layout time and therefore lowers the acquisition cost. A straight-forward roll-along is only an advantage for non-telemetry systems, otherwise patch movement is not a concern. The simple geometry makes processing easy and cuts down on geometry errors during processing of the data. A disadvantage of the straight-line method is that the minimum offset in the survey is quite large which may cause problems imaging shallow exploration targets and determining

shallow refractor velocity so reduced source/receiver line spacing may be required, which increases acquisition cost.

The offset distribution for the straight-line method is unevenly sampled in the bins for the near and far-offset range but becomes more uniformly sampled for the mid-offset range. The azimuth distribution follows the same pattern as offset distribution with poor azimuth sampling for the near and far-offset and more uniform distribution at mid offsets. Fold distribution also has a low fold distribution for the near and far-offset range and a high fold distribution for the mid-offset range.

A variation on the straight-line method of 3-D acquisition is the tight straight-line method which uses the same receiver patch but decreases source line and source spacing as well as receiver line and receiver spacing. This method produces a more uniform spatial sampling than the conventional straight-line method and also has a smaller minimum offset because of the dense source and receiver line spacing. Its disadvantage is that acquisition costs significantly more than for the conventional straight-line method because of all the extra source locations and extra equipment which must be laid out in the field per square kilometer.

A second variation on the straight-line method is the swath acquisition method. It provides a field operational advantage over the straight-line survey in that there is a minimum of equipment movement to acquire the data. This decreases acquisition time and therefore decreases acquisition cost. A disadvantage of this method is the poor distribution of offset and azimuths in each bin. The poor offset distribution could make stacking velocity determination difficult and may provide poor coherent noise cancellation in the stack. An uneven azimuth distribution could produce poor coupling between

receivers and will make it difficult to detect azimuth dependent variations such as anisotropy.

The brick acquisition method has an advantage over the straight-line method in that the largest minimum offset in the survey is equal to receiver line interval verses the diagonal of the distance between adjacent source and receiver lines for the straight-line method. This allows a wider spacing between receiver lines to obtain the same minimum offset as the straight-line method and this lowers acquisition time and therefore lowers acquisition cost. A second advantage of this method is that it provides reasonable offset and azimuth distribution in the bins which makes stacking velocity determination easier, provides better noise cancellation in the stack and makes it easier to detect azimuth dependent variations. A disadvantage of this method is that surface access must be very open to allow specific placement of sources and receivers which limits the use of this survey method.

The offset distribution, azimuth distribution and fold distribution for the brick method is lower than the conventional straight-line method for the full-offset range. This random offset and azimuth distribution will make it more difficult to determine stacking velocity and could create problems with static coupling between receivers. The lower fold distribution will affect signal to noise ratio and could make it difficult to determine proper velocity for NMO correction.

In designing a 3-D straight-line survey for the physical modeling tank it was found that two parameters control fold distribution. If the number of receivers per line in the receiver patch multiplied by the receiver station spacing and divided by source line spacing was not an even integer then there would be low bands of fold coverage in the survey. It was also found that if the number of

receiver lines per patch multiplied by the receiver line spacing and divided by the E-W patch move (source spacing) was not equal to an even integer then there would be low bands of different fold coverage in the survey. If both these conditions are met then the receiver patch rolls along in such a way that there is an exact overlap in both directions as the receiver patch moves through the survey.

During the processing of the 3-D data set (Chapter 6) it was found that the ITA 3-D processing software had numerous deficiencies, the first is the 3-D geometry program. This program is very awkward to use and documentation is very poor so the geometry was inserted into the trace headers using the geometry program then the utilities program was used to fix numerous errors in the values which were placed into the trace headers by the 3-D geometry program. It was also found that the 3-D reflection statics program supplied to the university does not work so the reflection statics were run at another ITA site. The 3-D velocity analysis forces the user to pick 5 sets of time-velocity pairs for each velocity analysis location and the time picks must be the same on all 5 sets of time-velocity pairs. Therefore it is not possible to insert a new time pick on any of the different azimuth time-velocity picks.

A problem with the physical modeling tank acquisition system was encountered during the processing of the full-offset 3-D survey. This problem was noticed during the velocity analysis when all of the horizons at each velocity analysis location appeared to have a short wavelength statics problem. There should be no statics problem in the data as this is a tank data set so it was assumed that the statics problem was caused by a positioning error in the source and receiver locations in the physical modeling tank. This positioning error could be created if the source and receiver beams in the physical modeling tank

were not orthogonal. If this was the case then as the beams moved they did not move to the correct location and this positioning error would tend to increase through subsequent movement of the source and receiver beams in the physical modeling tank. This possible positioning error of the source and receivers in the physical modeling tank manifests itself as a curling up of all horizons on the ends of all the lines in the full-offset 3-D volume. To solve this problem an ITA program which determines the trace by trace time shifts over a window which included both the *KM* and *M* events on the stack section was applied to the stacked data to determine the maximum lateral correlation on a stacked line of data. This "dejaggle" program was implemented in both the inline and cross-line direction to remove the horizon curvature at the end of each line.

7.2 Conclusions

1) 3-D acquisition algorithms were developed for University of Calgary's physical modeling tank.

2) Analysis of 2-D data confirms Noah et al., (1992) theory that sideswipe energy from out-of-plane sand bodies affect amplitude of events on 2-D seismic data.

3) The lack of amplitude variation on two 3-D surveys may be the result of single-fold coverage in the zero-offset 3-D survey and a result of the poor resolution in the full-offset 3-D survey caused by the scattering of traces in each CMP bin.

4) There are many deficiencies in the ITA 3-D processing software which impeded the progress of the processing of the 3-D surveys.

5) Factors which affect 3-D design significantly were found to be fold, offset, and azimuth distribution.

6) Conventional straight-line 3-D acquisition method produces low distribution of fold, offset and azimuth distribution for near and far-offset range and more uniform distribution at the mid-offset range.

7) Dense straight-line method of 3-D acquisition produces more uniform distribution of fold, offset and azimuth distribution over all offset ranges compared to the conventional straight-line method.

8) Brick method of 3-D acquisition has a lower offset, azimuth and fold distribution for the full-offset (0-1500m) range compared to the conventional straight-line method.

9) The 2-D and 3-D survey were able to produce high quality images of the point bar, lateral bar and shale-filled channel and channel splay.

10) All three surveys (2-D, zero-offset 3-D and full-offset 3-D) displayed the velocity anomaly on the Mississippian event caused by the overlying channel shale. The full-offset 3-D data was able to image the velocity pull-down on the Mississippian event caused by the overlying channel sand.

7.3 Future Work

Future work for this study should include acquiring more offset 3-D surveys over the physical model using the various acquisition geometries. These surveys would be processed to determine if the variations and limitations noted in each of these acquisition geometries affect the seismic resolution of the seismic data. Special processing of these data sets would include producing various limited offset range stacks of the 3-D volume to try to highlight the variations in offset, azimuth and fold distribution that occurs on each of these different acquisition geometries.

REFERENCES

Buckingham, E., 1914, On physically similar systems: illustration of the use of dimensional equations: Physical Review, v. 4, p. 345-376.

Bukovics, C., and Nooteboom, J. J., 1990, Combining techniques in integrated 3D land, shallow water and deep channel seismic acquisition: First Break, v. 3, p. 375-382.

Cheadle, S. P., 1988, Applications of physical modelling and localized slant stacking to a seismic study of subsea permafrost: Ph.D. Thesis, University of Calgary, Alberta.

Cheadle, S. P., Bertram, M. B., and Lawton, D. C., 1985, Development of a physical seismic modelling system, University of Calgary: Current Research, Part A, Geological Survey of Canada, paper 85-1A, p. 499-504.

Crews, G. A., Musser, J. A., and Bremner, D. L., 1989, Applications of new recording systems to 3-D designs: 59th Ann. Internat. Mtg., Soc. Expl. Geophy., Expanded Abstracts, p. 624-627..

Energy Resources Conservation Board, 1989, Alberta reserves of crude oil, oil sands, gas, natural gas liquids, and sulfur: Energy Resources Conservation Board Calgary, Alberta, statistical series 88-18, variously paginated.

Evans, J. F., Hadley, C. F., and Silverman, D., 1953, A three dimensional seismic wave model with both electrical and visual observation of waves: Geophysics, v. 43, p. 220-236.

Farshori, M. Z., and Hopkins, J. C., 1989, Sedimentology and petroleum geology of fluvial and shoreline deposits of the Lower Cretaceous Sunburst Sandstone Member, Mannville Group, southeastern Alberta: Bulletin of Canadian Petroleum Geology, v. 37, p. 371-388.

Farshori, M. Z., 1983, Glauconitic sandstone, Countess Field "H" pool, southern Alberta, in McLean, J. R., and Reinson, G. E., (editors), Sedimentology of Selected Mesozic Clastic Sequences: Canadian Society of Petroleum Geologists, Corexpo 1983, p. 27-42.

French, W. S., 1974, Two-dimensional and three-dimensional migration of model-experiment reflection profiles: Geophysics, v. 39, p. 265-277.

Galbraith, M., 1994, 3-D seismic design by computer: CSEG Recorder, p. 4-8.

Glaister, R. P., 1959, Lower Cretaceous of southern Alberta and adjoining areas: AAPG Bulletin, v. 43, p. 590-640.

Hawthorne, R., and Webster, R., 1989, 3-D seismic, in Anderson, N. L., Hills, L. V., and Cederwall, D. A., (editors), CSEG/CSPG Geophysical Atlas of Western Canadian Hydrocarbon Pools: Can. Soc. Explor. Geophys./Can. Soc. Pet. Geol., p. 311-317.

Hilterman, F. J., 1970, Three dimensional seismic modeling: Geophysics, v. 35, p. 1020-1037.

Hopkins, J. C., Wood, J. M., and Krause, F. F., 1991, Waterflood response of reservoirs in an estuarine valley fill: Upper Mannville G, U, pools, Little Bow Field, Alberta, Canada: AAPG Bulletin, v. 75 p. 1064-1088.

Hopkins, J. C., Hermanson, S. W., and Lawton, D. C., 1982, Morphology of channels and channel sand bodies in the Glauconite Sandstone Member (Upper Mannville), Little Bow area, Alberta: Bulletin of Canadian Petroleum Geology, v. 30, p. 274-285.

Hospers, J., 1985, Sideswipe reflections and other external and internal reflections from salt plugs in the Norwegian-Danish basin: Geophysical Prospecting, v. 33, p. 53-71.

Howes, E. T., Tejada-Flores, L. H., and Randolph, L., 1953, Seismic model study: Journal Acoustic Society of America, v. 25, p. 915-921.

Jackson, P. C., 1984, Paleogeography of the Lower Cretaceous Mannville Group of western Canada, in Masters, J. A., (editor), Elmworth Case Study of a Deep Basin Gas Field: AAPG Memoir 38, p. 49-77.

Krebes, E. S., 1989, Geophysical data processing: Geophysics 557 Course Notes

Lansley, R. M., 1993, SEG 3-D seismic acquisition course: taught at 63th Ann. Internat. Mtg., Soc. Expl. Geophy.

Levin, F. K., and Hibbard, H. C., 1955, Three-dimensional seismic model studies: Geophysics, v. 20, p. 19-32.

May, B. T., and Hron, F., 1978, Synthetic seismic sections of typical petroleum traps: Geophysics, v. 43, p. 1119-1147.

McDonald, J. A., Gardner, G. H. F., and Hilterman, F. J., (editors), 1983, Seismic Studies in Physical Modeling: IHRDC, Boston, MA.

Nazar, B., 1990, 2-D and 3-D migrations applied to a 3-D channel model dataset: Geophysics 701 project.

Newman, P., 1980, 3-D acoustic model experiments: paper presented at 50th Ann. Internat. Mtg., Soc. Expl. Geophy.

Noah, J. T., Hofland, G. S., and Lemke, K., 1992, Seismic interpretation of meander channel point-bar deposits using realistic seismic modeling techniques: Geophysics: The Leading Edge, v. 11, p. 13-18.

Northwood, T. D., and Anderson, D. V., 1953, Model seismology: Bulletin Seismological Society of America, v. 43, p. 239-245.

O'Brien, P. N. S., 1955, Model seismology-the critical refraction of elastic waves: Geophysics, v. 20, p. 227-242.

Pant, D. R., Greenhalgh, S. A., and Watson, S., 1988, Seismic reflection scale model facility: Exploration Geophysics, v. 19, p. 499-512.

Rana, A. I., and Sekharan, K. K., 1990, New developments in physical modeling at the acoustic lab: 60th Ann. Internat. Mtg., Soc. Expl. Geophy., Expanded Abstracts, p. 1066-1068.

Ritchie, W., 1991, Onshore 3-D acquisition techniques: a retrospective: 61th Ann. Internat. Mtg., Soc. Expl. Geophy., Expanded Abstracts, p. 750-752. Geologic Structures: Society of Exploration Geophysicists, Tulsa, OK.

Robinson, E. A., and Treitel, S., 1980, Geophysical Signal Analysis: Prentice-Hall, Englewood Cliffs, NJ.

Van Wagoner, J. C., Mitchum, R. M. J., Posamentier, H. W., and Vail, P. R., 1987, Part 2: key definitions of sequence stratigraphy, in Bally, A. W., (editor), Atlas of Seismic Stratigraphy, Volume 1: AAPG studies in Geology 27, 125 p.

Walton, G. G., 1972, Three dimensional seismic method: Geophysics, v. 37, p. 417-430.

Wood, J. M., 1990, Sequence stratigraphy, sedmentology and petroleum geology of the Glauconitic Member and adjacent strata, Lower Cretaceous Mannville Group, southern Alberta: Ph.D. Thesis, University of Calgary, Alberta.

Wood, J. M., and Hopkins, J. C., 1989, Reservoir sandstone bodies in estuarine valley fill: Lower Cretaceous Glauconite Member, Little Bow Field, Alberta, Canada: AAPG Bulletin, v. 73 p. 1361-1382.

Yilmaz, O., 1987, Seismic Data Processing: Society of Exploration Geophysicists, Tulsa, OK.

Zimmerman, L. J., 1991, Modeling the seismic response of geologic structures with physical models, in Fagin, S. W., (editor), Seismic Modeling of Geologic Structures: Society of Exploration Geophysicists, Tulsa, OK.

APPENDIX A

In chapter 5, a comparison was done of offset, azimuth and fold distribution between the brick method of acquisition and the conventional straight-line method of 3-D acquisition over the full-offset range (0-1500m). Figures A.1 through A.3 are the offset, azimuth and fold distribution for the conventional straight-line method over the full-offset range used in this comparison.

The offset, azimuth and fold distribution was examined for the brick acquisition method using the same survey size, source and receiver line spacing, source and receiver spacing and receiver patch size as was used in the conventional straight-line method (chapter 5). Figure A.4 defines the offset distribution for near 0-500 m offset range. The offset distribution is highly variable over this area with more uniform offset distributions along source lines where there are no active sources. There are also strips of more uniform offset distribution along receiver lines. The largest near offset in the center bin of the box (A in Figure A.4) formed by the adjacent source and receiver lines is 200 m. In general offset distribution is much more variable then the conventional straight-line acquisition method over this offset range. Azimuth distribution for the near-offset range (Figure A.5) indicates a sparseness of azimuth in bins in the center of the box. The offset distribution for the mid and far offsets are described in Figures A.6 and A.7 respectively. The offset distribution in these figures is fairly uniform over the whole area. On the mid-offset diagram, Figure A.6 there are bins which contain only far offsets along source lines at the end of a zone of active sources. The next bin along the source line after the end zone of active sources will always contain only far offset traces (B zones on Figure A.6). The bin in the center of the box (A on Figure A.6) contains only 2 offsets and there is
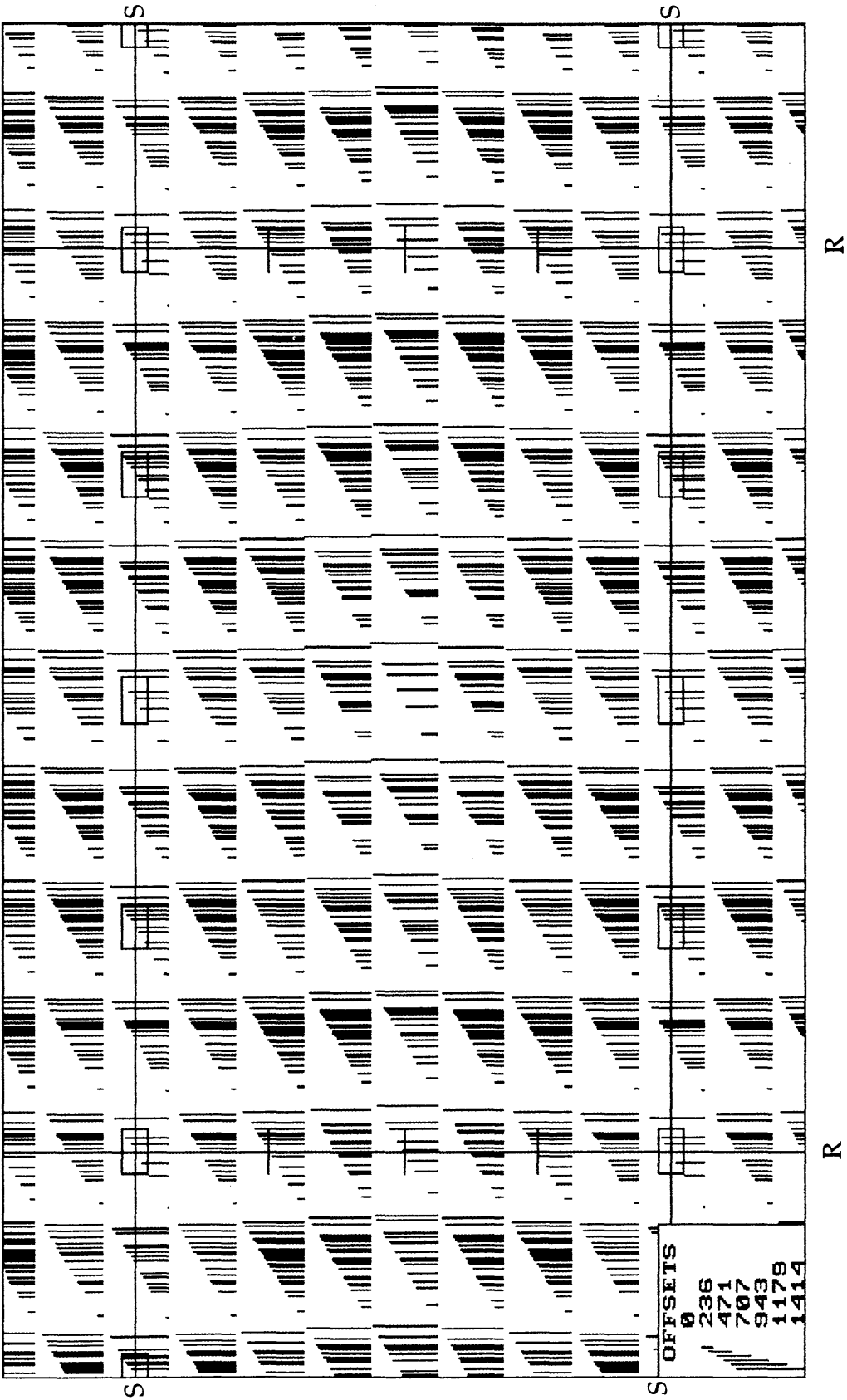
136

FIG. A.1 Offset distribution for the full-offset range for the conventional straight-line 3-D acquisition method.
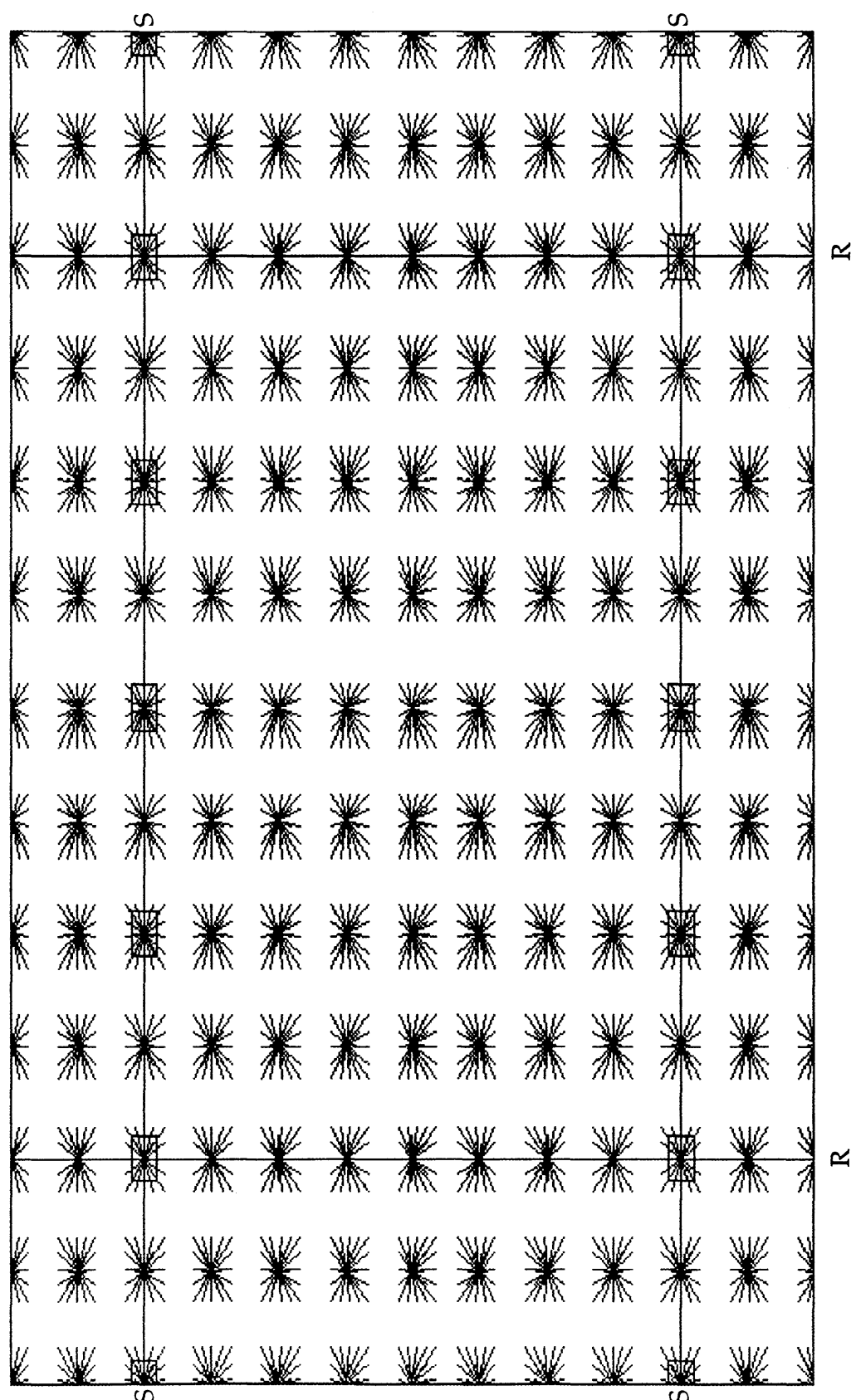
FIG. A.2 Azimuth distribution for the full-offset range for the conventional straight-line 3-D acquisition method.
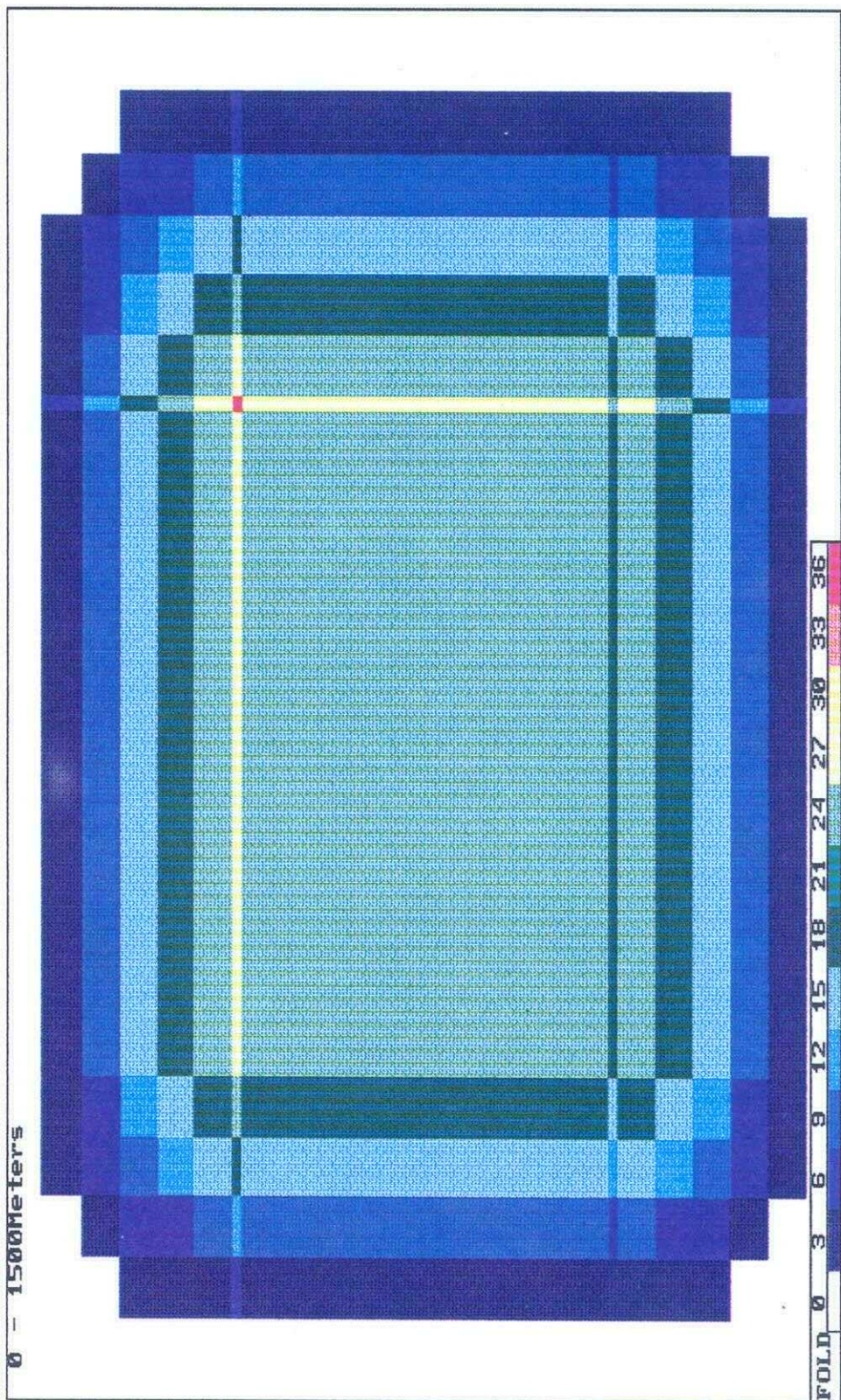
138

FIG. A.3 Fold distribution for the full-offset range for the conventional straight-line 3-D acquisition method.
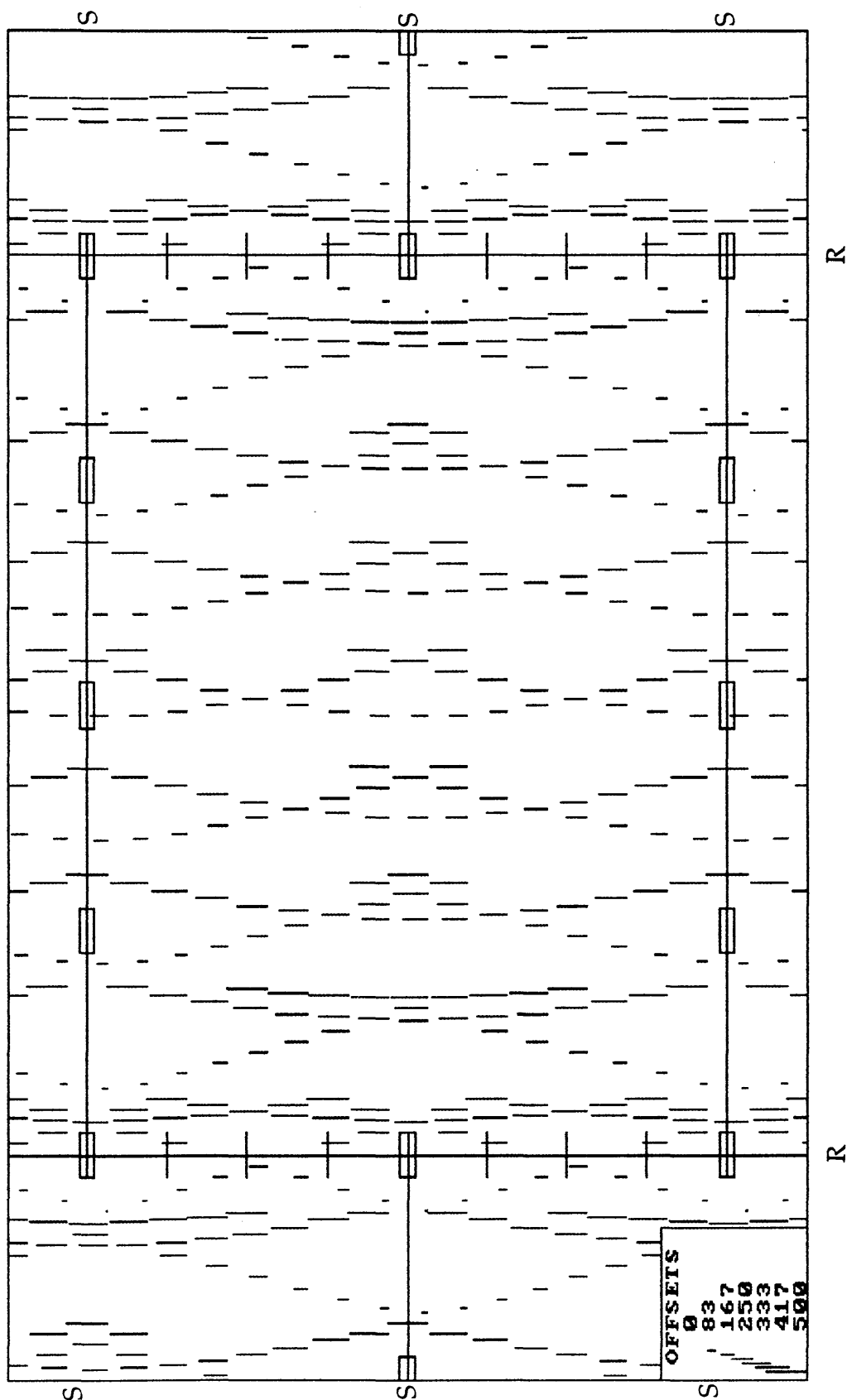
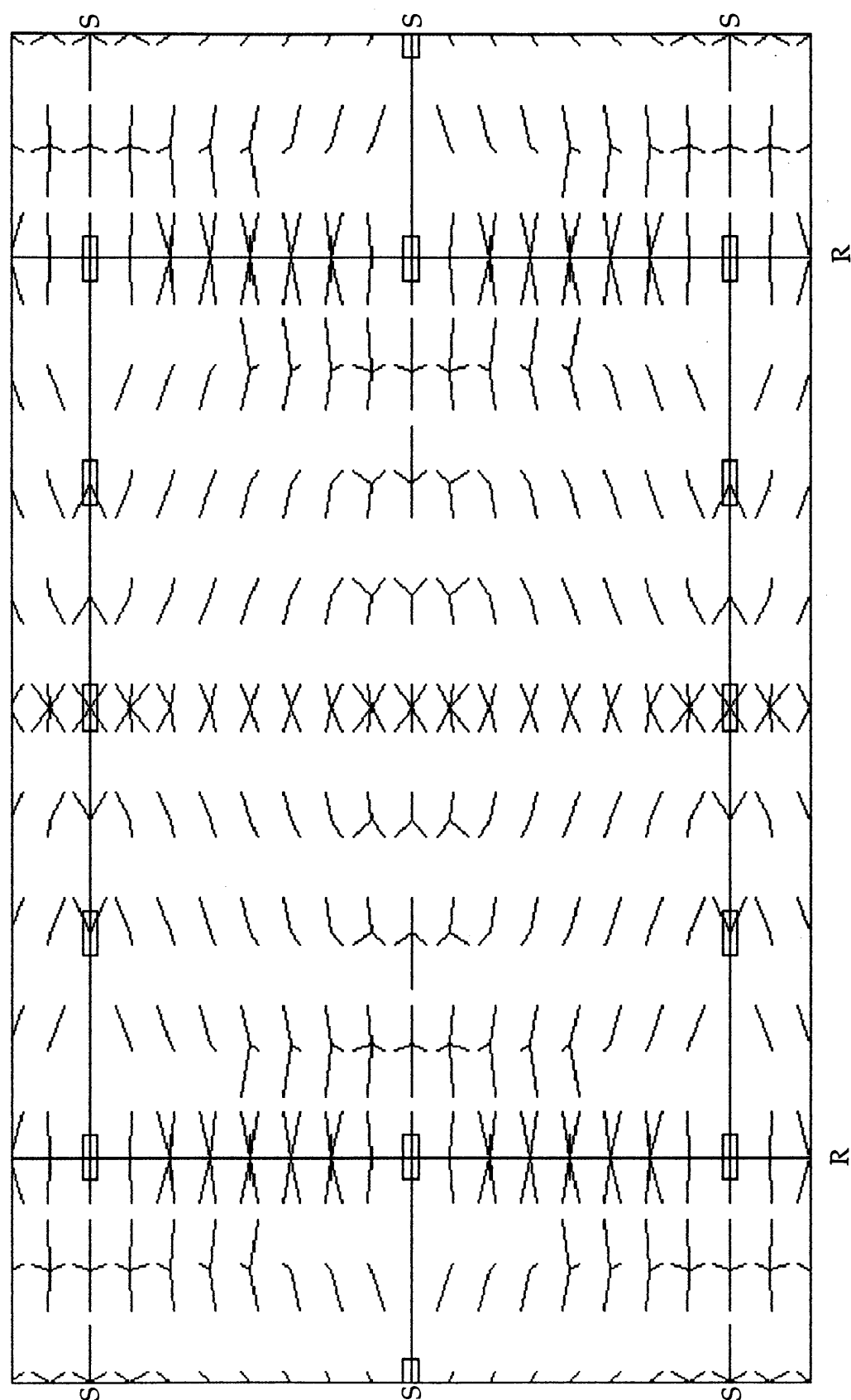FIG. A.4 Offset distribution for the near-offset range for the brick 3-D acquisition method.

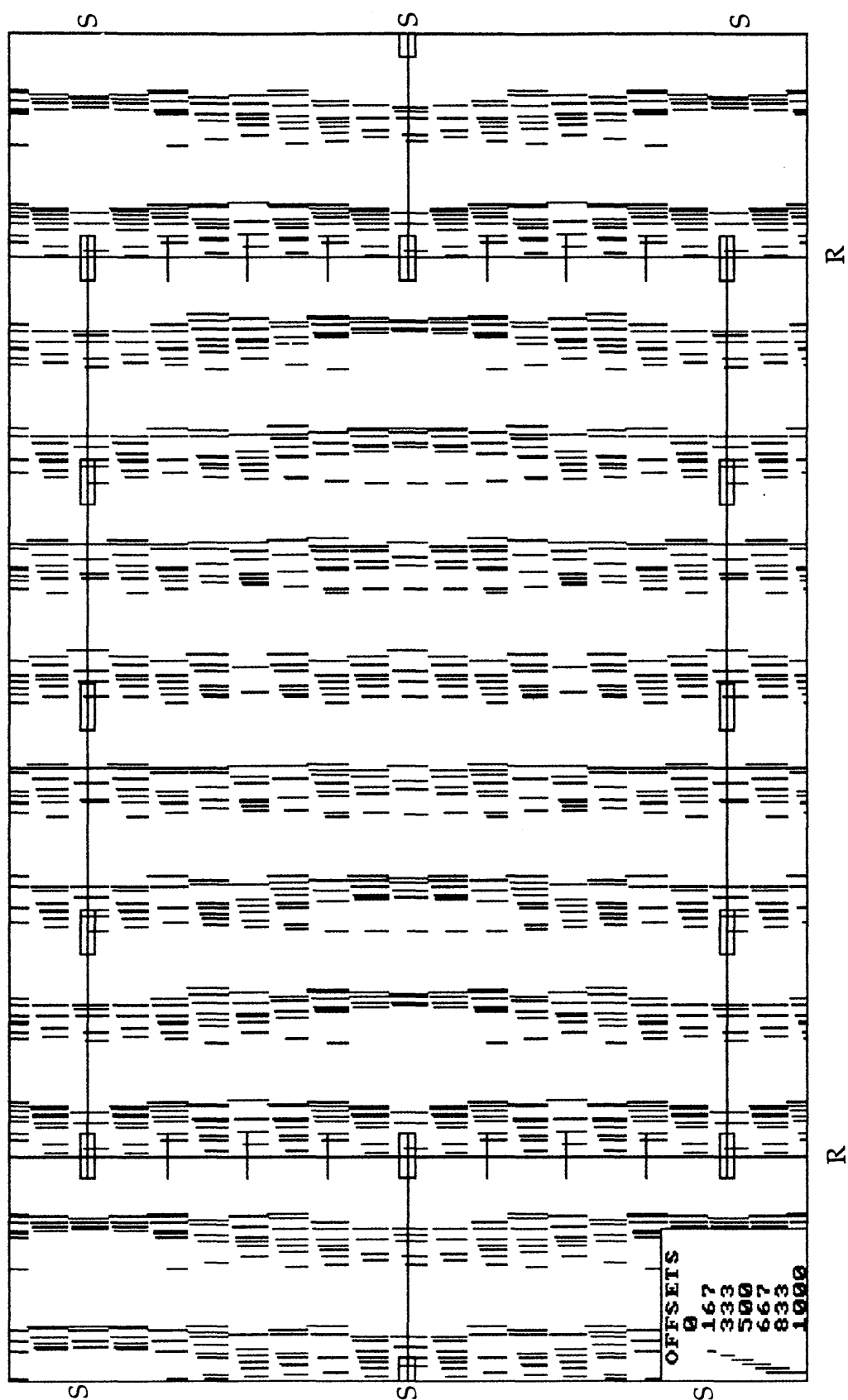FIG. A.5 Azimuth distribution for the near-offset range for the brick 3-D acquisition method.

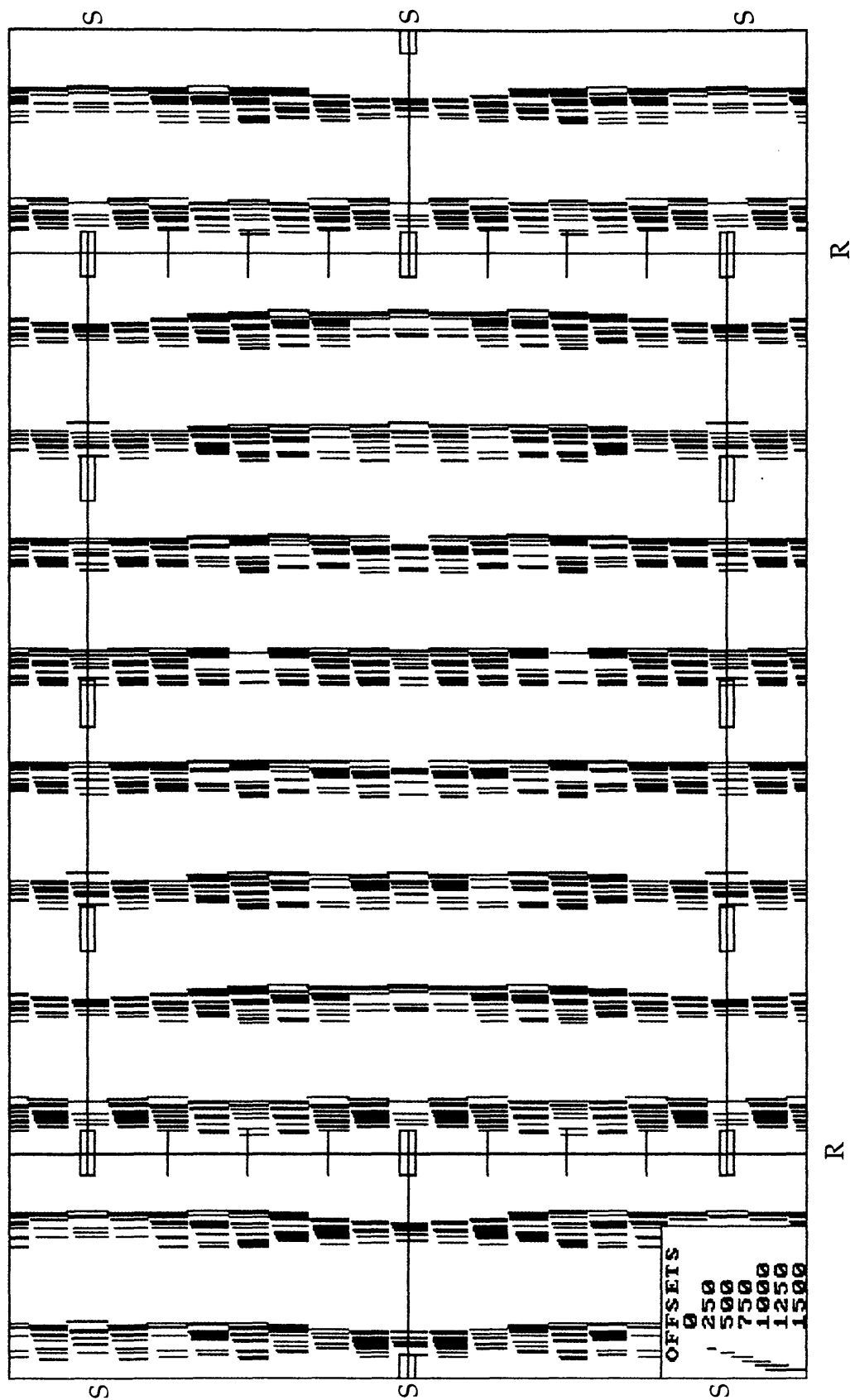FIG. A.6 Offset distribution for the mid-offset range for the brick 3-D acquisition method.

FIG. A.7 Offset distribution for the far-offset range for brick 3-D acquisition method.

bins where source and receiver lines intersect which contain only 3 offsets. In general offset distribution in the bins for the mid-offset range is more random then in the bins with the same offset range and a conventional straight-line method of acquisition. The offset distribution for the far-offset range has a poor offset distribution in bin in the center of the box (A Figure A.7). Offset distribution in the bins for this offset range is more uniform than the offset distribution for the same offset range but using a conventional straight-line method of acquisition (Figure A.7 verses Figure 5.12).

The azimuth distribution is uniform over the whole area for both the mid and far-offset ranges (Figures A.8 and A.9) but there is a denser azimuth sampling along lines parallel to the receiver lines which are at 1/2 receiver line spacing. Azimuth distribution over the mid-offset range (Figure A.8) is sparser then the same offset range using the conventional straight-line method of acquisition (Figure A.8 verses Figure 5.10). The azimuth distribution over the far-offset range is much more uniform than the conventional straight-line method over this offset range (Figure A.9 verses Figure 5.13).

The fold distribution for the near-offset range (Figure A.10) averages about 2-3 fold over entire survey which is lower than the 4-6 fold generated by the conventional straight-line method of acquisition for the same offset range. Fold distribution for the mid and far-offset range (Figure A.11 and A.12) is almost uniform through this offset range at 8-11 fold and there is no decrease in fold over the far-offset range like there is with the conventional straight-line method of acquisition. With the brick method fold distribution increases over the far-offset range compared to both the near and mid-offset range. In general fold distribution is lower than the conventional straight-line acquisition method up to
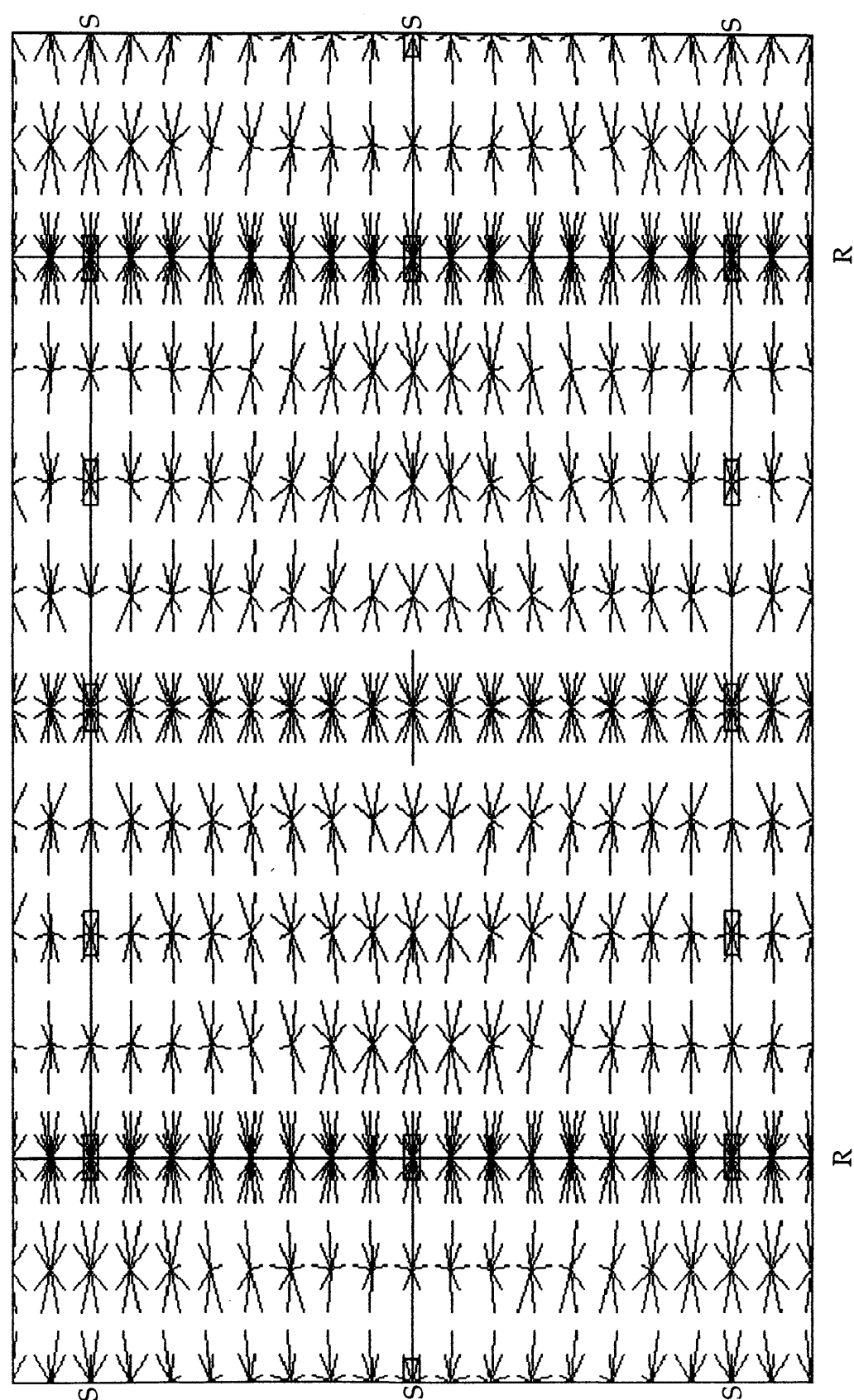
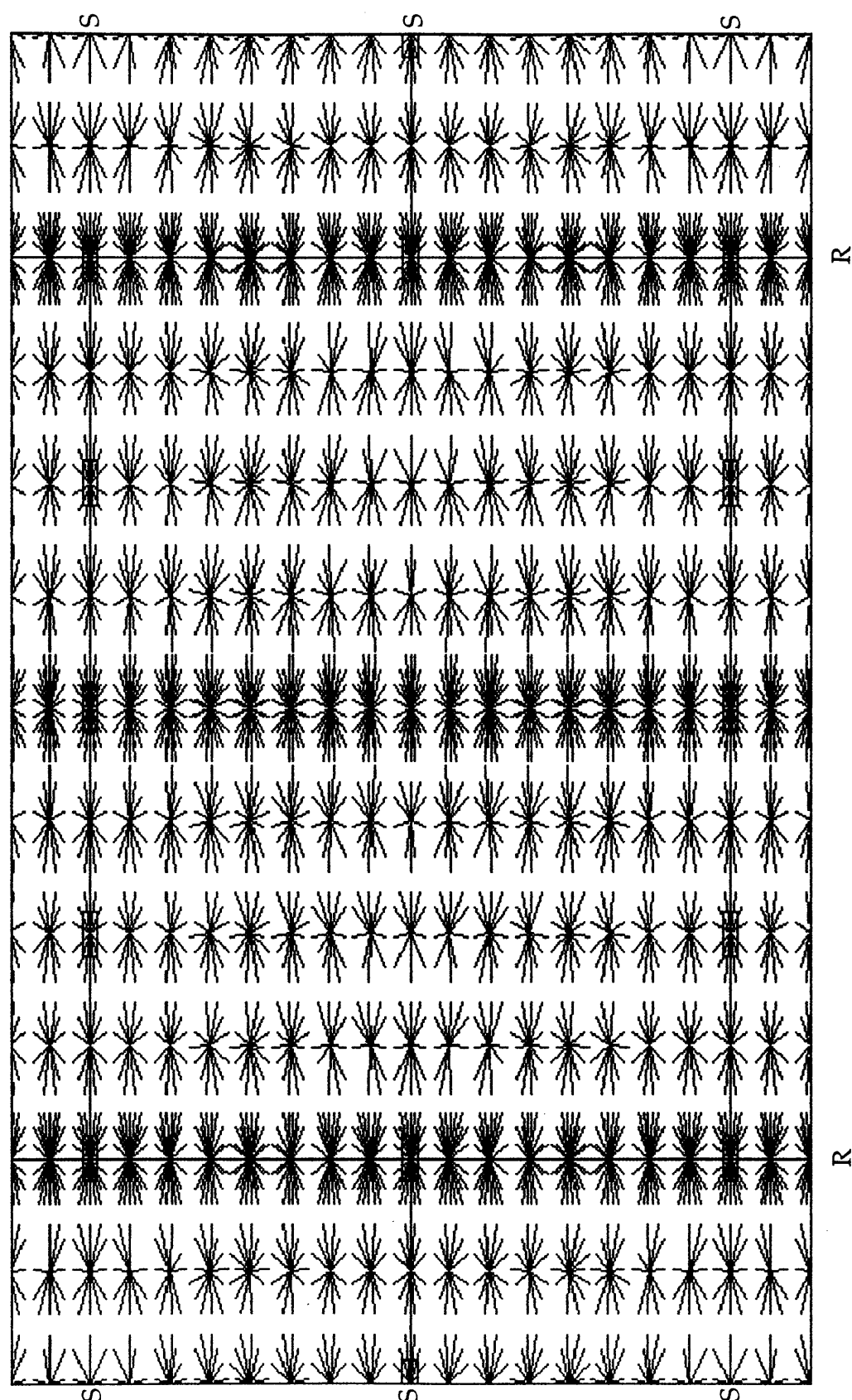FIG. A.8 Azimuth distribution for the mid-offset range for the brick 3-D acquisition method.

FIG. A.9 Azimuth distribution for the far-offset range for the brick 3-D acquisition method.
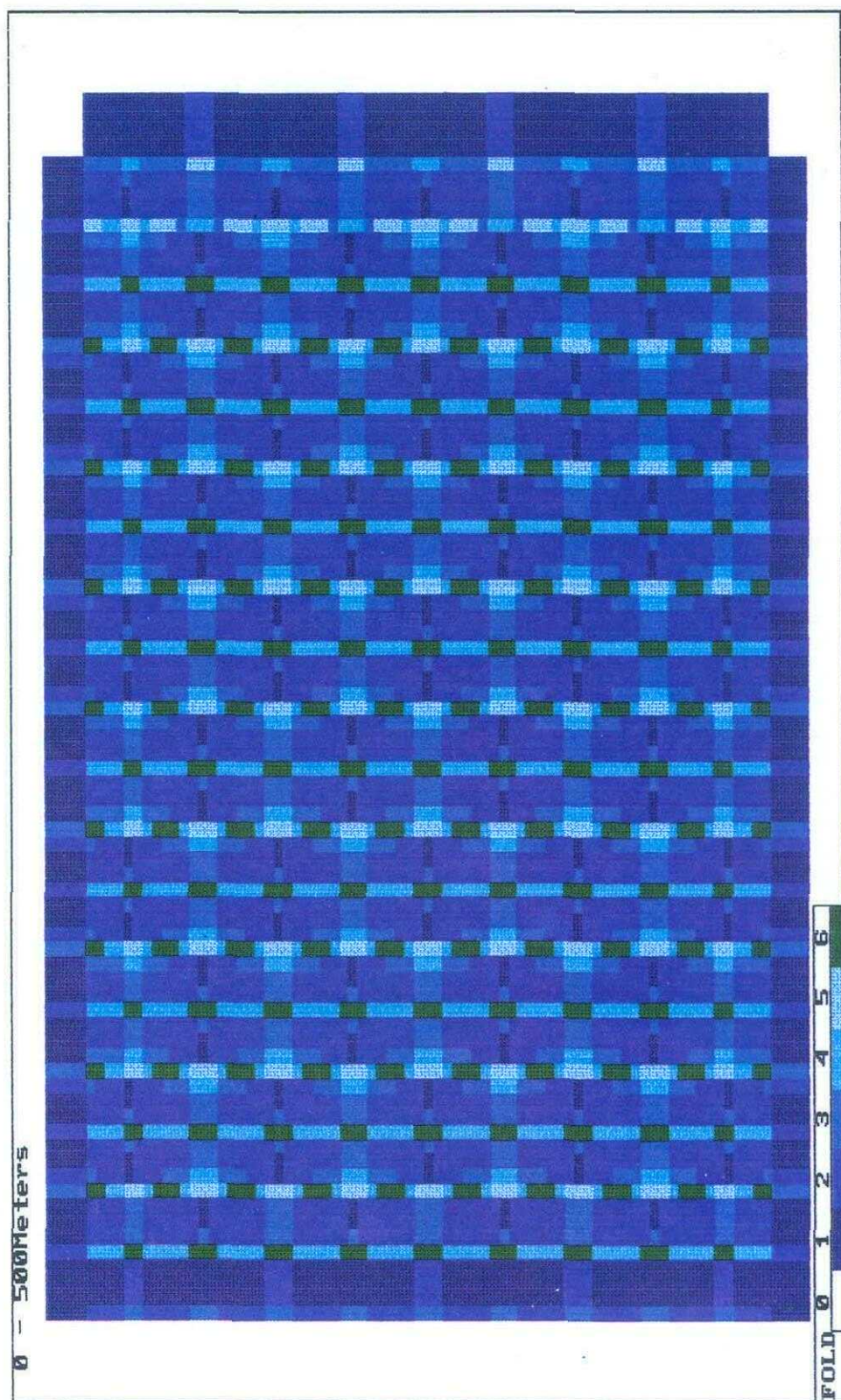
FIG. A.10 Fold distribution for the near-offset range for the brick 3-D acquisition method.
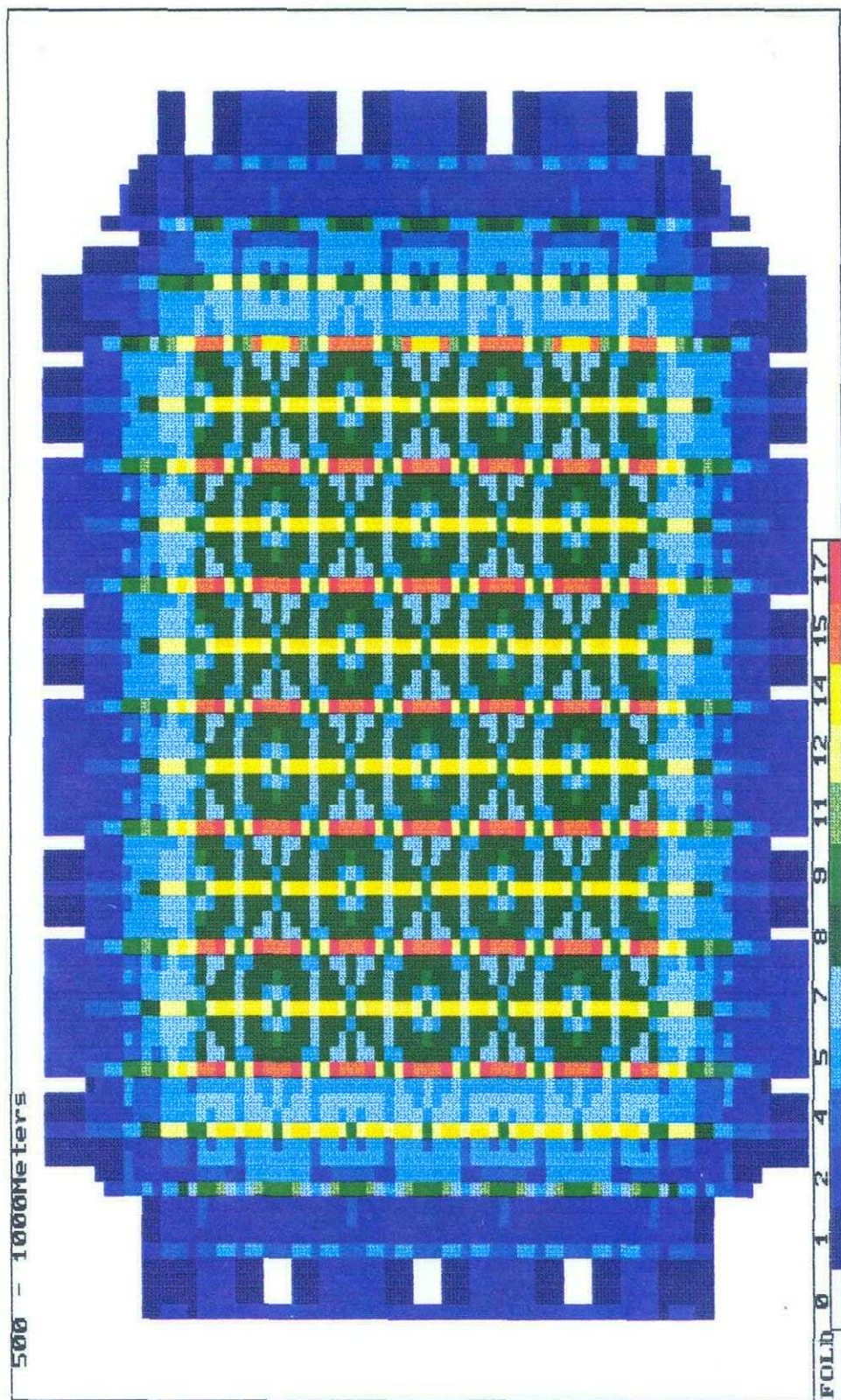
FIG. A.11 Fold distribution for the mid-offset range for the brick 3-D acquisition method.

1000 - 1500Meters

FOLD 0   2   4   7   9   11   14   16   18   21   23   25   28
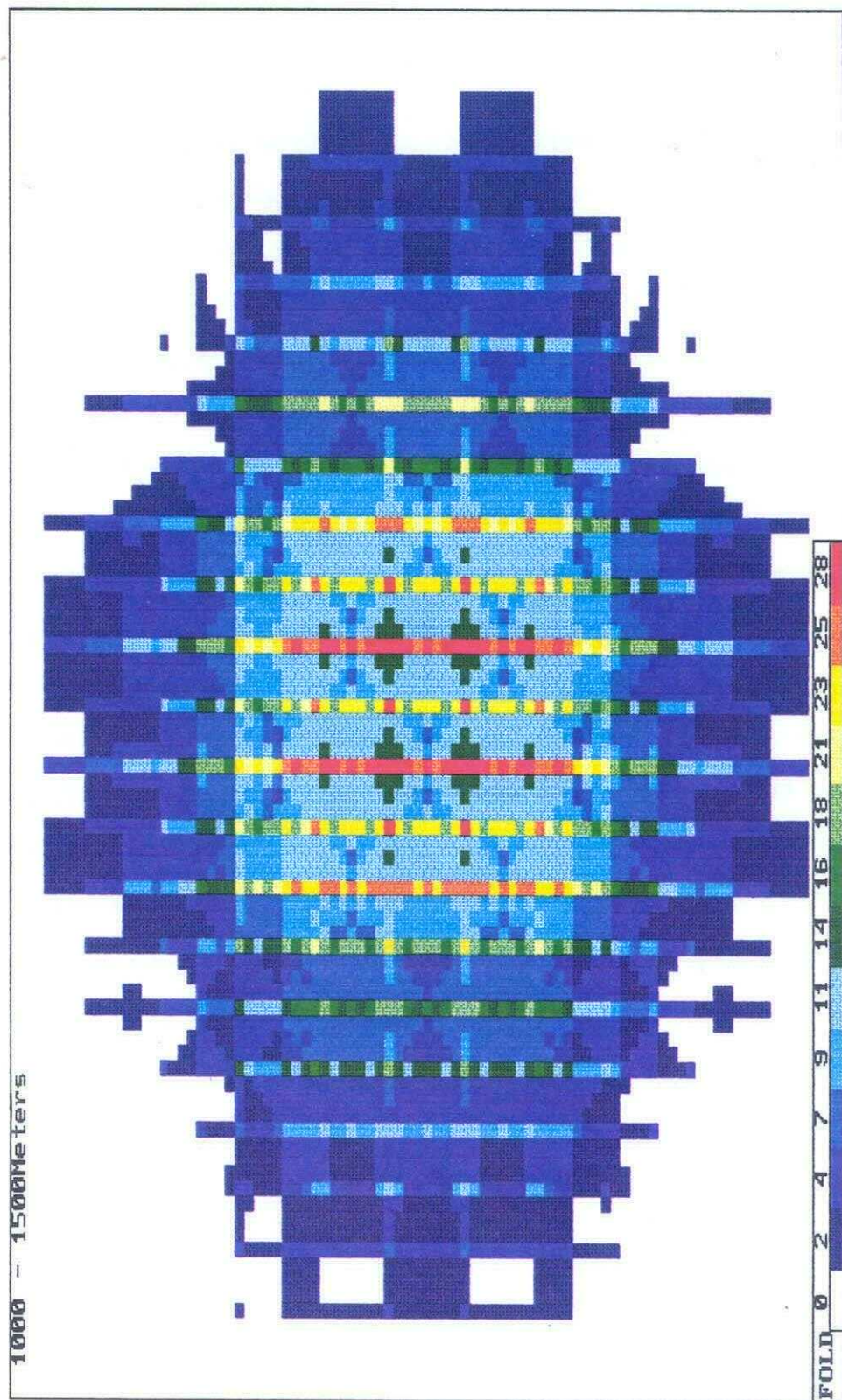
FIG. A.12 Fold distribution for the far-offset range for the brick 3-D acquisition method.

1000 m offset then it increases above conventional straight-line method of acquisition for the far-offset range.

In summary offset distribution for the brick method is more random than the conventional straight-line method up to the mid-offset range and then becomes more uniform over the far-offset range. The largest near offset is 200 m which is the same as the conventional straight-line 3-D acquisition method. The random offset distribution in brick method up to 1000 m offset will make it more difficult to determine stacking velocity and have coherent noise cancellation in the stack. Azimuth distribution follows the same pattern as offset distribution and is more sparse up to the mid-offset range than the conventional straight-line method and then becomes more uniform then the straight-line method at far offsets. This sparseness in azimuth distribution up to mid-offset range could create problems with static coupling between receivers and make azimuth dependent variations such as anisotropy more difficult to detect. Fold distribution is lower than the conventional straight-line method up to 1000 m offset then it increases above straight-line method of acquisition for far offset. This low fold distribution especially for near-offset range will affect signal to noise ratio and could make it difficult to determine proper velocity for NMO correction